Forschungsbericht 2024-19

Jet-Flap Interaction Noise of Highly Integrated UHBR Turbofans

Christian Jente

Deutsches Zentrum für Luft- und Raumfahrt
Institut für Aerodynamik und Strömungstechnik
Braunschweig

Deutsches Zentrum
DLR für Luft- und Raumfahrt

Forschungsbericht 2024-19

Jet-Flap Interaction Noise of Highly Integrated UHBR Turbofans

Christian Jente

Deutsches Zentrum für Luft- und Raumfahrt
Institut für Aerodynamik und
Strömungstechnik
Braunschweig

174 Seiten
73 Bilder
5 Tabellen
53 Literaturstellen

Deutsches Zentrum
DLR für Luft- und Raumfahrt

Herausgeber:

Deutsches Zentrum
für Luft- und Raumfahrt e. V.
Wissenschaftliche Information
Linder Höhe
D-51147 Köln

ISSN 1434-8454
ISRN DLR-FB-2024-19
Erscheinungsjahr 2024
DOI: 10.57676/1281-ze36

Erklärung des Herausgebers
Als Manuskript gedruckt.
Abdruck oder sonstige Verwendung nur nach Absprache mit dem DLR gestattet.

Aeroakustik, Triebwerksintegration, UHBR, Strahl-Klappen-Interaktion, Installationsgeräusch

Christian JENTE
DLR, Institut für Aerodynamik und Strömungstechnik, Braunschweig

Strahl-Klappen-Interaktionsgeräusch bei hochintegrierten UHBR-Strahlantrieben

Technische Universität Carolo-Wilhelmina Braunschweig

Diese Arbeit beschreibt einen herausfordernden akustischen Zusatzeffekt, der mit der Triebwerksintegration von großen modernen UHBR-Triebwerksdüsen an herkömmlichen Flugzeugplattformen einhergeht. Untersucht werden dabei Änderungen zwischen installiertem und isoliertem Strahlgeräusch, welche in der hierfür neukonzeptionierten Druckluftzufuhr für große Zweistromtriebwerke im Aeroakustischen Windkanal Braunschweig (AWB) experimentell ermittelt wurden. Als Flügelmodell wird das F16 Modell ohne Pylon verwendet.

Das industriell verwendete Messverfahren gilt für hohen Schub unter stationären Betriebsbedingungen oder niedrigen Flugbedingungen. Damit die Komplexität von mehreren Quellen im Übergangsbereich zu vornehmlichem Hochauftriebsgeräusch abgebildet wird, wurde das Messverfahren auf Flugbedingungen mit hohem Auftrieb und geringem Triebwerksschub erweitert.

Die Nahe/Ferne-Parametrik von Strahlscherschicht und Flügel wird analytisch hergeleitet und die Lücke in der bisher unzureichenden aero-geometrischen Charakterisierung des Problems geschlossen.

In den Experimenten werden nicht nur großzügig oder moderat ausgelegte Triebwerksintegrationen berücksichtigt, sondern der Messbereich auch auf besonders nahe („radikale“) Triebwerksintegrationen erweitert.

Ein Schlüssel für die Vorhersage des Strahl-Klappen-Interaktionsgeräuschs ist die Dreiteilung des Spektrums in tief-, mittel- und hochfrequente Anteile. Deren unterschiedliches Verhalten bei Änderung der Triebwerksintegration und Geschwindigkeit wird qualitativ herausgestellt.

Aerodynamische Untersuchungen bestätigen abhängig von Installationsnähe und Auftrieb vier qualitativ unterschiedliche Varianten der Strahl-Klappen-Interaktion, welche sich durch Strahlablenkung oder Strahldeformation geometrisch unterscheiden.

Die Arbeit legt damit die Grundlagen für die Modellbildung des Strahl-Klappen-Interaktionseffekts unter umfangreicher Berücksichtigung der Wirkgrenzen des Effekts.

Aeroacoustics, engine integration, UHBR, jet-flap interaction, installed jet

(Published in English)

Christian JENTE
German Aerospace Center (DLR), Institute of Aerodynamics and Flow Technology, Braunschweig

Jet-Flap Interaction Noise of Highly Integrated UHBR Turbofans

Technische Universität Carolo-Wilhelmina Braunschweig

This thesis describes a challenging acoustic penalty associated with the engine integration of large modern UHBR engine nozzles under the wing of conventional aircraft platforms. Changes between installed and isolated were experimentally determined with help of the newly designed pressurised air supply for large dual stream engines in the Aeroacoustic Wind Tunnel Braunschweig (AWB). The F16 model without pylon is used as the wing model.

The industrially used measurement method applies to high thrust under static operating conditions and low flight operations. In order to map the complexity of multiple sources in the transition area to predominantly high-lift noise, the measurement method was extended to flight conditions with high lift and low engine thrust.

The proximity parameter between jet shear layer and wing is derived analytically in order to close the scientific gap in the previously incomplete aero-geometric characterisation of the problem.

Not only generously or moderately designed engine integrations are experimentally tested, but the measurement range is also extended to very close ("radical") engine integrations.

A key to predicting the jet-flap interaction noise is the threefold division of the spectrum into low-, medium- and high-frequency components. Their different behaviour with changes in engine integration and velocity is qualitatively determined.

Depending on installation proximity and lift, aerodynamic investigations confirm four qualitatively different variants of jet-flap interaction, which differ geometrically due to jet deflection or jet deformation.

The work thus lays the foundations for parametric modelling of the jet-flap interaction effect with extensive consideration of the effect’s limits.

TU Braunschweig – Niedersächsisches
Forschungszentrum für Luftfahrt

Berichte aus der Luft- und Raumfahrttechnik

Forschungsbericht 2024-16

Jet-Flap Interaction Noise of Highly Integrated UHBR Turbofans

Christian Jente

Deutsches Zentrum für Luft- und Raumfahrt
Institut für Aerodynamik und Strömungstechnik (AS)
Braunschweig

Diese Veröffentlichung wird gleichzeitig in der Berichtsreihe „NFL - Forschungsberichte“ geführt.

Diese Arbeit erscheint gleichzeitig als von der Fakultät für Maschinenbau der Technischen Universität Carolo-Wilhelmina zu Braunschweig zur Erlangung des akademischen Grades eines Doktor-Ingenieurs genehmigte Dissertation.

Jet-Flap Interaction Noise of Highly Integrated UHBR Turbofans

Strahl-Klappen-Interaktionsgeräusch bei hochintegrierten UHBR-Strahlantrieben

Von der Fakultät für Maschinenbau
der Technischen Universität Carolo-Wilhelmina zu Braunschweig

zur Erlangung der Würde

eines Doktor-Ingenieurs (Dr.-Ing.)

genehmigte Dissertation

von:	Christian Jente
geboren in:	Luckau, Deutschland

eingereicht am:	25.01.2023
mündliche Prüfung am:	19.12.2023

Vorsitz:	Prof. Dr.-Ing. Jens Friedrichs
Gutachter:	Prof. Dr.-Ing. Jan W. Delfs
	Prof. Dr.-Ing. Sabine C. Langer

2024

Zusammenfassung

Das Strahl-Klappen-Interaktionsgeräusch wird dann wirksam, wenn ein Triebwerk sehr nah unterhalb des Flügels installiert ist. Die bei Start und Landung herausgefahrene Landeklappe kann dabei so viel Platz einnehmen, dass es zu einer Interaktion mit dem Triebwerksstrahl kommt.
Für die Charakterisierung des aeroakustischen Problems wird ein üblicher akademischer Ansatz verwendet, wobei der Effekt physikalisch beschrieben, in Bezug auf Geometrie und Betriebsbedingungen definiert und sowohl aerodynamisch als auch akustisch untersucht wird.
Eine besondere Leistung ist die Vereinfachung des Mehrströmungs-/Mehrkörperproblems, indem anstelle des Zweistromtriebwerks ein Modell für die initiale Mischregion des isolierten Triebwerksstrahls erarbeitet wird. So wird der Konflikt zwischen dem gegebenen Platzangebot durch den Flügel und dem Platzbedarf des Triebwerksstrahls aufgezeigt und die Vorhersage von einfachen Interaktionsszenarien ermöglicht. Um auch komplexere Szenarien darzustellen, wurden aerodynamische Untersuchungen durchgeführt. Diese beantworten Fragen zum lokalen Strömungsverhalten und inwiefern der Strahl abgelenkt oder deformiert wird.
Zur Durchführung der Messungen musste zunächst die Druckluftzufuhr des Aeroakustischen Windkanals Braunschweig (AWB) für den Betrieb von Zweistromdüsen neu konzipiert und umgerüstet werden (2014-2016).
Ein Mehrwert der AWB-Experimente wird durch das gezielte Austesten der Wirkungsgrenzen der Strahl-Klappen-Interaktion geschaffen: Hinsichtlich des Bauraums betrifft dies sowohl das Verschwinden des Effekts bei großzügig ausgelegten Triebwerksintegrationen als auch die Änderung der Strömungsphysik (Prallströmung) und Akustik bei radikalen Triebwerksintegrationen. In Bezug auf die Betriebsbedingungen geht es um Strahl-Klappen-Interaktion unter stationären Bedingungen und unter Flugbedingungen sowie um die Grenze des Effekts gegenüber Hochauftriebsgeräusch bei sehr geringem Triebwerksschub.
In einem hier zum ersten Mal definierten Strahl-Klappen-Interaktionsdiagramm wird abhängig von Bauraum und Strömungsbedingung der Betriebsbereich von Strahl-Klappen-Interaktion dargestellt und der Effekt in 4 Kategorien unterteilt.
Ein Schlüssel für die Vorhersage des Strahl-Klappen-Interaktionsgeräuschs ist die Einteilung in tief-, mittel- und hochfrequente Anteile. Deren unterschiedliches Verhalten bei Änderung der Triebwerksintegration und Geschwindigkeit wird qualitativ herausgestellt.
Um eine geeignete Datenbasis für die quantitative Vorhersage zu generieren, werden auf Grundlage der hergeleiteten geometrischen Analogie neue Messmethoden gezeigt. Diese Verfahren könnten die Grundlage bilden, um ein möglichst genaues Vorhersagemodell für das Strahl-Klappen-Interaktionsgeräusch abzuleiten.

Abstract

Jet-flap interaction (JFI) noise is a jet installation noise source which results from integrating an engine very tightly under the wing. Especially during take-off and landing, the wing must be operated in a high-lift setting. The resulting space conflict between the jet shear layer and the deployed flap causes an interaction which results in the very jet-flap interaction noise.

The conventional way to investigate an aeroacoustic problem consists of a problem definition, geometrical characterization, the investigation of acoustic effects and the corresponding aerodynamics. Since the problem is complex (4 bodies, 3 flow potentials), it needs a simplification to the most basic model that can be found.
A key contribution of this thesis is replacing a dual stream jet engine with a model of the isolated jet's so-called initial merging region, as well as defining the flap geometry in the same reference system. The model is suitable for explaining industrial relevant interaction scenarios where the flap is in close distance to the jet or interacts with the jet shear layer. It could be even extended for radical settings where the flap restricts the spatial distribution of the jet. Therefore, answers are needed to the questions whether interaction can be related to internal or external flow physics, whether the jet turns or is deformed at the flap and which mechanisms drive the change of flow.

The experiments were conducted at the Aeroacoustic wind tunnel Braunschweig (AWB) which needed a redesign of its pressurized air supply from single stream to dual stream. A great contribution to the academic community is testing the limits of the JFI effect in terms of build space and operations and finding suitable measurement methods. The build space is limited between generous engine integration where the effect is irrelevant and radical engine integration where flow physics (jet impingement) and acoustics change. The operations define the two investigated effects of JFI under static and flight operations, as well as the irrelevance of the effect when high-lift wing noise is significant.

This dissertation shows the qualitative differences of the JFI effect for each of the frequency ranges (low, mid, high) depending on build space and operational changes. These insights indicate the necessity for a rather detailed JFI prediction model.

Since the prediction requires a sufficient amount of conclusive data points, new measurement methods are derived based on the aero-geometric analogy. They could be the foundation to further the understanding of jet-flap interaction noise and help build a suitable prediction model.

Acknowledgement and some personal words

The results in this work were achieved during my ongoing work as research scientist at the Institute of Aerodynamics and Flow Technology at DLR Braunschweig (i.e. the German Aerospace Center). First of all, I would like to thank my supervisor Prof. Dr.-Ing. Jan Delfs for his valuable advice and encouragement throughout the study. My special thanks go to the reviewer Prof. Dr.-Ing. Sabine C. Langer and the chairman Prof. Dr.-Ing. Jens Friedrichs. My work profited tremendously from the general experience and the knowledge of Dipl.-Ing. Michael Pott-Pollenske, as a project lead, experienced designer, quick thinker, experimental scientist. Furthermore, many thanks to the DLR graduate program as well as my colleagues from technical acoustics.

I am thankful to live in a country which has decided to give itself an aerospace strategy and thereby fund its own aerospace research. The main contributions in this dissertation stem from the LuFo projects Power25 and LIST. Some benefits and insights refer to DLR internal campaigns, e.g. KonTeKst. The projects were partly funded by the German federal ministry for economic affairs and climate action and partnered by industry. As such, I would like to acknowledge the project partners from Airbus Operations GmbH, as well as Rolls-Royce Deutschland for their roles in the project and the clearance of data for publication.

I made a quick list of people who enabled me to write this dissertation on jet-flap interaction. It contains easily 100 names. The efforts with the General Data Protection Regulation allow me to only name a few by name, but I would like to thank everyone involved.

My history with jet-flap interaction research spans over a longer time period than my stay at DLR. In retro-perspective, I find it astonishing how I got the unique opportunity to gain my academical knowledge in such a professional and competitive environment. Back in 2012, Airbus Operations Bremen (Germany) gave me the chance to intern in the field of jet-flap interaction. Back then, I tried to find an analytical model for the mixed jet properties, but could only partly close this sub-problem. The closure had been published already, but I would not find the paper before I had completed the derivation myself.
I recognized the turning of the jet in the real expansion region, and - together with insights from current publications on coaxial jets - decided that the problem analogy for jet-flap interaction was too complicated to be simplified at that moment.
My research on high-lift devices led me more than once to DLR Braunschweig and my personal challenge to find an analogy to this problem was still on. This is the reason why I decided to apply at DLR in order to study the phenomenon from an acoustical point of view.

I got the opportunity to develop a cold jet test rig and felt highly motivated and prepared for this job, as I had previously designed multiple challenging internal flow systems (one at Virginia Tech and at two at TU Darmstadt).
One question which I found unanswered was how to deal with the cold core flow, as this is a violation of the scaling rule that requires the conservation of intensive flow properties.
Fortunately, I could solve this issue with the publications on local similarity as well as the discovery of dimensionally conserved total enthalpy flow rates. Thus, I would know for which nozzle the test rig was to be designed.
The initial design of the test rig was part of my Master's thesis. I would like to thank my supervisors from DLR and TU Darmstadt for their valuable feedback on the draft.
There are many inhouse and industry partners which should be mentioned for their good work or fine products. Take for example Ingo Dehne from Masterflex SE whom I would like to acknowledge for his efforts beyond normal work duty to increase the maximum pressure of their tubes with the help of a third-party steel reinforcement. This was a game-changer in the conceptual design as it helped to keep unwanted noise out of the plenum of DLR's Aeroacoustic Wind tunnel Braunschweig (AWB).
I would like to specially thank the many industry partners who shared technological in-depth knowledge, especially from MAN Diesel & Turbo SE (for a training session on screw compressors) and Samson AG (for helping me understand valve operations). This delivered the essential insights to program a digital version of the test rig and study its system behavior in advance.
Moreover, I would like to acknowledge and thank the precision machinists Jan Täger and Danica Knoblich who were eager in helping to convert the construction drafts into manufacturable designs and who ensured high quality test rig setups.

I would like to thank Heino Buchholz for the testing and installation of multiple measurement devices and systems and the programming and maintenance of the test rig software *koaxdruck*. Due to the expertise of Michael Pott-Pollenske, the wing model was conveniently prepared and optimized for jet-flap interaction studies.
Moreover, my thanks belong to the entire AWB test team as well as the partners from DNW-NWB for their compressor maintenance and control. In hindsight, I would say that the measurements went intuitively very well, even though this did not seem to be particularly obvious at this time. The post-processing of offline acoustic data was standardized by Daniela Almoneit whom I would like to thank for her good work.
The offline data results of the problem left me initially puzzled because they did not offer too many insights for a general theory. Hence, I was frustrated with the interpretation of the data and could not comprehend what made me choose a physical problem that consists not only of 4 bodies, but also 3 flows. I was able to retrieve some basic aerodynamic insights from CFD-simulations which a colleague provided.

In such times, it is good to get some encouragement and I would like to thank my flat mates, friends and family, especially my sister.
Furthermore, I am very thankful for Prof. Delfs' guidance and support during the dissertation. It was about this time, when I realized that I did not only have to solve one, but two different physical problems, namely JFI with static conditions (jet-plate interaction) and with flight conditions. There are quite some models around for the jet-plate problem, yet it seemed that no one could find a reliable model for the flight conditions.
The great turning point for this thesis came when I learned that two of my DLR-colleagues used a simple thin mixing layer model in other wind tunnel experiments. I figured that I could use this ansatz to model the initial merging region of an isolated jet shear layer.
I combined a derivation on jet noise with this ansatz and published a paper on jet-like shear layer noise. For the first time, I felt that I made a really great contribution to the field.
From this moment on, the way to the solution of the problem seemed to be much easier: The comparison of the required space of the isolated shear layer with the installation height of the flap trailing edge is the key to the 1D aero-geometric characterization of the JFI problem.
According to my knowledge, this thesis contains formerly unknown insights and I do firmly believe that the contributions are significant.

I would like to thank my writing buddies at TU Braunschweig library, my flatmates for keeping me energized and caffeinated, as well as my wife Janina and my brother Daniel Jente for their help with proof-reading.

Contents

List of Figures

List of Tables

Nomenclature

Symbols

Name	Unit	Meaning
α	[°]	(geometric) installation angle
α_o	[°]	outer shear layer spreading angle
χ	[°]	limiting angle defining redistribution area
δ_ω	[m]	shear layer width
δ_F	[°]	flap deflection angle
Δp	[bar]	difference pressure
$\dot{H}_0$	[W]	stagnation enthalpy flow rate
$\dot{m}$	[kg/s]	mass flow rate
μ	[-]	bypass ratio
$\mu_{A,I}$	[-]	area ratio of instrumentation ring
μ_A	[-]	bypass to core area ratio
ϕ	[°]	turning angle (engine axis vs and jet axis)
Ψ	[°]	azimuthal angle
ρ	[kg/m^3]	density
σ_0	[-]	shear layer spreading parameter
θ	[°]	polar angle
θ'	[°]	corrected polar angle
A	[m^2]	area
A_{noz}	[m^2]	nozzle outlet area
b	[m]	span width
c	[m]	chord length of an airfoil
C_P	[-]	pressure coefficient
c_p	[J/(kgK)]	specific heat capacity
c_r	[-]	shear layer convection ratio for radial position
c_U	[-]	shear layer convection ratio for velocity
D	[m]	engine diameter at nozzle outlet (w/o nozzle lip)
D_{mix}	[m]	mixed (or equivalent) jet diameter

Name	Unit	Meaning
f	[Hz]	frequency
f_m	[Hz]	mid frequency of third octave band
h	[m]	distance between acoustical source and shear layer
H	[m]	vertical distance between engine MRP and flap
He	[-]	Helmholtz number
i	[-]	counter / index variable
I	$[W/m^2]$	sound intensity
L	[m]	horizontal distance between engine MRP and flap
L_d	[m]	diffusor length
L_p	[m]	protrusion (bypass to core nozzle outlet)
M	[-]	Mach number
m, n, q	[-]	velocity scaling exponent
$OASPL$	[dB]	overall sound pressure level
$\tilde{p}$	[Pa]	RMS value of sound pressure
Q	$[m^3/h]$	Volumetric flow rate
R	[m]	distance of microphone to MRP
R_{mix}	[m]	mixing radius
r_U	[-]	velocity ratio
S_{geo}	[m]	coordinates of geometrical source
SPL	[dB]	sound pressure level
Sr	[-]	Strouhal number
T	[K]	Temperature
U	[m/s]	streamwise velocity
$\overline{U}$	[m/s]	mean velocity
$\hat{U}$	[m/s]	peak velocity
$U_\infty, Uinf$	[m/s]	ambient/flight velocity
U_{Byp}	[m/s]	bypass flow velocity
U_c	[m/s]	shear layer convection velocity
U_{Core}	[m/s]	core velocity (mean)
U_c	[m/s]	duct velocity
U_{jet}	[m/s]	jet velocity
U_{mix}	[m/s]	mixed jet velocity
V	[m/s]	Y-velocity
W	[m/s]	Z-velocity
X	[m]	streamwise wind tunnel coordinate
X', Z'	[m]	jet engine coordinates
x_0	[m]	virtual thin mixing layer origin
Y	[m]	wind tunnel coordinate
Z	[m]	wind tunnel coordinate

Acronyms and Abbreviations

1/3	third-octave
–	wind tunnel off
-0-	engine off
1D	one-dimensional
ac.	acoustic
AoA	angle of attack
APP	Approach, an engine operation condition according to ICAO annex 16
aux.	auxiliary
AWB	Aeroacoustic Wind Tunnel Braunschweig
BGN	background noise
BL	boundary layer
BOC	Bypass nozzle outlet center point, i.e. the engine MRP
BPR	bypass ratio
BYP	bypass duct
C	criterion
c	cross-sectional
CAD	Computer Aided Design
CB	Cutback, an engine operation condition according to ICAO annex 16
CFD	Computational Fluid Dynamics
ci	cross-sectional intersection
conv.	convenient
CORE	core duct
D	definition
DLR	Deutsches Zentrum für Luft- und Raumfahrt e.V.
dpt	data point(s)
e	energetic
e.g.	*exempli gratia*, for example
e1, e2	example 1, example 2
EMA	elemental motion analysis
ENG	engine, operational test parameter
ESP	engine slat pylon, an engine integration effect
F16	a three-element wing model
FI	flap insert
FN	flap noise
fs	full scale
FTE	flap trailing edge
g	gauge (pressure)
geo	geometrical
HL	high-lift

i	inner
i.e.	*id est*, that is
ICAO	International Civil Aviation Organization
id	idealized trapezoid
ISL	Inner Shear Layer, between bypass flow and core flow
iso	isolated
IVP	Inverted Velocity Profile (outer velocity faster than inner velocity)
JFI	Jet-flap interaction
JWI	Jet-wing interaction, an engine integration effect
l	lower
LE	leading edge
LIST	LIST engine model, geometrically scaled
M, Mic	microphone
meas	measured (i.e. uncorrected)
mix	mixed flow property
MN	mixing noise
mp	mean (of total) pressure between wind tunnel and bypass flow
MRP	Measurement Reference Point
ms	model scale
n/a	not applicable
NACA	National Advisory Committee for Aeronautics
nb	narrowband
NEN	nozzle exit noise
NVP	Normal Velocity Profile (inner velocity faster than outer velocity)
o	outer
OF	original flap
ONERA	Office national d'études et de recherches aérospatiales
os	original size
OSL	Outer Shear Layer, between ambient an bypass flow
p.	page
P25H	Power25 engine model, geometrically scaled
pot	potential
PPRIME	a French national centre for scientific research located in Poitiers
prim.	primary
PSD	Power spectral density
redist.	redistribution
Ref	Reference
rel.	relevant
S/L	shear layer
sec.	secondary
set.	setting
SFC	thrust-specific fuel consumption

SNR	signal to noise ratio
SR	(a spatially restricted) noise source region
SRN	slat related noise
SSJ	same speed jet, equal bypass and core velocity
st	static
t	total
TE	trailing edge
TN	turbulent noise
trans	transitional
TsAGI	the Russian Central Aerohydrodynamic Institute
u	upper
UHBR	Ultra High Bypass Ratio
Var1, Var2	an engine integration parameter where the height has been changed
VP	velocity profile
WLE	wing clean chord leading edge
WLE	main wing trailing edge
w.r.t.	with respect to
wt	wind tunnel
WTT	wind tunnel test

Glossary

- **low frequency JFI**: A frequency range smaller than $He_L < 1$. For the constant engine integration length L, this corresponds to the fixed frequency range of $315\,\text{Hz} \leq f_{1/3,ms} \leq 630\,\text{Hz}$.

- **mid frequency JFI**: A frequency range where in addition to the broadband JFI effect, several tones can be observed. It must start lower than $He_L = 1$ and could include $He_L \approx 4$, i.e. here $800\,\text{Hz} \leq f_{1/3,ms} \leq 3150\,\text{Hz}$.

- **high frequency JFI**: A frequency range which consists of a comparably small, but constant broadband-like JFI offset and does not contain tones. It is here defined for $He_L > 4$, i.e. $4\,\text{kHz} \leq f_{1/3,ms} \leq 40\,\text{kHz}$.

- **jet-like** shear layer: a shear layer where the jet is faster than the wind tunnel velocity. (opposite: wake-like shear layer).

- **jet-flap diagram**: This is an abbreviation for a diagram which describes the isolated jet shear layer space requirement (operational need) vs. build space at the flap (geometrical reality). The model covers 1D similarity geometries. It looks promising for not very closely coupled engine integration and low velocity ratios. The term has to be differentiated from the concept of an actual jet-flap interaction diagram.

- **jet-flap interaction diagram**: A diagram which genuinely describes jet-flap interaction effects with the help of the physically relevant similarity parameters. It copes with 2D/3D effects of jet redistribution and jet bending caused by close engine integration.

- **installed**: a test rig build information that typically refers to the engine being installed to the wing. This is the build for jet-flap interaction measurements.

- **isolated**: a test rig build information. Either the wing is not installed (isolated engine) or the engine model is not installed (isolated wind).

- **integrated**: a test rig build information. The engine is installed to the wing, but not operated.

- **static**: wind tunnel is switched off, i.e. the airplane is fixed/not flying

1. Introduction

Imagine you sit in an airplane, excited for your flight, you lean back and watch outside the window to check out the plane, and suddenly, the plane seems to be upside down. For some reason, the engine is located on top of the wing. This observation may lead to the question why it is very challenging to fit a new modern jet engine underneath the wing of an already existing airframe.

Airframe companies aim to enhance airplane operation by equipping an existing airframe platform with new engines (e.g. NEO or MAX concept). This is an economically interesting option, since the development of a new airframe is costly and associated with higher risk. New engine technologies, i.e. the Ultra high bypass ratio (UHBR) class, can improve the operational and acoustical performance of the standalone engine: Turbofans with increasing fan diameter and high bypass ratio improve the engine's thrust-specific fuel consumption (SFC), i.e. the efficiency of an engine design with respect to thrust output. Furthermore, the jet noise of the isolated engine decreases for the same thrust because the larger engine produces the same thrust at lower velocities. The lower velocities reduce the sound intensity and thus, cause an acoustic benefit.

However, the installation under the wing is limited by ground clearing restrictions and the specifications of an already existing airframe and landing gear system. Thus, the new engine may be installed in close proximity to the wing. The available space between engine axis and wing is even closer when the flaps are deployed in order to produce high lift. High lift is essential during take-off and landing and thus highly relevant for the population around the airport. The interaction between the jet and the flap causes the appearance of a new acoustical source in the mix of relevant noise sources which is called jet-flap interaction (JFI) noise. This acoustical effect can diminish the acoustical benefits which the new engines potentially offer. Therefore, jet-flap interaction noise must be understood on a qualitative physical level as well as quantitative level.

1.1. State of the art

Some of the first papers on jet-flap interaction date back to the 1980s (Way and Turner [52], Miller [35]). By experimental means a mismatch between the noise from an isolated engine and the noise from an installed engine was discovered. The found excess signal (for tight, but not radical engine integration) consists of a low/mid frequency peak and a more broadband-like offset for higher frequencies (e.g. Mengle [30], Huber et al. [20]). The low frequency peak was explained mainly due to the scattering of the near-field evanescent instability waves (Jordan [28]). The high frequency offset was suggested to stem from reflections of high frequency jet noise (SenGupta [42]), however this work will show that the high frequency noise of radical engine integration can exceed 3 dB and depends on thrust. Moreover, it was found that the jet-flap interaction noise scales with an exponent of 5 to 6 (SenGupta [42], Rego [37]). Jet-flap interaction noise does not only consist of broadband noise (amplifier mechanism), but also supports tonal components (oscillator mechanism). The origin of the tones seemed unclear for a longer time, yet, they were experimentally observed. From a theoretical point it is reasonable to assume a feedback loop between the jet shear layer origin and the flap trailing edge: An upstream travelling wave and a downstream travelling wave is required in order for resonance to occur. The downstream travelling wave consists of Kelvin-Helmholtz wave-packets. A variety of edge-tone problems can be explained using the coupling with an upstream travelling sound wave, but for jet-flap interaction this is not the case [28] [34] [43] [49]. Jordan showed "that the strongest tones are due to coupling between Kelvin–Helmholtz wave-packets and a family of trapped, upstream-travelling acoustic modes in the potential core." [28]. This family consists of TH-waves (Tam & Hu, [46]) as well as waves supported by the potential core of the jet (Towne [51] and Schmidt et al. [40]).

1.2. Scope and research objectives

This dissertation furthers the experimental side of the jet-flap interaction studies. The multi-flow, multi-body, multi-source problem consists of a vast parameter field.
While the ambition is to study the entire parametric field of this multi-dimensional problem, the shear quantity of parameters can be overwhelming. Hence, a model theory must be developed in order to narrow down JFI to its key characteristics. The model can be used to derive a test hypothesis a variety of operational and build parameters.
Finding a good model is not a simple task, as e.g. Segalini [41] showed on the study of coaxial jets: The number of parameters and dependencies is numerous and thus

difficult to systemize.
The testing of numerous build parameters requires a cost-effective wind tunnel facility. AWB is well-suited in terms of the rig and staff, especially the experience with high-lift wings. Contrary to the static installed jet-plate tests, even the smallest realistic model wings require fairly large UHBR engine models. Yet, the available air mass flow restricts jet operations to a Mach number range ($M < 0.6$) where the presence and study of tonal JFI is negligible. The focus of this study is rather to play the strengths of AWB by developing measurement techniques for JFI under flight operations, deriving testing and analysis methods based on the 1D similarity parameter model.

1.3. Outline

I. The road to building a JFI test facility Since the tests were conducted at the Aeroacoustic Wind tunnel Braunschweig (AWB) in Northern Germany, a pre-existing secondary air supply (single stream) needed to be redesigned to meet the needs of acoustic dual stream testing. The realization of this project is described in chapter 2.

II. The road to a physical model for JFI This dissertation starts off with the realization that the jet-flap interaction problem can be related to the jet-impingement problem with a declined jet (chapter 3). This is a problem which is mainly characterized by the streamwise jet properties. In comparison to the impingement problems, the "plate" (flap) is finite. Hence, the number of geometric parameters increases and radial jet characteristics become relevant (vertical parameters). However, as the crucial length between nozzle and flap can be limited to the initial region of the jet, there is an opportunity to formulate the spreading of the jet and its outer shear layer based on thin mixing layer theory. By separation of variables, the similarity based on 1D geometry can be formulated: Jet-flap interaction is characterized as a space conflict problem where the theoretical space requirements of a conically shaped isolated jet mixing layer has to adapt to the reality of geometric build constrictions. The geometrical parameters which define a truncated cone can be arranged in a ratio that resembles the arc tangent of the half cone tip angle. In other words, the problem can be defined in angles (first order) as long as the mixed jet radius is constant (second order). The half cone tip angle of the jet shear layer depends on the velocity ratio in the outer shear layer.
The model is simple enough and bridges to some extent the modeling gap between an inclined jet-impingement problem (infinite plate) to the interaction of a jet with a finite plate. The acoustical methods of measuring and evaluating this jet-plate

interaction (or:quasi-static jet-flap interaction) is explained and key facts on jet-flap interaction noise are generated from test data.

The next two chapters try to bridge the gap between jet-plate interaction and jet-flap interaction, chapter 4 from an acoustical perspective and chapter 5 from an aerodynamic perspective. There are two points in the derived model which must be addressed. The first one is the limit in operational conditions because only static or quasi-static jet-flap interaction can be investigated. When dealing with higher flight velocities, the high-lift wing noise components become relevant and jet noise is not the one and only aircraft relevant noise source. This changes the measurement and evaluation techniques for the general assessment of jet-flap interaction. Six data points and five builds are needed for the evaluation of a single jet-flap interaction noise delta. Engine and high-lift wing are measured isolated as well as installed and their background noise is qualified. An analysis of the isolated builds helps to identify operational ranges where the isolated noise component is negligible and the test method can be shortened.

This first critique point has also an aerodynamic component which is addressed in chapter 5. The model fails to address the effect which the wing's static pressure field has on the jet, especially underneath the wing and in the vicinity of the flap trailing edge. The thin mixing layer parameters of the isolated jet cannot be completely transferred to the flow underneath an airfoil. The hope is that the approximation is not too far off and that basic flow parameters can be used for a physical characterization of the noise sources. Critique point number two addresses very close engine integration from a qualitative point. The jet flow under the wing is analysed w.r.t. its internal and external flow properties and the question is discussed whether the flow turns or gets reshaped. The findings of the cross-sectional flow analysis are inserted into the jet-flap diagram in order to qualify regions of those aerodynamic effects. It is suggested to quantify close engine integration with a 2D geometry similarity, whereby interaction and redistribution areas are important. Such a quantitative analysis is not within the scope of this dissertation, but qualitative effects can be evaluated.

III. Studying the JFI problem from the perspective of aircraft relevant parameters There is a need to study jet-flap interaction effects caused by changing aircraft build parameters and operations (chapter 6). The model parameters (primary parameters) play a special role in comparison to other parameters. Based on the preservation of comparable geometries at the flap trailing edge position, two measurement methods are derived. The first one is called elemental motion analysis and is meant for the study of build parameters. The second one assumes the preservation of the outer shear layer width of the isolated jet (OSL width conservation) and helps to gain information on operational parameters.

2. Design and Commissioning of the AWB Pressurized Air Supply

The prerequirement to start with the scientific work on JFI was building a suitable dual stream pressurized air supply (see section 2.1) and qualifying its worthiness for good testing (see section 2.2).

2.1. Design of the AWB Secondary Air Supply

This was accomplished by extending an existing single stream air supply. Due to tight budget restrictions, the project was challenged with incremental improvement processes: The systems needed to remain operable at all times, changes needed to be relevant and cost-effective. Therefore, the first version was build with basic functionality and was enhanced step by step.

General The single stream test rig was designed for cold compressed air with flow rates of $1\,\mathrm{kg/s}$. The design goal for the dual stream flow supply was to max out the compressors' supply limits ($\geq 3\,\mathrm{kg/s}$). The pressurized air supplier DNW-NWB delivers humid and oily compressed air via a $350\,\mathrm{m}$ pipe (single source system).

Ambient air is sucked in using 2 screw compressors which consume max. $1.4\,\mathrm{MW}$ of electrical energy in order to deliver $3.1\,\mathrm{kg/s}$ at a gauge pressure of $6\,\mathrm{bar.g}$. The initial AWB secondary air supply system has been designed for mass flows below $1\,\mathrm{kg/s}$ by Schaeffer&Walcker, a local company specialized in pipe engineering.

The single stream system used the functions of filtering, flow separation, pressure reduction, silencing, and flow measurement. For the larger dual stream nozzles those systems needed adjustment. The design process until concept stage is documented in a master's thesis [21].

Technical air quality improvement Since old pipes are installed in the ground, a raw filtering device is needed. This helps prevent rust particles from damaging any valves or measurement devices.

The initially installed Boge particle filter device (for $\approx 1\,\mathrm{kg/s}$) was installed in the first JFI wind tunnel campaigns. It was replaced by a larger particle filter in 2019 since it caused very high pressure losses up to $\Delta p \approx 2.5\,\mathrm{bar}$ in off-design operation. The new pipe system also allows to install a secondary filter device: The use of a fine filter has been discussed as a future concept to improve technical air quality by reducing especially oil and some of the water condensate.

In order to prevent the formation of water condensate out of humid air, the installation of an adsorption filter with dew points around or below $-40\,^{\circ}\mathrm{C}$ has been discussed. However, an installation might be best on the side of the air supplier.

Safety concept There is a two-fold system in order to protect people and material from any harm:

1. A high pressure release valve protects the pipe and technical components from pressures greater than $10\,\mathrm{bar.g}$.

2. In case of an emergency stop, a bypass valve directs the air flow into a sandpit. The bypass valve is also very useful for adjusting the mass flow for the model.

Mass flow measurement The mass flow measurement system was installed in order to determine the engine's nozzle outlet properties by using a flow-based evaluation. It relies on conservation of mass and is dependent on completely sealed pipes. The mean outlet velocity is calculated by determining the geometrical nozzle outlet area and the subsonic outlet condition for the nozzle outlet pressure and density.

As the system evolved from single stream to dual stream, the flow measurement system in the main pipe is used to determine the total mass flow rate. The dual stream measurement (2016) was obtained due to an orifice flowmeter installed in the bypass flow pipe whereas the core flow was determined by subtracting bypass mass flow from total mass flow. Since 2019, the core mass flow rate can be measured with the help of a device which uses an energy conservation method (heat addition/cooling).

The option of using instrumentation rings introduces a different type of measure-

ment based on flow potential. The main task is the calculation of the nozzle exit velocity using the assumption of adiabatic and reversible (isentropic) flow conditions downstream of the instrumentation ring.

Flow separation. A Y-branch pipe mass flow divider separates the main flow into two pipes where the flows can be regulated, measured and silenced. At the end of the system, the dual flow system continues as coaxial tubes and coaxial pipes.

The 2016 budget restrictions made it inevitable to utilize a flow separation system using only one valve downstream the Y-separator. This made a thorough evaluation of the system analogous to an electrical current divider necessary. The extra calculation proved costly in terms of time, however, allowed to create one of the fastest, reliable and fail-safe dual stream controls. Since there is no second valve, the 2016 test rig can be adjusted for $BPR = 7 \ldots 30(\infty)$, which is a good range for UHBR short cowl nozzles.

The flow system beyond such a divider has to be carefully characterized in terms of hydraulic properties (i.e. area and loss coefficients). Small design changes have great impact on most of the other components (e.g. dependencies for pipe-in-pipe / tube-in-tube installations, dimensioning of orifice flowmeter, etc.) and require a redesign.

In order to evaluate design changes and system dynamics, a digital twin to the secondary air operations was developed by the author. (This method is for example also used for fuel management systems of cars.) The digital twin is fed by a database of ≈ 60.000 flow resistance values which change depending on flow conditions. The flow resistance values were determined using calculations from a flow solver that is based on 1D compressible flow equations [2][12].

In 2019, the mass flow divider was equipped with the second control valve. This extends the BPR-range for testing nozzles with varying area ratios, e.g. long cowl nozzles.

Wind tunnel pipe and interface The design of the tubing and piping behind the silencers is very sensitive. Especially in the wind tunnel nozzle, all inner and outer surfaces are flow surfaces and thus, conventional steel pipes with flange joints are not possible anymore.

The solution which was used is to build light parts with thin walls and smooth and sealed surfaces. This is accomplished by using standard aluminum pipes which are

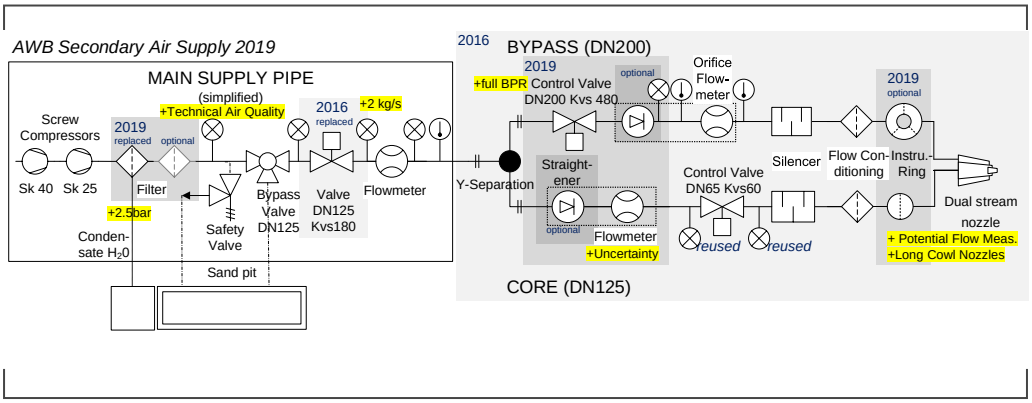

Figure 2.1.: **AWB secondary air supply system**

welded or glued to aerodynamically shaped flat flanges. The flanges can be screwed together and therefore allow to integrate other functional devices, i.e. a settling chamber or an instrumentation ring.

The **settling chamber** design is very challenging, because the local area is restricted in space. The challenge of higher flow velocities was solved by using a 4 stage cascade of high-performing subcritical screens. During the 2019 redesign, the cascade was extended to a 6 stage cascade.

An **instrumentation ring** is the industry-typical interface between wind tunnel and test owner. The interface geometries are provided to the test owner who builds an adapter to the engine model which is to be tested. In 2019, the decision was made to avoid any boundary layer suction technology by planning two different instrumentation rings for small nozzles $D_{mix} \leq 90\,\mathrm{mm}$ and larger nozzles $D_{mix} \leq 140\,\mathrm{mm}$. The smaller instrumentation ring was built and successfully tested in 2019. The following concept studies were carried out in order to enhance the performance and testing:

- Helium supplied core flow: A concept study to simulate hot core flow properties with a cold air-helium mixture. Involved partners: Linde Gas, Wittgas GmbH.

- Heated core (using heat injection techniques and heat removal analysis from wind tunnel). Industry partners: Siekerkotte.

- Suction operation for engine inlet studies. Industry partners: Samson AG, SKI GmbH.

- Flow rate extension using compressed air receivers for storage/buffer or secondary sources. Involved industry partners: Kaeser.

2.2. Qualification of jet noise acoustics

Low test rig noise design for core duct and bypass duct Real engines contain internal struts or guide vanes. This may add spurious noise to the jet noise acoustics and cause a mix of noise sources. The experimental piping also requires struts for fixation of two pipes to create a the dual stream. However, the duct system's spurious self noise must be negligibly small compared to the acoustics of a jet issuing from a particular nozzle.

The piping system was designed with an industrial design criterion $M_{duct} < 0.35$ where unwanted noise from internal guide vanes in a channel is deemed negligibly small compared to the wanted jet noise signal. A better interpretation of this criterion is to calculate the area ratio between the duct at $M_{duct} = 0.35$ and a choked ($M_{jet} = 1$) jet at the nozzle outlet (equation 2.1) using the isentropic flow equations.

$$\frac{A_{duct}}{A^*} \left(M_{duct} = 0.35\right) \approx 1.8 \tag{2.1}$$

The reformulated design criterion indicates that any internal struts or guide vanes should be placed upstream of the nozzle outlet where the duct area is at least 1.8 times larger than the nozzle outlet area. The 2016 wind tunnel pipe does not fully suit this better interpretation of the design criterion[1]. Therefore, the duct and jet noise of the engine models LIST and P25H is studied in the next paragraph.

Test methods for test rig noise There are several concepts available to study duct noise. They can be categorized by measurement type and evaluation method. The evaluation differs depending on spectrum (narrowband or third-octave), the measurement type depends on changing nozzle outlet areas or velocities (for duct or jet). Let us look into the narrowband velocity scaling method, because it is very good for the evaluation of spectra which are not very smooth or even include tones.

Gaeta and Ahuja [17] published the process of scaling narrowband data for static jet noise. The essence of the difference between narrowband and third-octave scaling is shown in equation 2.2. Gaeta and Ahuja can scale any bandwidth, as long as the spectra are converted into Power Spectral Density (PSD) first.

For reason of a simple demonstration, the following assumptions are made: same nozzle (D_{jet}=const.), same flow medium and ambient conditions (ρ_∞, a_∞ = const.),

[1] The redesign in 2018/2019 provided a more suitable duct with less guide vanes.

far-field microphone at nozzle outlet plane, perpendicular to jet axis ($\theta = 90\,^\circ$), jet velocities U_{jet} vary.

$$SPL_{normed} = SPL_{...} - 10\,\lg(\Delta f) - 10\,\lg\left(\frac{D_{jet}}{U_{jet}}\right) - 80\,\lg\left(U_{jet}\right) \tag{2.2}$$

The bandwidth Δf is defined in equation 2.3:

$$\Delta f = \begin{cases} \text{const.} & , \text{ narrowband} \\ \underbrace{\frac{2^{1/3}-1}{\sqrt{2^{1/3}}}}_{0.2316} \cdot f_m & , \text{ third-octave band} \end{cases} \tag{2.3}$$

Gaeta and Ahuja's data shows that the conventionally scaled third-octave jet noise spectra peak approximately at unity Strouhal number ($Sr = f\,D_{jet}/U_{jet} \approx 1$) whereas the narrowband (and PSD converted) spectra peak at $Sr \approx 0.3$.
The author has contributed to the theory [24] by deriving the acoustic intensity of mixing noise from jet-like shear layer flows (see figure 3.4) caused by engines operating in flight condition (i.e. with an ambient co-flow). The derivation underlines that jet noise scales with U_{jet}^8 for constant velocity ratios $r_{U,OSL}$, i.e. the ratio of wind tunnel velocity U_∞ to jet velocity U_{jet}.
Two special cases which come up within the derivation process and they characterize jet sound intensity: Static and quasi-static jets do asymptotically fit with the exponent set $[m = 6, n = 2]$ of opposite velocity profiles whereas unity velocity flow profiles align with the exponent set $[m = 4, n = 4]$. Hence, a wide velocity range of jet shear layer like flows scales well with the exponent set $[m = 5, n = 3]$.

$$I_{1/3} \propto U_{jet}^q \cdot (1 - r_{U,OSL})^m \cdot (1 + r_{U,OSL})^n \cdot A_{jet} \tag{2.4}$$

$$q = m + n = 8 = \begin{cases} m = 6, n = 2 & , \text{ opposite velocities } U_{jet} = -U_\infty \\ m = 4, n = 4 & , \text{ unity velocity profile } U_{jet} = U_\infty \end{cases} \tag{2.5}$$

Scaling exponents of $q = 8$ and $m = 5\ldots6$ for subsonic flight operations were independently confirmed by Michalke/Michel [32] and Sandberg/Tester [39].
The nature of AWB as a closed-circuit wind tunnel does not allow for academically pure static jet noise testing (zero co-flow). Thus, a fixed non-zero velocity ratio has been chosen (see figure 2.2). For the same nozzle operating at similar velocity profiles $r_{U,OSL} = 0.21$, and microphones perpendicular to the nozzle outlet $\theta_{mic} = 90\,^\circ$ a notable scaling difference of $\Delta SPL \approx 5\,\text{dB}$ was measured across five different operating conditions. The narrowband gain fluctuates with $3\ldots5\,\text{dB}$ around its spectral average. This is unwanted because it complicates the evaluation. Yet, this quality of spectra is the reality for many experiments across well-known facilities. A workaround to smooth the signal is to increase the bandwidth (here: $\Delta f = 12\,\text{Hz}$) or use filters to smooth. Another way to achieve sharp spectra is to scale the third-octave data. This is also shown in figure 2.2.

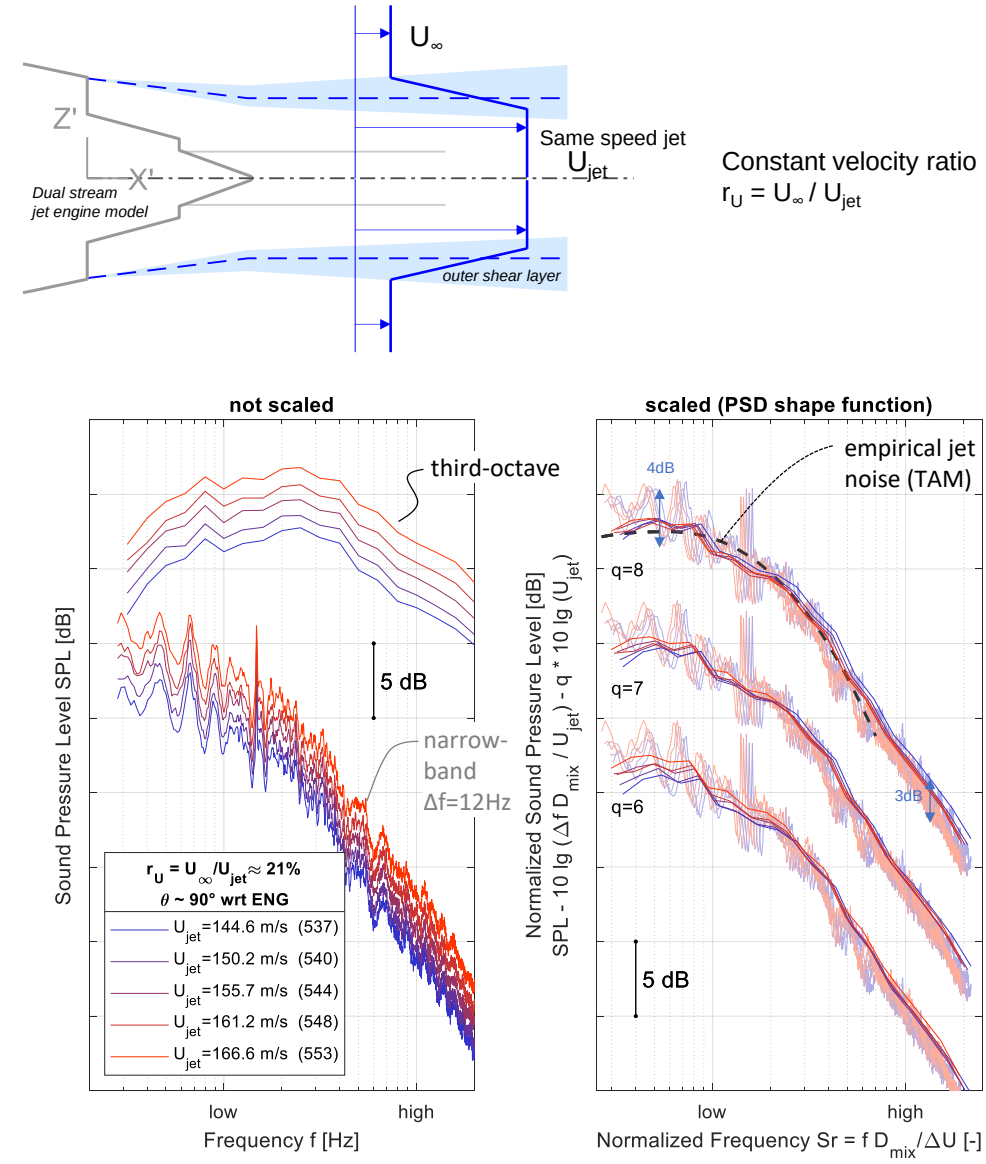

Figure 2.2.: **Velocity scaling of jet noise at flight operations**

The spectra collapse with an exponent of $q \approx 7 \ldots 8$. This means that the jet noise share of the nozzle's total noise is significant. It is debatable whether duct noise is still a contributor to the measured data. Differences in the scaling exponent may be also the result of jet noise directivity (e.g. microphone distance compared to the spatial jet noise source region): Zaman & Dahl [53] found a scaling coefficient of $q = 6.5$ at $\theta = 90\,^\circ$ as well as $q = 8.5$ at $\theta = 25\,^\circ$ when scaling coannular nozzles.

Another method of rig noise evaluation using different nozzles for the same duct noise is displayed in figure 2.3. In this setting, an open duct with a large nozzle outlet area should produce minimum jet noise whereas small engine models cause significantly higher jet noise. The qualitative results of the analysis are a clear indication for the presence of the jet noise sources as well as not very smooth spectra which are related to the exited frequencies measured in the open duct setting.

Final statement on duct noise The methods indicate that the ducts provide some good signal to noise ratio for the models, but also that the test conditions are not clinical w.r.t. acoustic jet noise testing. This means that test rig noise of some sort is still relevant. Yet, it does not dominate total (jet + test rig) noise. Furthermore, the smoothness of the spectra is not neat for quantitative analysis of third-octave with low uncertainty requirements.

Nevertheless, the test system can be used for qualitative analyses of jet-flap interaction. This is supported by results of DLR-project KonTeKst where a counter-rotating ultra high bypass ratio fan (CRUF) was installed to a wing. Even though the turbo noise with its tonal (blade passing) components buried especially the mid frequency part of the spectrum, the effect of jet-flap interaction could still be measured (especially for low frequencies). As an essence of that measurement, one could postulate that no matter how little or how much the jet flow is disturbed upstream the flap, the flow has to address the flap hindrance which blocks its natural space for transitioning into the free field condition. This causes some additional JFI decibels.

In other words, it is great to build an improved test system with presumably less test rig noise. This will help to make quantitative values even more reproducible when compared to other testing environments. However, a real jet engine does also deal with the imperfection of guide vanes or even a pylon disturbing the pure jet noise source. The presence of slight imperfections at the engine noise source should not prevent the occurrence of qualitative jet-flap interaction effects. Therefore, the system is suitable for qualitative evaluation and for comparing builds when referring to the same nozzle.

Various nozzle outlets at same duct operations
duct velocity U_d=const

Idea: Same duct velocity U_d produces same duct noise.

Smaller nozzle exit area ($A_d/A_{jet} > 1$) causes $U_{jet}>U_d$ (conservation of mass).

- If duct noise is significant, all spectra are the same.
- If jet noise is significant, smaller nozzle exit areas should produce the highest noise

Shortcomings for quantitative analysis of this example:
- LIST-like / P25H bypass engine model ducts contain one more set of guide vanes than the OPEN duct . This causes additional internal noise (not only jet noise).
- OPEN bypass duct has not been assessed for possible separations

Qualitative results:
- P25H and LIST-like signal is not equal even though they share the same internal noise: This means that jet noise is produced
- Jet noise spectrum is not smooth, it contains tonal components which are exited at the OPEN duct. This smoothness is therefore related to internal / duct noise.

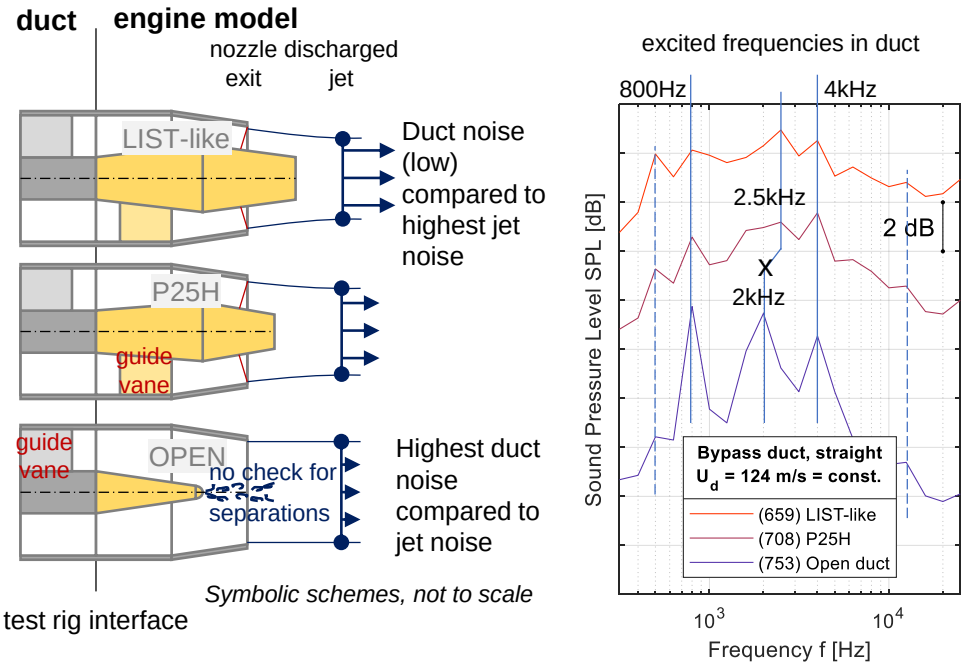

Figure 2.3.: **Jet noise vs. duct noise evaluated from duct perspective**

3. A simple model of academic jet-flap interaction

"A physical model to a problem must be as simple as possible, but not simpler. It must be complex enough, to model essential effects without being reduced to triviality." This is the author's own wording of a rather famous quote of undocumented origin, yet often referred to Einstein. It is the essence of every scientist to find an explanation (in other words: a model) to a complex phenomenon.

Hence, this chapter is meant to identify characteristic parameters in order to model jet-flap interaction. The hypothesis formulated in this chapter focuses on static jet-flap interaction (or: jet-plate interaction). In addition to the horizontal parameters which characterize jet impingement (i.e. a related problem, see figure 3.1), the vertical space needed by an isolated jet shear layer as well as the flap boundary layer. The model for static jet-flap interaction is already complex enough. Yet, it serves merely as a starting point in order to explore jet-flap interaction in the following chapters.

In the theory sections, the engine and its jet are studied and shear layer properties are derived. Moreover, the boundary layer of the flap is approximated and has been found to be negligibly small. The available geometrical space between flap trailing edge and engine axis is set by a reference setting and otherwise not further

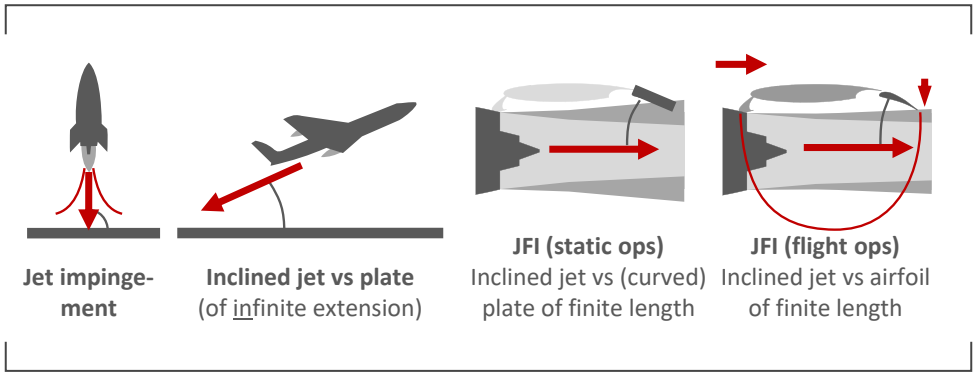

Figure 3.1.: **Physically related problems**

questioned in this chapter. But, the adjustment of build parameters which determine the free build height is thoroughly studied in chapter 6. The evaluation chain to static jet-flap interaction is explained as well as measurement data of cases fitting the model and model flaws are portrayed.

3.1. Model hypothesis for (quasi-)static jet-flap interaction

One of the first questions which needs an answer is whether it is technically possible as well as sufficient to reduce the complexity of the four-body problem to a one-body problem with a mere interaction between the "jet" (*better:* a shear layer like flow) [1] and a semi-infinite wall which ends at the position of the flap trailing edge. The flap could be also approximated by a finite flat plate which is installed at an inclination angle to the flow.

From a geometrical point of view, it must be evaluated how much vertical space the flow's shear layer thickness as well as the flap boundary layer thickness [2] need as well as how much vertical space between the engine axis and flap trailing edge H is available.
There are three cases which would influence the spectra: 1. no interaction and thus possibly no jet-flap interaction noise, 2. the flap blocking the space needed for parts of the (isolated jet engine's) outer shear layer, as well as 3. the jet blocking the space for the outer shear layer as well as parts of the bypass jet potential core. Listing more cases might be appealing on first sight. These cases concern interaction with the inner shear layer or core flow potential core. However, such an interaction is not very likely: It is possible to compress a mixing layer like the outer shear layer. The shear layer can be seen as a result of a local force or momentum balance between bypass and flight stream. The presence of the flap can easily shift the balances. In contrast to the outer shear layer, the bypass potential flow is the main contributor for jet thrust. This flow can be manipulated by some extent, but this is much harder to do.

[1] The jet is a "flow which is generated by a fluid that exits through a nozzle into a quiescent environment."[41] In between the jet (high velocity) and the quiescent environment (no velocity), a shear layer formulates which bridges the two different velocities. The shear layer grows in streamwise direction and is a vital part in the jet-flap interaction.

[2] The boundary layer is "the region of fluid around a moving wall which is influenced by the presence of the wall. In this region viscosity and turbulence effects play an important role altering significantly the local flow. Theoretically, all the fluid is affected by the presence of the wall, but only the boundary layer is subject to significant modifications." [41]

However, it is rather difficult to find aerodynamically sound installations where the flap could directly interact with the core potential core as this would require to locally diminish the protection of the bypass potential core. This unlikely case could be possibly forced by unconventional dual stream engine designs, radical pylons, flow deflectors or very steep flap settings which cause the core flow to fully impinge on the flap.

Should those core-relevant parts of the jet interact with the flap (i.e. without the "protection" of the bypass stream), then this might cause a problem with the local similarity between the cold test and the hot real engine. However, those very special cases are not within the scope of this thesis.

In the following sections, the model parameters are determined: The mixed jet diameter (section 3.2 and appendix A) and the thin mixing layer model are derived. This helps to determine the space requirements for an undisturbed isolated outer shear layer for the jet (section 3.5).

3.2. The engine model and it's mixed jet diameter

This section is about the jet engine model and the derivation of the mixed jet w.r.t. to cold operations. The engine models are dual stream nozzles with high bypass to core area ratio of $\mu_A \approx 8$. This allows for classification as an Ultra High Bypass Ratio (UHBR) engine. The model is geometrically scaled down with the same scaling coefficient as the wing ($1 : 14.67$) which corresponds to a characteristic bypass outlet diameter around $D \approx 160\,\mathrm{mm} (\approx 6.3'')$.

The models do not contain any rotating parts, e.g. there are not any fan blades. The most important geometrical features are the nozzle outlets and their positioning (see figure 3.2). The ducts, i.e. bypass (outer) and core (inner) duct, are axisymmetrically coaligned. The engine type can be classified as a short cowl nozzle as the nozzle outlet areas are positioned with a positive protrusion ($L_p > 0$). Thus, at the nozzle outlet planes, there are two separate flows which mix externally. The geometrical outlet areas can be estimated as the lateral surface of a truncated cone and look like Belleville washers.

The core duct is fixed to the bypass duct by three NACA0012 guide vanes, which are equally distributed around the circumference ($120\,^{\circ}$) of the bypass duct (compare figure 3.2). In a similar fashion, the nozzle plug is fixed to the core duct.

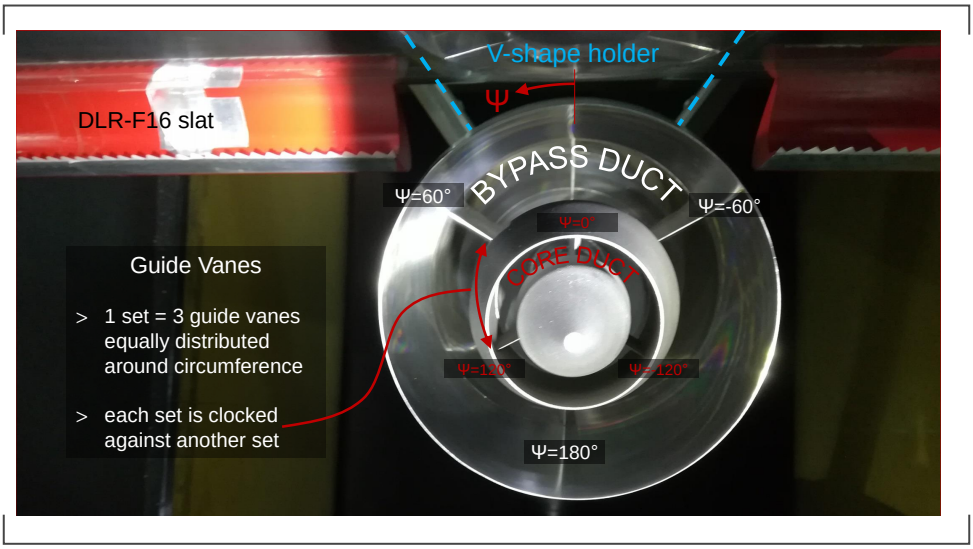

Figure 3.2.: **Engine outlet with view into bypass duct and core duct.**

Assembly The engine is mounted to the wind tunnel pipe and fixed to the wind tunnel by a V-shaped support system. The "V" results from the mounting of the two struts which are partly covered with fabric in order to prevent leading edge sound sources from turbulent inflow. The engine is not mounted to the wing (no pylon), but positioned by a positioning device.

Aerodynamic similarity w.r.t. cold testing Cold compressed air wind tunnel tests are conducted with the best intention that the data can be compared well with hot conditions. This comes with some restraints: Since the tested core exhaust temperature is too low (e.g. by factor 2.25), the core exhaust mass flow rate is too large as well as local speed of sound too low (i.e. by factor 1.5). Therefore, some core exhaust velocities may be subsonic for the hot real conditions, yet supersonic for the cold core model. A supersonic cold core would require a core duct modification and may be parasitic to engine acoustics. Therefore, the core flow in cold tests is kept subsonic.

The combination of low total temperature humid air flow and close to sonic core exhaust velocities cause very low static temperatures and enable water condensation and even ice formation. This can be prevented by moderate heating or compressed air dryers with dew points around $-40\,^{\circ}\mathrm{C}$ (not installed at AWB).

For the interaction of mainly outer flow features with wing and flap, such as the bypass jet potential core and the outer shear layer, the cold core flow is a good approximation to hot conditions:

This is because the *local similarity* (see George [18]) for bypass and co-flow can be preserved (see Jente et al. [26]), even if the core and inner shear layer region may not be similar. This is especially the case for studying engines with large bypass to core area ratios (e.g. UHBR) and works well for near unity and inverted jet profiles (normal jet velocity profiles with high core thrust settings are more challenging, yet also to some extent limited due to the sonic limit).

Given the thermal restrictions of the test rig there is an aerodynamic argument to downsize the ideally hot core nozzle to a cold core nozzle of similar thrust (same mixed jet speed). Yet, the merely geometrically scaled core nozzle approximates geometrical features (mixed jet diameter, shear layer position) much better and is therefore favored for acoustical studies. Jente et al. [26] found that this nozzle shows a dimensional similarity w.r.t. the stagnation enthalpy flow rate $\dot{H}_0$, i.e. the characteristic energy conservation property of the jet.

3.3. Jet aerodynamics

Three-fold multi flow radial to engine axis Flight jet operations are characterized by three flows, which are spatially defined along the direction radial to the engine axis, see figure 3.3): core stream, bypass stream and flight stream[3]. In the free field ambient, the core jet diameter is approximated by the core nozzle outlet area equivalent. This core potential flow can be interpreted as a geometrical support for the bypass potential flow. The flow potentials are separated by a mixing layer, whereby the mixing between bypass and core is referred to as inner shear layer (ISL) and the mixing of bypass and flight stream is referred to as outer shear layer (OSL).

For reason of simplification, bypass and core stream are often summarized to their mixed jet properties (see appendix A). For most of the common operational conditions (i.e. near unity velocity profiles) at a short cowl UHBR nozzle, the mixed jet diameters are approximately constant and mixing velocities are fairly similar to the bypass velocity.

Aerodynamic Specs w.r.t. streamwise flow regions The internal flow conditions in the engine ducts have to adapt to the external flow condition of the free field. The physical process can be described in three streamwise jet mixing regions (see figure 3.4): the near field region, a transitional region as well as the fully-merged region.

[3]This name is used during flight (tests). In wind tunnel tests, it is called wind tunnel velocity, in order to differentiate between the two different acoustical experiments.

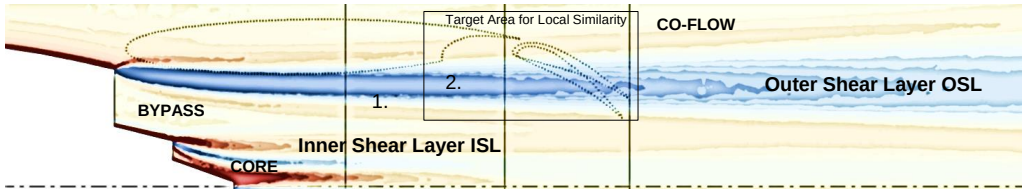

Figure 3.3.: **Multi-flow regions (radial property) indicated by zero vorticity flow regions (yellow) and non-zero vorticity flow (blue, red)**

1. The **near field region** (also referred to as initial merging region) is characterized by the length of the jet potential core. The jet flow transits from an internal (duct) flow into an external (free field) flow, thereby interacting with the ambient co-flow (i.e. the flight stream). This causes the outer shear layer to formulate around the trailing edge. The shear layer expands in streamwise direction until the potential flow is completely decimated. The potential core length of a static jet is estimated with a length of $L \approx 5 \ldots 7 \cdot D_{mix}$. Since the flap trailing edge can be approximated at a horizontal distance of $L \approx 2 \ldots 3 \cdot D_{mix}$ from the bypass nozzle outlet, the initial merging region physics are essential to understanding jet-flap interaction.

2. In the **transition region**, larger vortex scales formulate around a spatially limited arc along the circumference of the mixed jet. This process increases in streamwise direction until the vortex is uninterrupted along the circumference. The mixing changes to a rather turbulent mixing process.

3. The **fully merged region** is a region of self similarity of the jet in the free field. The mixing is completely driven by turbulent mechanisms. The aforementioned large vortex scales cause the low frequency peak of the jet noise spectrum.

3.4. Jet noise

The characterizing part of jet noise is the low frequency peak which is generated in the self-similarity region of the jet and located in the rearward arc. The shape of a typical jet noise spectrum has been empirically defined by Tam and Ariault [45] as well as Tam and Zaman [48]. They use two model functions of Sound pressure Level, F and G, which are normalized w.r.t. the peak of the spectrum. This means, the non-dimensional frequency must be multiplied with the peak frequency and

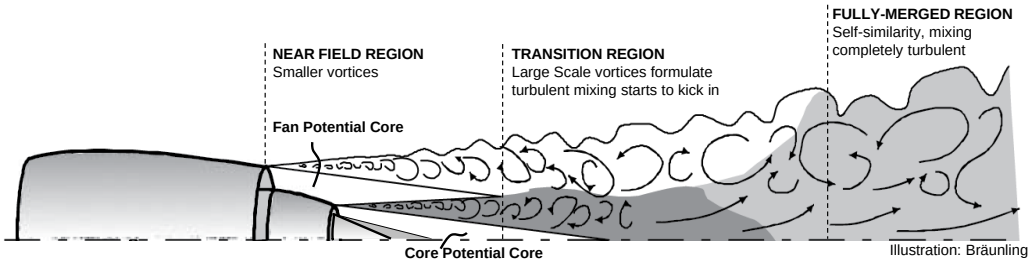

Figure 3.4.: **Jet flow regions, streamwise (adapted from Bräunling [6], p. 1276)**

the peak SPL must be added to function F, G or a superposition of F and G (see figure 3.5). According to Tam, F-noise is a function which fits very well to the noise caused by large turbulence structures and instability waves. G-noise is a function which fits well to fine-scale turbulence which can be measured with the microphones close to the flyover position ($\theta = 90\,°$) and rear arc. In comparison with low subsonic velocities ($Sr < 2$ good), the spectrum replicates high subsonic velocities ($Sr < 5$ good) slightly better (see figure 3.5).

This indicates that jet noise does not only consist of a single acoustic mechanism. When comparing dual stream and single stream nozzles, the noise stemming from the outer shear layer region is vital, even though this flow feature is present for both nozzle types. The difference is that short cowl dual stream nozzles cause mixing diameters which are smaller then the bypass diameter. This means, that downstream the bypass nozzle trailing edge, the developing small vortices do not propagate along a straight diameter, but initially along a constricting diameter (until the mixing diameter is reached). In order to accommodate such a constriction, the jet is not fully expanded at the nozzle exit. Tam & Pastouchenko [47] showed that the two acoustical sub-effects are the main contributors to UHBR dual stream noise, at least for industrial operations and the conditions used within this paper.

Nevertheless, certain operation ratios and smaller area ratios can cause other noise components to be crucial. This was shown by Khavaran et al. [29] who developed a model where secondary (i.e. bypass) and primary (i.e. core) jet, the combined jet signal in the transition region and the fully mixed jet signal can be accumulated to calculate the combined jet noise spectrum. Moreover, the studies of Henderson [19] and Segalini [41] showed that trailing edge thickness can cause an unwanted high frequency peak in the spectrum.

Single Jet Noise
(Tam / Zaman 2000)

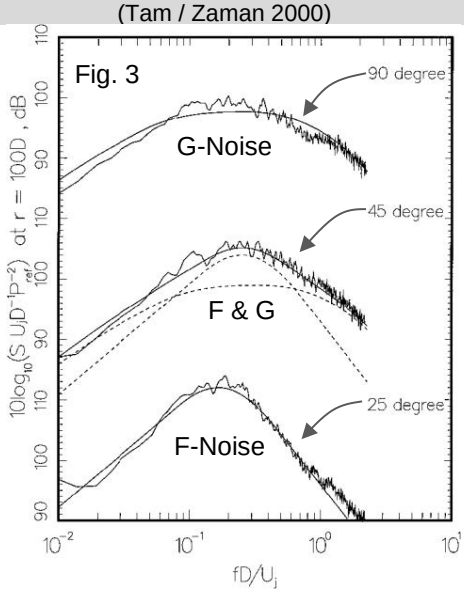

(Tam / Auriault 1999)
Cold jet, Θ=90°

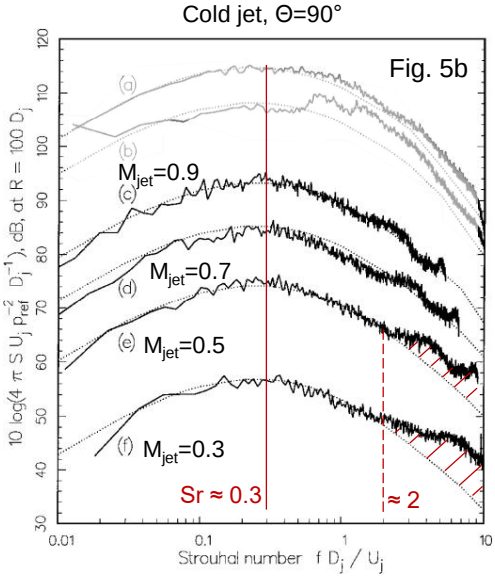

Dual Stream Jet Noise
(Tam / Pastouchenko 2006)

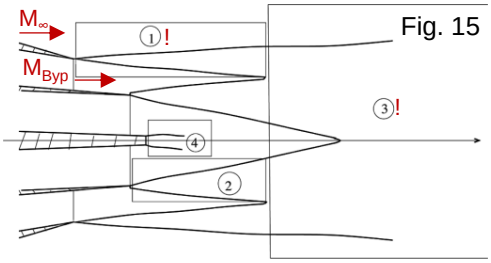

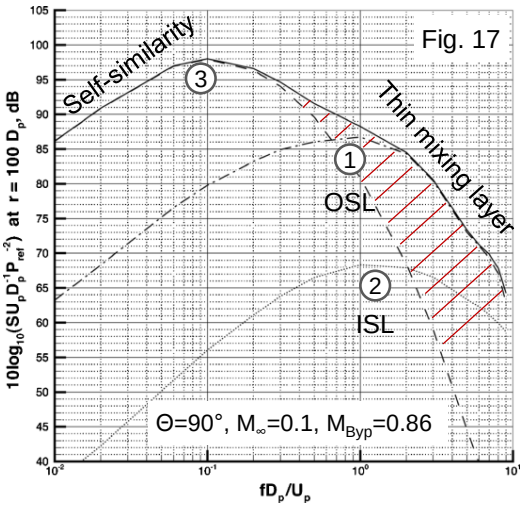

- Static single jet noise spectrum shape and peak Sr depends on angle
- At Θ=90°: jet noise fits well with empirical Tam G-noise model
- Peak narrowband Strouhal number is Sr≈0.3 (Θ=90°), based on jet diameter and velocity
- Model is good for high Mach numbers, there are deviations for low Mach numbers, here: good until Sr ≈ 2
- Dual stream jet: Initial region and thin mixing layer broaden the spectrum

Figure 3.5.: **Jet noise [45], [48], [47]**

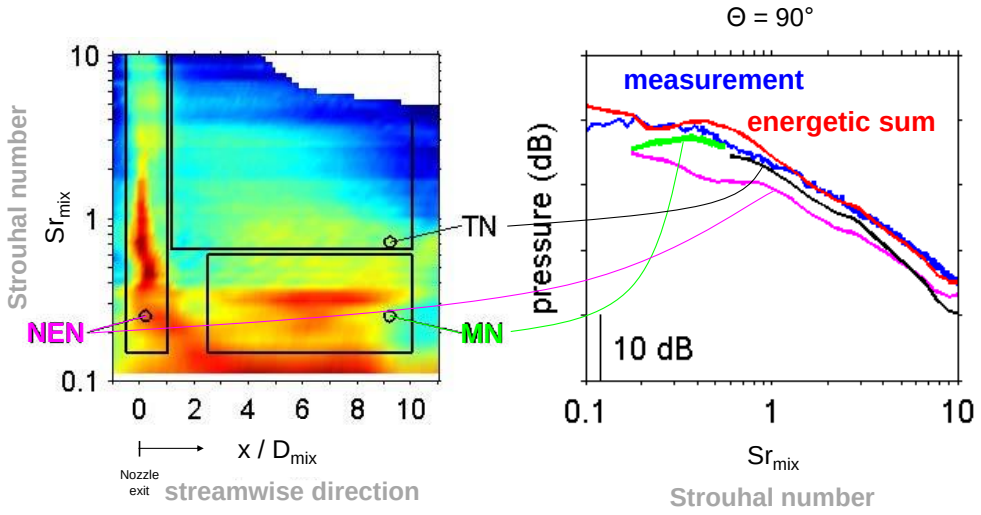

Figure 3.6.: **Jet noise source regions according to Fleury and Davy (ONERA) [15]**

Acoustical specs w.r.t. spatial source analysis Measurements with microphone arrays in combination with source location algorithms, e.g. beamforming, allow to analyse the noise sources. According to Fleury and Davy [15], subsonic jet noise can be characterized by three spatial source regions (see figure 3.6), nozzle exit noise (NEN), turbulent noise (TN) and mixing noise (MN).

- They found that **nozzle exit noise** is a spatial region of strongly correlated noise and it is crucial for the high frequencies. This can be explained by the physics of the initial merging region. The shear layer starts to formulate around the nozzle lip and successively gains in width. The small dimensions allow only rather small turbulent vortex structures to build up.

- The **mixing noise** is generated approximately 4-10 diameters downstream the engine outlet and accounts for the low frequency peak SPL_{max}, which can be found at a Strouhal number of $Sr_{nb} \approx 0.3$, $Sr_{1/3} \approx 1$ (unity).

- The **turbulence noise** region does not show strong sources via source localization analysis. However, the corresponding signal (black curve) is rather strong compared to nozzle exit noise (pink). This could indicate that MN and TN might belong to the same mechanism and together represent the noise originating from the aerodynamic far-field of the jet.

Jet instabilities Instability analysis showed that subsonic jets support a family of upstream and downstream travelling waves [28]. In jet-flap interaction settings, those waves can cause tonal components in the spectrum. This occurs if there is a strong coupling between an upstream and a downstream travelling wave which creates a feedback loop between the trailing edges of nozzle and flap (distance L). Downstream travelling Kelvin-Helmholtz wave-packets are possibly the better known waves, as there are natural phenomena which help to make them visible. Moreover, there are some waves which are distinct features of supersonic flow, but which can also be found in subsonic flow. Jordan [28] referred to this waves as TH-waves which were discovered by Tam & Hu, [46] as well as by Michalke [31] who initially rejected them [28]. There are more waves which are supported by the jet potential core (see Towne [51] and Schmidt [40]). Those are rather relevant for transonic flow velocities ($M > 0.8$) and are not a part of the low Mach number data used in this dissertation.

The key take away of this section is that the engine parameters can be simplified and that the wing is installed with its flap trailing edge at $x/D \approx 2-3$. This is the initial merging zone of an isolated jet where thin shear layer model can be used in order to determine shear layer properties (approximately for $1 < L/D_{mix} < 5$). This means that contrary to the related conventional jet impingement problems (see figure 3.1) the radial flow properties cannot be neglected. In addition to the length L, the jet interaction with an inclined plate of fixed length is also geometrical defined by the "vertical" parameters of the jet at the flap trailing edge position. This requires knowledge about the jet mixing radius R_{mix} and the outer shear layer.

The idea behind the derivations in the following sections is to build a powerful tool by being able to replace any engine by its near-field shear layer properties and providing a framework for comparison of any engine integration.

3.5. Derivation of the shear layer width using thin mixing layer theory

An analytical model (equation 3.1, Eisfeld [14]) is used in order to calculate the local outer shear layer width δ_ω of a planar thin mixing layer model at the streamwise position L (see figure 3.7). The model parameters can be calibrated w.r.t. static jet properties (simplifications: $c_0 = 0.64$, $\sigma_0 \approx 9.2$, $r_{U,OSL} = U_\infty/U_{jet}$, see appendix B.2). The virtual origin of shear layer is positioned at $x_0(\leq 0)$, e.g. $x_0/D_{mix} \approx -0.2$ (for LIST nozzle, see appendix B.3).

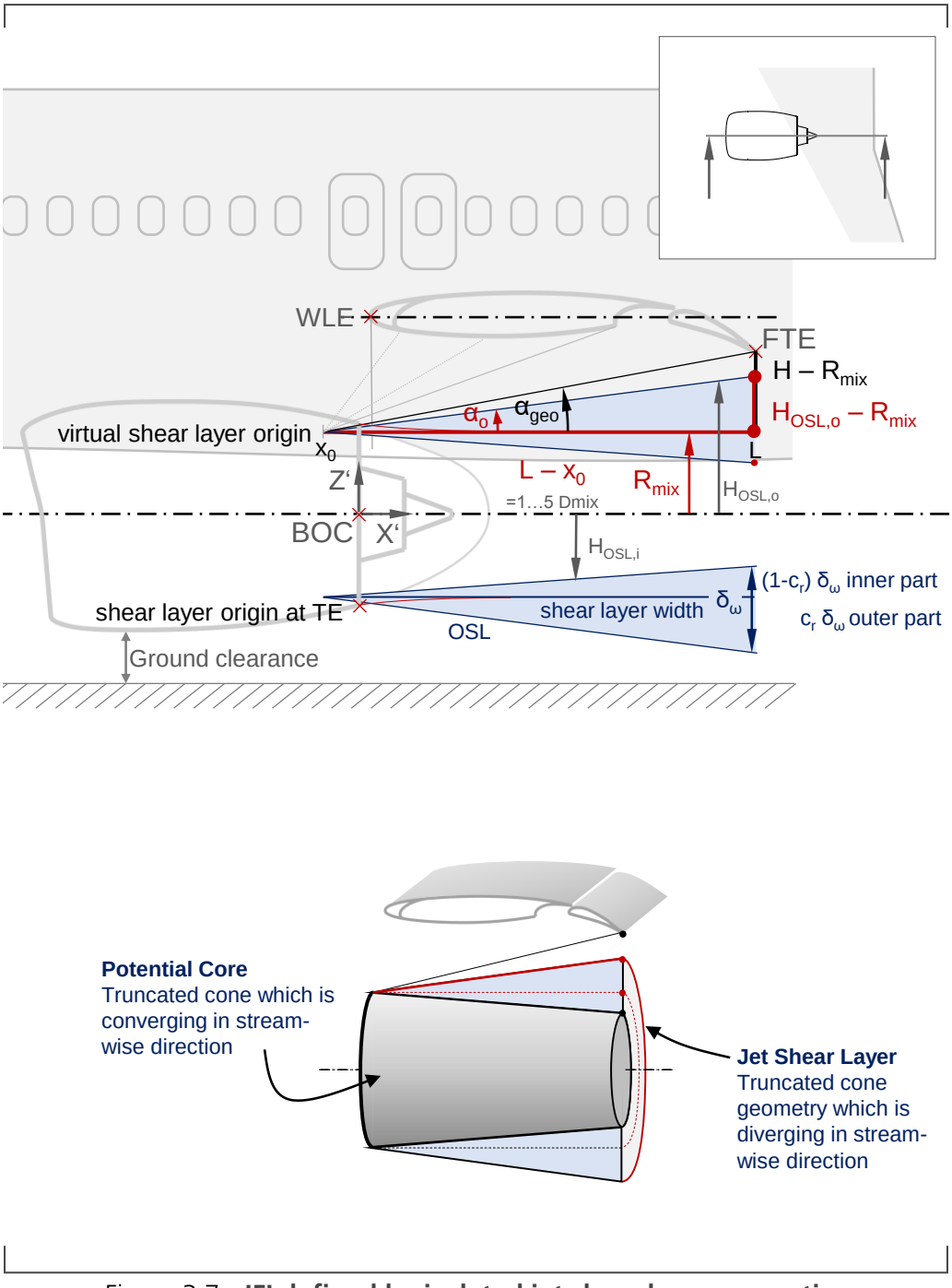

Figure 3.7.: **JFI defined by isolated jet shear layer properties**

$$\delta_\omega = (L - x_0) \cdot \frac{\sqrt{\pi}}{\sigma_0} \frac{1 - r_{U,OSL}}{1 + r_{U,OSL}} \tag{3.1}$$

Contrary to axisymmetric shear layer models where half-jet width coordinates are used, the aerodynamic jet near-field has a more prominent radial characteristic, the mixed jet radius R_{mix}. The shear layer convection velocity U_c happens to be positioned at the mixed jet radius R_{mix} (Jente et al. [24])[4]. A conventionally used formula [33] for its calculation is equation 3.2. For a better fit with the standard thin mixing layer model, it is rewritten as convection parameter function c_U (equation 3.3). The geometric convection parameter function c_r calculates the relative share between the top part of the outer shear layer and the full outer shear layer thickness.

$$U_c = U_\infty + c_0 \cdot (U_{jet} - U_\infty) \tag{3.2}$$

$$c_U := \frac{U_c}{U_{jet} + U_\infty} \approx \underbrace{c_0}_{\approx 0.64} \cdot \frac{1 - r_{U,OSL}}{1 + r_{U,OSL}} + \frac{r_{U,OSL}}{1 + r_{U,OSL}} \tag{3.3}$$

$$c_r := \frac{H_{OSI,o} - R_{mix}}{\delta_\omega} = c_U \cdot \frac{1 + r_{U,OSL}}{1 - r_{U,OSL}} - \frac{r_{U,OSL}}{1 - r_{U,OSL}} \tag{3.4}$$

The mixed jet radius is calculated according to equation 3.5 for isothermal cold jets (appendix A) with its inner shear layer velocity ratio $r_{U,ISL} = U_{Byp}/U_{Core}$. Assuming a high area ratio engine and near unity velocity profiles, most engine operations can be approximated well with $r_{U,ISL} = 1$.

$$R_{mix,cold} = \sqrt{\frac{A_{Byp}}{\pi}} \cdot \sqrt{\left(\frac{(\mu_A \cdot r_{U,ISL} + 1)^2}{(\mu_A \cdot r_{U,ISL})^2 + \mu_A} \right)} \tag{3.5}$$

$$= \begin{cases} \sqrt{A_{Core}/\pi} & r_{U,ISL} = 0 \\ \sqrt{(A_{Byp} + A_{Core})/\pi} & r_{U,ISL} = 1 \\ \sqrt{A_{Byp}/\pi} & r_{U,ISL} = \infty \end{cases} \tag{3.6}$$

The radial jet and shear layer properties can be calculated with equation 3.7:

$$Z' = \begin{cases} H_{OSL,o} = R_{mix} + c_r \cdot \delta_\omega & \text{outer OSL boundary, total jet width} \\ R_{mix} & \text{mixed jet width} \\ H_{OSL,i} = R_{mix} - (1 - c_r) \cdot \delta_\omega & \text{inner OSL boundary to bypass pot. core} \end{cases} \tag{3.7}$$

With the help of the shear layer thickness (equation 3.1), equation 3.7 can be separated into build parameters[5] (left side of equation 3.8) and operational parameters

[4] For single jets w/o nozzle plug, the mixing radius equals the nozzle radius. The shear layer convection velocity can be measured at the nozzle lip line [7].

[5] There are dependencies on operational parameters, which can be assumed quasi-constant for a lot of build comparisons: The mixing radius depends on the ISL velocity ratio; the virtual shear layer origin slightly depends on the OSL velocity ratio.

(right side), also shown by Jente [23]:

$$\underbrace{\frac{Z' - R_{mix}}{L - x_0}}_{\text{left side}} = \begin{cases} \tan(\alpha_o) = c_r \frac{\sqrt{\pi}}{\sigma_0} \frac{1-r_{U,OSL}}{1+r_{U,OSL}}, & \text{for } Z' = H_{OSL,o} \\ \tan(0°) = 0, & \text{for } Z' = R_{mix} \\ \tan(\alpha_i) = (c_r - 1) \frac{\sqrt{\pi}}{\sigma_0} \frac{1-r_{U,OSL}}{1+r_{U,OSL}}, & \text{for } Z' = H_{OSL,i} \end{cases} \tag{3.8}$$

The left side equals the tangent of an angle between the mixed jet radius (a line that is here parallel to the jet axis), and a line along the outer shear layer edge. This angle is rather small ($\alpha_o = 0 \ldots 7\,°$). Hence, small changes in length are less sensitive than small changes in height.

The characteristic angles of the jet shear layer (equation 3.8) can be compared with the real installed angle (equation 3.9) between mixed jet radius, virtual shear layer origin and the flap trailing edge ($Z' = H$).

$$\tan(\alpha_{FTE}) = \frac{H - R_{mix}}{L - x_0} \tag{3.9}$$

The installation angle and the shear layer angle symbolize 1D similarity of the JFI problem, yet they are not the similarity parameter: The mathematical uniqueness of a triangle cannot be defined by angles on their own. Rather, the height difference $Z' - R_{mix}$ in combination with the length difference $L - x_0$ are more suited for the geometric problem description. An in-depth analysis and corresponding measurement methods are described in chapter 6.

Nevertheless, the angle definition allows to create the most general formulation of a so-called jet-flap diagram (see figure 3.8). The jet-flap diagram allows to compare the space requirements of an isolated jet shear layer for any velocity ratio $r_{U,OSL}$ and the constriction due to build height at the flap TE. In addition to the flap TE, the entire wing contour can be plotted into the same diagram. Thereby, any geometric space conflicts of the isolated shear layer can be displayed. This includes space conflicts with the main wing.

For the first part of the dissertation, a constant mixing radius as well as a constant length are chosen. For such a specific build comparison, the height is the only relevant variable. It is used within a simplified jet-flap diagram $Z'(r_{U,OSL})$ which may be easier to comprehend.

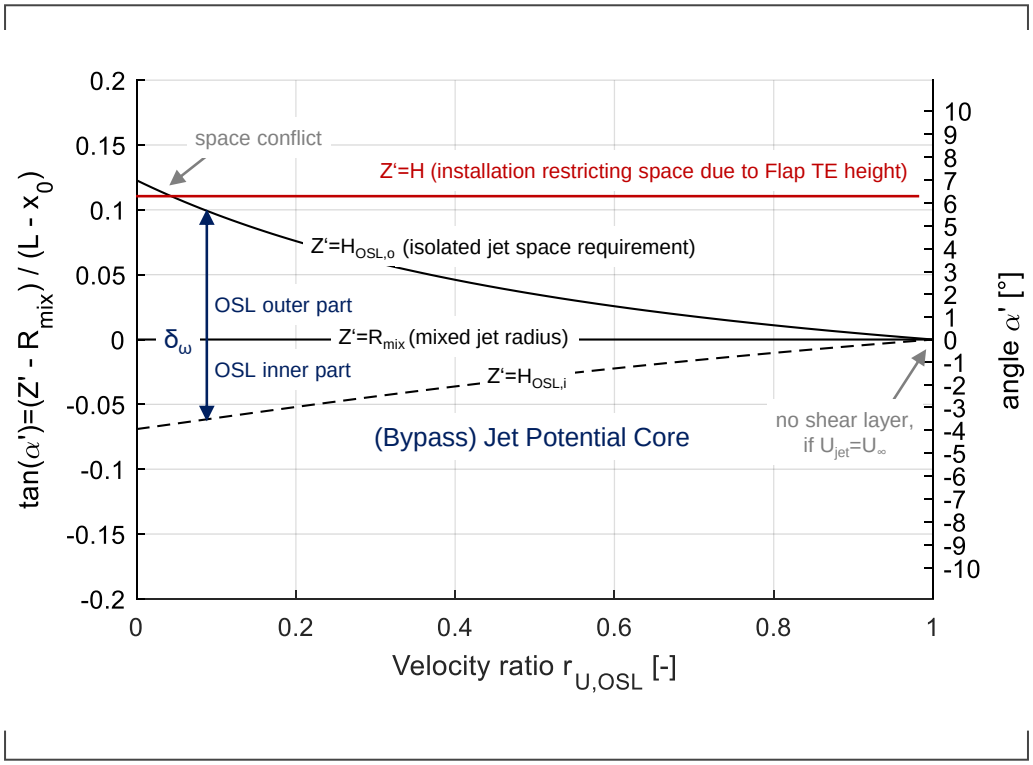

Figure 3.8.: **Jet-flap diagram: space requirements of isolated jet shear layer vs. build height for different operations.**

3.6. Derivation of the Flap Boundary Layer thickness

The flap boundary layer is approximated by flow over a flat plate with length of the flap chord length $x \approx c_{flap}$. The boundary layer thickness can be estimated using equations 3.10 to 3.12.

$$\delta_{BL,flap} = \begin{cases} 4.91 \cdot x \cdot Re_x^{-1/2} & \text{, if } Re_x < 5 \times 10^5 \text{ (laminar)} \\ 0.37 \cdot x \cdot Re_x^{-1/5} & \text{, if } Re_x > 5 \times 10^5 \text{ (turbulent)} \end{cases} \tag{3.10}$$

$$\text{using } Re_x = \frac{U_\infty x}{\nu} = \frac{60\,\mathrm{m/s} \cdot x}{1.47 \times 10^{-5}\,\mathrm{m^2/s}} = \begin{cases} 4 \times 10^5 & \text{model scale} \\ 6 \times 10^6 & \text{full scale} \end{cases} \tag{3.11}$$

$$\frac{\delta_{BL,flap}}{D_{mix}} \approx \begin{cases} 0.006 & \text{model scale} \\ 0.012 & \text{full scale} \end{cases} \tag{3.12}$$

The approximations in model scale and full scale (equation 3.12) indicate that there is good reason to neglect the flap boundary layer thickness for its small dimension compared to the mixed jet diameter. For simplicity reasons, the flap boundary layer thickness will not be part in the further discourse of this thesis.

3.7. Acoustic measurement and evaluation of quasi-static JFI

For the first example, the third-octave spectra of the installed engine setup is compared against the isolated engine (figure 3.9, left). For all data points, the engine is operated in static condition, i.e. the wind tunnel flow is switched off.

Method For a single evaluation of the jet-flap effect ΔSPL_{JFI} in static condition, at least two data points must be measured, i.e. two signal data points. The measurement of the data points requires 2 builds, the isolated engine build as well as the installed engine build. The measured spectra are corrected and normalized by state of the art correction methods (see appendix C).

The background correction is optional for static engine tests. It can be (1) either omitted (background noise is dimensionally negligible) or (2) done against the two zero data points (wind tunnel off, engine off). As AWB is a circuit wind tunnel, a third

background data point option is thinkable, i.e. the testing against low wind tunnel velocities $U_\infty \leq 10\,\mathrm{m/s}$. However, this setting has not yet been tested, because the axial AWB fan would be operating at an unstable region and may possibly introduce new noise sources which are not present when the AWB fan is switched off.

There are two data points which can be compared, the corrected installed noise level $SPL_{installed}$ as well as the corrected isolated engine noise SPL_{jet}. The interaction effect (figure 3.9) can be evaluated by calculating the additional noise ΔSPL_{JFI} which is generated by the presence of the wing. It is common practise in the industry to measure the installed noise $SPL_{installed}$ of any jet-related physical effect and to (arithmetically) subtract the isolated engine noise SPL_{jet} from the total noise in order to get the arithmetic difference in SPL (equation 3.13):

$$\Delta SPL_{JFI} = SPL_{installed} - SPL_{jet} \tag{3.13}$$

Research questions: The test objective is to vary the installation height H of the wing and engine. A wing which is installed in large distance to the engine axis has in theory no influence on the jet and does only serve as a reflective surface. But how close can the wing be installed in order to still be negligible compared to isolated engine noise? (1) What is the minimum engine integration height that causes no jet-flap interaction delta? And: (2) When moving closer to the jet axis, how can jet-flap interaction be characterized in terms of spectrum and frequency?

Results: The installed JFI noise is characterized by a broadband-like offset on top of the isolated jet noise spectrum. JFI tones are more prominent at higher subsonic jet Mach numbers (e.g. $M \geq 0.6$) rather than lower jet Mach numbers. Since narrowband plots can look cluttered compared to third-octave band data, a low jet Mach number (here at $U_{jet} = 160\,\mathrm{m/s}$) is displayed. The jet-flap interaction effect can be clustered by three frequency ranges, which are here defined by the labels low, mid and high. Cavalieri et al. [10] found that the JFI effect follows a Helmholtz analogy. Therefore, the corresponding Helmholtz number (rather than the Strouhal number) is given.

- The mid frequency JFI delta contains the characteristic feature of the effect, i.e. a rather broadband-like peak of $10 - 15\,\mathrm{dB}$ around $He_L = 1$ (large bandwidth). JFI tones show up at high Mach number and can easily exceed jet noise by $20 - 30\,\mathrm{dB}$. The broadband part of the noise is comparably indifferent with respected to changing jet speed [27], yet sensitive to changing engine integration height: mid-frequency JFI noise is maximal when the flap trailing edge disturbs the outer shear layer (figure 3.9, left).

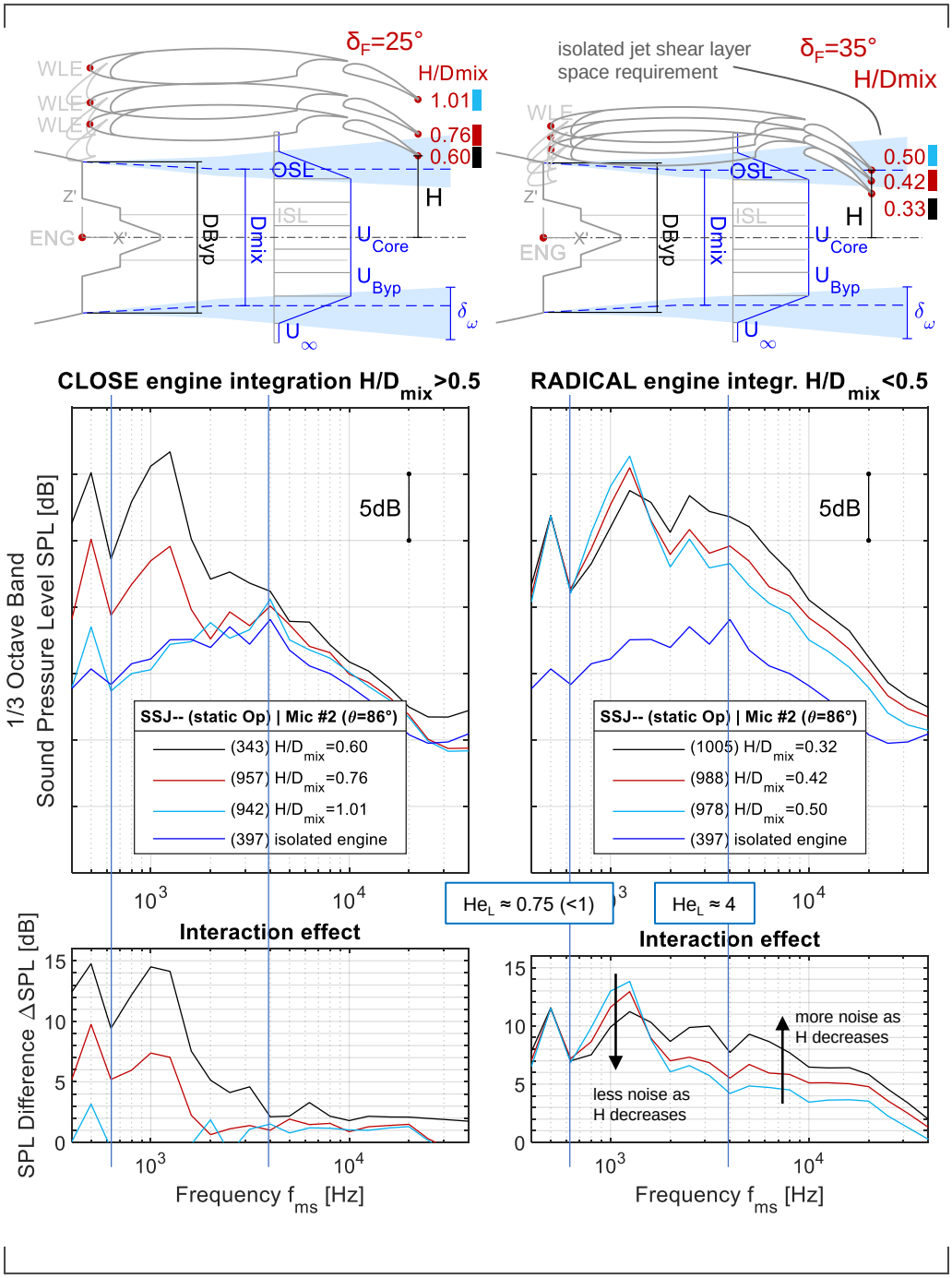

Figure 3.9.: **Isolated engine and height variations of installed engine operated at 160m/s (same speed jet)**

  - **mid frequency JFI effect**: $0.75 \leq He_L \leq\approx 4$ ($800\,\text{Hz} \leq f_{1/3,ms} \leq 3150\,\text{Hz}$)

- The low frequency JFI delta is characterized by an anomaly [23] [27]: Low jet speed causes a higher low frequency JFI delta than high jet speed. According to Michel [34] the high noise at low speeds compared to high jet speeds results from a slow decay of the pressure wave's representing eigenfunctions of the shear layer linear instability.
  The spectrum consists of one peak with a rather broad bandwidth, but does not show any sharp tones. Multiple peaks or waviness in the spectrum results from the wing being finite in length: The low frequency JFI delta changes with different chord length of the wing or plate [27].

  - **low frequency JFI effect**: $He_L \leq 0.75$ ($400\,\text{Hz} \leq f_{1/3,ms} \leq 630\,\text{Hz}$)

- The high frequency JFI delta is defined by the absence of tones. The magnitude of the JFI effect is small ($0 \ldots 1\,\text{dB}$) for industry relevant engine integration, yet can even increase to $7 \ldots 10\,\text{dB}$ (figure 3.9, right).

  - **high-frequency JFI effect**: $He_L \geq\approx 4$ ($4\,\text{kHz} \leq f_{1/3,ms} \leq 40\,\text{kHz}$)

The minimum engine integration height where jet-flap interaction can be neglected (in the wind tunnel experiment) is located at $H/D_{mix} \approx 1$. This corresponds to a build angle of $\alpha_{geo} \approx 9.5\,°$. The installation distance where jet-flap interaction is negligible is approximately one mixed jet diameter (i.e. $\approx 0.8 \ldots 0.9$ engine diameters). This provokes the question why jet-flap-interaction noise is not already a massive problem in current installations: A modern mid range aircraft may just barely have such a one mixed diameter engine integration height during cruise (clean chord flap, i.e. maximum distance H). During take-off and landing, the flaps are deployed and decrease the free height H below the margin of one mixed jet diameter. This may lead to the conclusion that jet-flap interaction should already play its role in the noise mix.

Radically integrated heights may be defined by distances which limit the space at the flap trailing jet below the mixed jet radius, i.e. $H \leq 0.5 D_{mix}$. Such builds influence especially the high frequency JFI effect (see right side of figure 3.9). Some third-octave bands can accumulate a jet-flap interaction noise of up to $\Delta SPL = 7 \ldots 10\,\text{dB}$. Contrary to the high frequency increase, the low frequency peak does not change in jet-flap interaction delta. The mid frequency peak even decreases for radical heights.
This behavior of varying qualitative sensitivity of low-, mid- and high frequency JFI

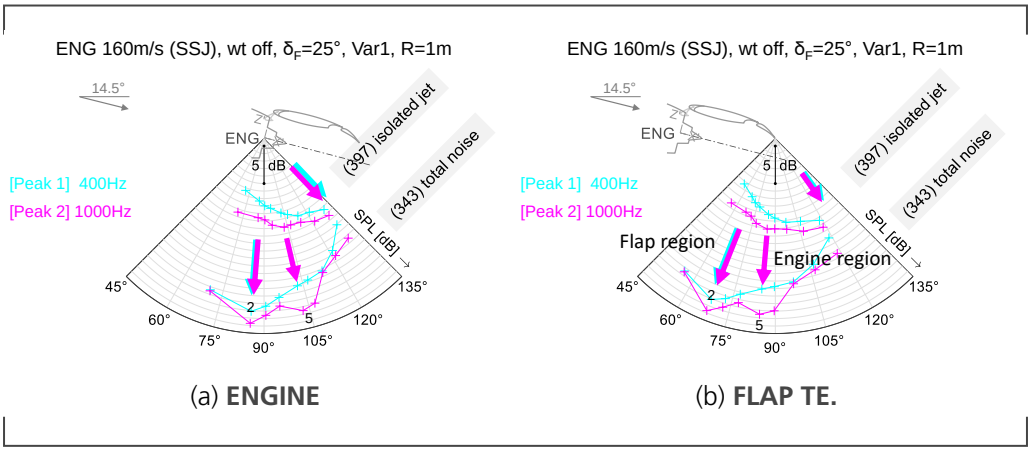

(a) **ENGINE** (b) **FLAP TE.**

Figure 3.10.: **Directivity depending on measurement reference point**

noise w.r.t. both engine integration height and operations shows how complex a SPL or OASPL estimation is.

Directivity Jet-flap interaction noise consists of multiple noise components. With the help of microphone array measurements and a beamforming algorithm, it is possible to detect the engine related sources (nozzle exit noise, mixing noise), jet-flap interaction as well as high-lift wing noise.
Those sources are fairly concentrated in comparison to the low frequency noise peak of the isolated jet (which is located at $4 \ldots 10 \cdot D_{mix}$) downstream the engine. In the test setup used in this work microphones are positioned at $R \approx 7 D_{mix}$ under the engine, which corresponds to the acoustic "mid"-field rather than the far-field. Thus, the noise source region is not negligibly small compared to the microphone distance. The directivity of the signal would be more reliable with a larger microphone distance.
As a general rule, the following directivity should be expected (compare figure 3.10): Isolated jet noise is directed into the rearward arc and peaks around $\theta_{ENG.MRP} = 160\,^{\circ}$ [45]. The microphone placement does not allow to show this information in figure 3.10a). The installed jet noise measurement shows two peaks: the low frequency JFI peak at 400 Hz is greatest at mic #2, whereas the mid frequency JFI peak at 1000 Hz is great at mic #2 and mic #5. Since mic #2 captures both, it is a good option for evaluation.
The hump at mic #5 is interesting. Since a static jet is examined, this noise could relate to a jet noise source, e.g. NEN (Fleury and Davy [15], compare figure 3.6).

Conclusion: A Jet-flap interaction geometric model, measurement procedure and evaluation method were developed for the simplest case at static operations. This is

in general a useful method for operations which are defined by high thrust settings and low flight speed. The geometric model is an advance to the use of horizontal proximity ratio ($HPR = L/D$) and vertical proximity ratio ($VPR = H/D$) [42] between bypass outlet center plane and flap trailing edge. In order to study some more sophisticated jet-flap interaction problems with a higher wind tunnel velocity, corresponding methods and their evaluation limits are studied in chapter 4.

4. Acoustic influence of the slat: JFI as a multi-source problem

In chapter 3, the jet-flap interaction noise problem was studied from the perspective of a strong jet noise source. It is a common procedure in the engine industry, e.g. to compare build effects against the isolated jet noise. This method is only good because the engine is operated in static mode (i.e. no wind tunnel speed). It could be granted that there are no other relevant aircraft noise sources present, especially no conventional high-lift wing noise except the effect of the flap in the region of jet impact as described.

However, this changes when high wind tunnel speeds and low thrust settings need to be measured. Then the perspective changes, and the evaluation of jet-flap interaction noise becomes more sophisticated because high-lift wing noise is a vital part of the noise mix. Let us take a look at the so-called approach of an airplane to the airport. This point of operation is an important certification point of an aircraft and specified by ICAO annex 16. The engine operates at comparably low settings whereas the flight speed is rather high. Especially slat-related high-lift wing noise becomes acoustically relevant.

Moreover, it must be checked whether engine integration sources other than jet-flap interaction become relevant. This concerns the interaction between engine, slat and pylon. The measured interaction noise is in general a sum of all the effects which stem from integrating the engine under the wing. Conclusions on jet-flap interaction can only be drawn as long as the other interaction noise sources remain constant or can be isolated.

Thus, this chapter will focus on how JFI noise can be measured. It will not be structured for modelling of the slat region because other engine integration sources are out of scope for this dissertation. Nevertheless, the presence of other noise sources shows that the JFI problem is not a single source, but a multi-source problem which needs its own evaluation. Consequently, the guiding questions which are targeted in this chapter are:

- How can jet-flap interaction noise be isolated from other engine integration

noise sources?
The experiment must be designed in order to avoid additional noise due to interaction of engine, slat and pylon. It must be shown, that noise in the region close to the engine does not really change compared to the jet induced noise coming from the flap.

- There must be a method to study the installed noise of the jet-flap interaction build in comparison to isolated high-lift wing noise and isolated jet noise.
  How does this affect the determination of jet-flap interaction noise?

- And how can a jet-flap interaction noise test be designed within the boundary conditions of a wind-tunnel-environment?
  Contrary to the aircraft, the installation of the model differs slightly in the experiment - hopefully with negligible compromise. This installation provides its own unwanted noise sources. The quality of the measured data must be secured against any of such unwanted (background) noise sources.

Hence, the wanted and unwanted noise sources in the wind tunnel experiment must be identified (section 4.1). Then, an analysis can be made in two steps. In the intial step, each of the two wanted noise sources must be individually studied in terms of how well can they be measured in comparison to background noise sources (appendix E). In the more important second step the operational limits are identified when the multi-source problem can be simplified to a quasi-single source problem (section 4.2). As a result, additions to the jet-flap diagram can be made (section 4.3). This may be used to define different measurement and evaluation techniques depending on the goal of a test campaign (section 4.4).

4.1. Wanted and unwanted noise sources in the wind tunnel experiment

In this section, the noise mix of the wind tunnel experiment is studied. The wind tunnel experiment does not only contain aircraft relevant sources, but also some sources which are only present in the experiment. Those wanted (section 4.1.2) and unwanted (section 4.1.1) noise sources must be identified qualitatively and, as far as this is possible, quantified.

Figure 4.1 shows the noise sources of the experiment. The wanted noise sources are high-lift wing noise sources (black), jet noise sources (dark blue) and sources related to the engine integration (light blue). The unwanted noise sources are marked in

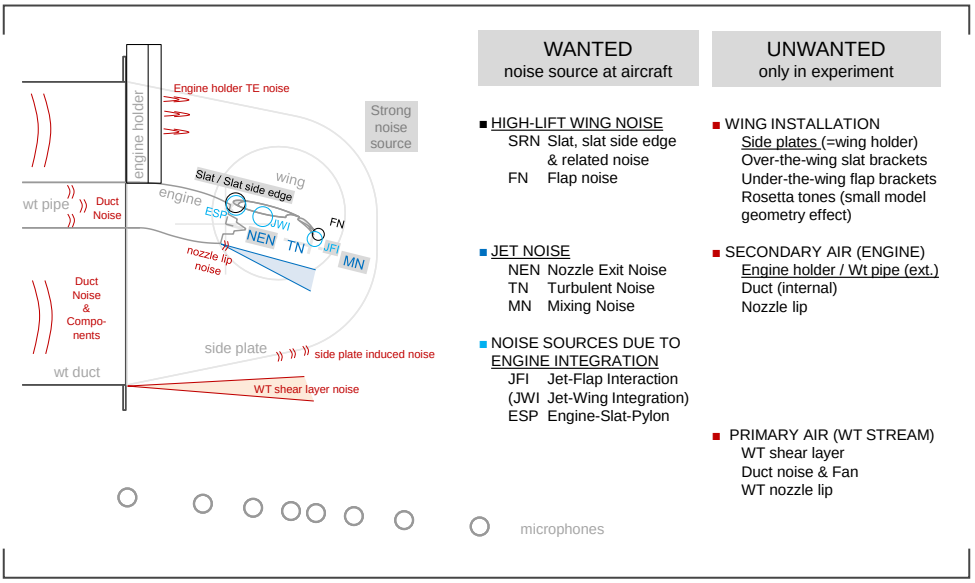

Figure 4.1.: **Noise sources at aircraft and wind tunnel experiment**

red.

4.1.1. Unwanted noise sources

Most of the unwanted noise sources are specified to be negligible by design. For example, there are design criteria for engine ducts (duct noise) or trailing edge thickness (minimal nozzle lip noise). Some of the source noise misinterpretation effects can be corrected by theory (e.g. the wind tunnel shear layer, see Amiet [1]). Some installation noises cannot be measured very well (e.g. over-the-wing slat brackets), but some build effects can be isolated by comparing installations:

- Let us start with an empty wind tunnel (see figure 4.2, magenta). Since the wind tunnel is in operation at fixed speed of $60\,\mathrm{m/s}$ for all the following data points, a shear layer is produced (peak at very low frequency $\approx 10^1$ Hz). The spectrum is expected to decrease monotonously from low to high frequencies. Wind tunnel duct noise, the axial fan, the nozzle lip, and other noise sources add up to the final empty wind tunnel spectrum. This is the lowest background noise available and is referred to as build $\#0$ in this section.

- Side plates are needed in order to hold the wing. Their installation produces a minimal[1] offset to the spectrum of $\approx 2\,\mathrm{dB}$ (see green spectrum). The

[1] For lower wind tunnel velocities the effect is even smaller.

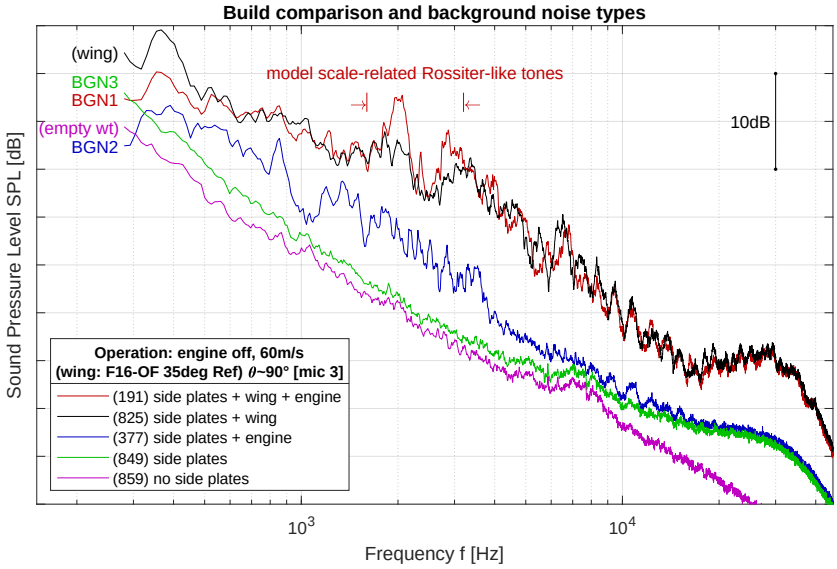

Figure 4.2.: **Identifying noise sources by adding components**

offset is slightly higher for very low and very high frequencies $f \geq 9\,\mathrm{kHz}$. This installation setup has been defined as BGN3 here, which stands for background noise build #3.

- The engine is attached to the wind tunnel nozzle outlet frame by a V-shaped holder, and the secondary air is supplied via the so-called wind tunnel pipe (wt pipe). In combination with the side plate this test setup can be used to produce a BGN2 data point (condition: no jet velocity). BGN2 is one of the most frequencyly used background sets that are measured.
  The BGN2 spectrum (blue) is approximately $\approx 5\,\mathrm{dB}$ higher than the BGN3 spectrum in the low and mid frequencies. The high frequencies are similar to BGN3, which might be caused by the influence of the side plates. Note that the spectrum is less smooth; it partly deviates with $\approx \pm 2\,\mathrm{dB}$ around its averaged spectrum curve.

- If the wing is installed to BGN2, the so-called *installed engine* test build for the jet-flap interaction noise test is complete. Operating the engine without jet velocity causes a background noise #1 measurement (red). The BGN1 measurement is not always useful as a background noise and can only be used for special cases. However, it is very similar to an isolated wing signal measurement (build 4), and can be used as a so-called *integrated wing measurement*. The integrated wing measurement is a measurement where the

engine is integrated onto a wing, yet it does not produce any thrust.

- The isolated wing sound pressure levels (black) are of the same dimension as the integrated wing and up to 10 dB higher than BGN2. For the measurement, the engine (including wt pipe and holder) is removed, the side plates and the wing are installed.

If the unwanted installation noise sources are too loud, then they cannot be neglected in the experiment. It is advised not only to test the background noise mix, but also to actively work on noise reduction, especially for holders. Some noise reduction measures are filling holes with modeling clay, taping over or smoothing out unwanted edges or applying serrations.

4.1.2. Wanted (aircraft-relevant) noise sources

For the evaluation of interaction noise, it is recommended to measure the two other groups of wanted aircraft-relevant noise sources individually: engine-related noise sources and high-lift wing related noise sources.

Isolated jet noise has been previously described in section 3.2, where the specifications of the jet engine are also listed.

The wanted wing-related noise sources depend on the number and type of elements of the wing:

- For a typical three-element wing, there are slat and slat-related noise sources as well as flap noise. Flap noise is very often negligible in comparison to slat noise.

- A two-element wing with a main wing and a flap is a bit more difficult to measure, as or if the measured signal to noise ratio is low.

A very exciting field and boundary condition for studying jet-flap interaction is an engine integration design which is prone to measure a sufficiently high jet-flap interaction signal and very low other interaction effects. The F16 high-lift wing has been studied in appendix D for this purpose.

4.2. Operation limits for reducing wanted multi-noise sources to quasi-single

In the jet-flap interaction build, two actual aircraft noise sources are present which can also be isolated, i.e. isolated jet noise and isolated high-lift wing noise. The combination of both of the sources represents the signal, which is also the best guess or baseline when testing a jet-flap interaction build. Two uncorrelated sources can be combined by energetically adding both of them (see equation 4.1).

$$SPL_e = \lg \Sigma(\text{iso.jet, iso.wing}) = 10 \cdot \log_{10}\left(10^{SPL_{iso.jet}/10} + 10^{SPL_{iso.wing}/10}\right) \tag{4.1}$$

If there is jet-flap interaction, the additional sound pressure level ΔSPL_{JFI} can be calculated by subtracting the energetic sum (equation 4.1) from the installed signal $SPL_{installed}$.[2]

$$\Delta SPL_{JFI} = SPL_{installed} - SPL_e \tag{4.2}$$

There are cases in which either isolated jet noise or isolated high-lift wing noise can be dimensionally neglected against one another (see equation 4.3).

$$SPL_e \approx \begin{cases} SPL_{iso.jet}, & \text{if } SPL_{iso.jet} \gg SPL_{iso.wing} \\ SPL_{iso.wing}, & \text{if } SPL_{iso.wing} \gg SPL_{iso.jet} \end{cases} \tag{4.3}$$

If the difference between the two noise sources is $6.9\,\text{dB}$, the energetic sum SPL_e is underestimated by $1\,\text{dB}$. If this difference is $9.6\,\text{dB}(\approx 10\,\text{dB})$ the energetic sum SPL_e is underestimated by $0.5\,\text{dB}$ (see table E.1).

Isolated jet noise (here for a same speed jet, $r_{U,ISL} = 1$) and isolated high-lift wing noise have been compared as quasi-single sources against their combination as an energetic sum (see figure 4.3).

$$\begin{cases} \text{baseline:} & SPL_e - SPL_e = 0\,\text{dB} \\ \text{blue:} & SPL_{iso.jet} - SPL_e \\ \text{black:} & SPL_{iso.wing} - SPL_e \end{cases} \tag{4.4}$$

There are some cases in which an isolated noise is very similar to the combined noise. The identifying parameter is rather the velocity ratio than the difference velocity, which can be derived from figure 4.3. This analysis has been conducted for the same

[2] Other sources do not work with jet-flap interaction deltas, but use a logarithmic subtraction. The logarithmic subtraction may only have a solution in complex numbers for high frequencies. Therefore, it was decided to use arithmetic deltas rather than logarithmic subtraction.

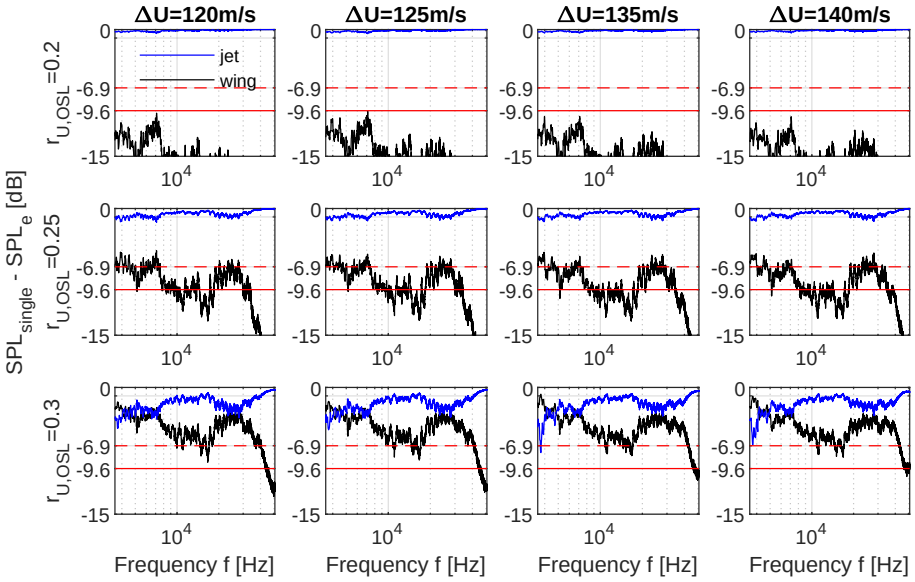

Figure 4.3.: **Contribution of isolated jet noise (same speed jets) and high lift wing noise to the energetic sum of both isolated noise components.**

engines and frequency ranges as before. The evaluation is based on a rather small number of operational data points (≈ 10 for P25H and ≈ 30 for LIST engine) and a velocity ratio range of $0 < r_{U,OSL} < 0.47$. Therefore, the real results may deviate from the results in table 4.1.

Table 4.1.: **Evaluation limits for quasi-single source**

		STRONG JET		**JET = WING**		**STRONG WING**	
		$r_{U,OSL} < \ldots$		$r_{U,OSL} = \ldots$		$r_{U,OSL} > \ldots$	
frequency range	$f_{1/3,m}$ [Hz]	P25H	LIST	P25H	LIST	P25H	LIST
low	315 . . . 630 Hz	< 0.19	< 0.2	0.25	0.25	≈ 0.47	≤ 0.47
mid	800 . . . 3150 Hz	0.19	≈ 0.2	0.35	0.35	> 0.47	> 0.47
high	4 . . . 40 kHz	≈ 0.22	0.33	0.38	0.38	> 0.47	0.47

Such a table is valuable because it indicates build setups with strong jet noise as well as strong high-lift wing noise. Take, for example, the evaluation of the full scale relevant frequency range where the LIST nozzle has been installed. There are **build setups with strong jet noise** contribution and negligible high-lift wing noise[3]. This concerns settings with velocity ratio of $r_{U,OSL} \leq 0.2$. The limit for dominating jet noise depends highly on the installed models. For instance, P25H is an engine with a larger mixed jet area which results in higher jet noise and a slightly larger limit for build setups with strong jet noise, i.e. $r_{U,OSL} \leq 0.22$.

There are also **build setups with strong high-lift wing noise** contribution and negligible jet noise. This is the case for operational settings with velocity ratios of $r_{U,OSL} \geq 0.47$. Note, that in section E.0.2, an operation with $r_{U,OSL} = 0.47$ was called a bad isolated jet data point (reason: low SNR for background noise correction). Nevertheless, the data set for jet-flap interaction can be very well evaluated because the isolated jet noise component can be neglected against the high-lift wing noise.

A few methods come into mind when identifying the jet-flap interaction deltas (equation 4.2) for builds with strong high-lift wing noise and low jet noise:

- Evaluation with quasi-single source. The missing jet noise contribution causes an underestimation of the "energetic sum" (best guess) and an overestimation of the jet-flap interaction delta. However, it is possible to quantify the uncertainty and assign it to the calculated jet-flap interaction noise delta, e.g. $\Delta SPL_{JFI} = 2\,\mathrm{dB}^{\pm 0}_{-0.5}$.

[3]It is rather convenient, that high-lift wing noise can be neglected for low velocity ratios in JFI measurements. Low wind tunnel settings and thus low Reynolds numbers increase the risk of unrepresentative laminar-turbulent transitions (see section D.0.1)

- Accounting for both isolated sources, i.e. isolated jet noise and isolated high-lift noise, where the measured isolated jet noise has not been corrected against the background noise. The energetic sum will be slightly overestimated and the jet-flap interaction delta slightly underestimated. Yet, it is not possible to quantify the uncertainty.

- Accounting for both isolated sources, i.e. isolated jet noise and isolated high-lift noise, where the isolated jet noise spectrum is corrected for some frequencies with suitable SNR and interpolated for the other frequencies.

In between the quasi-single source regions there are **velocity ratios where both of the isolated noise sources are important**. In the aforementioned example, an equilibrium between the contribution of both isolated noise sources is reached at $r_{U,OSL} \approx 0.31$.

4.3. JFI measurement diagram

The gathered boundary conditions for background noise correction and quasi-single aircraft noise can be summarized w.r.t. velocity ratios where the measurements can be evaluated well.

Let us take for example the evaluation of wanted noise in a JFI experiment for the LIST nozzle (figure 4.4).

- Criteria for background noise correction of the isolated jet noise are defined and evaluated in appendix E. The corrections can be conducted for $r_{U,OSL} \leq 0.33$, yet corrections beyond 0.38 are not possible due to bad SNR.

- However, jet noise can be dimensionally neglected in JFI evaluations for $r_{U,OSL} \geq 0.47$.

- This leaves a processing quality gap between $r_{U,OSL} = 0.33 \ldots 0.47$ where a higher uncertainty in data quality must be expected. This means that it might be easier to trust the jet-flap interaction evaluation LIST Approach Operation with the higher velocity ratio ($r_{U,OSL} = 0.47$) rather than the lower velocity ratio of ($r_{U,OSL} = 0.39$).

The results for all the frequency ranges and both engines are displayed in figure 4.5:

- In general, it can be concluded, that data points with sufficiently high jet noise

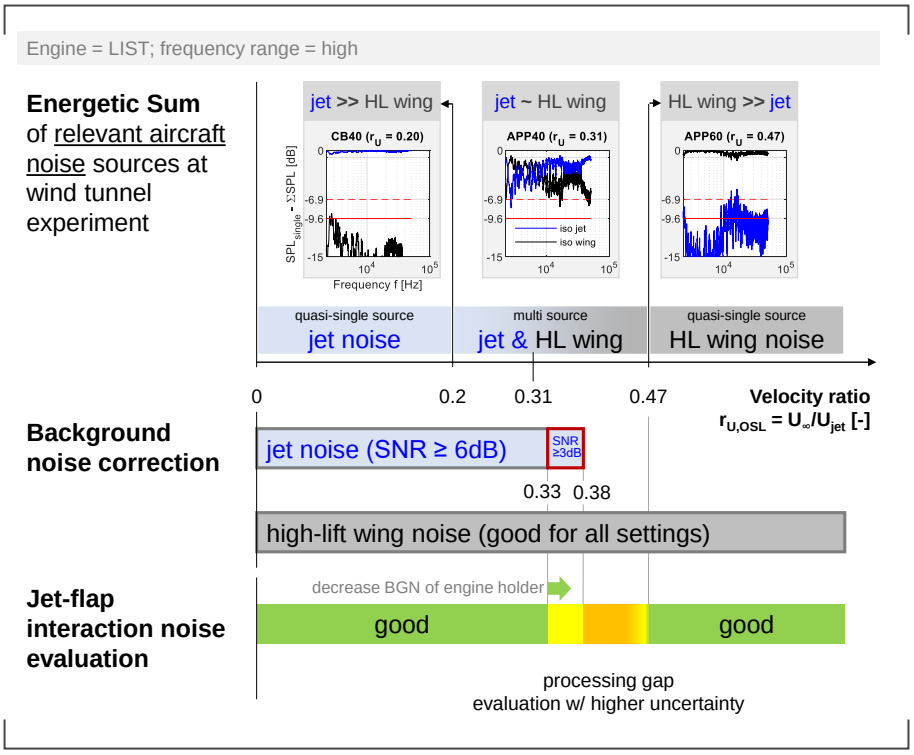

Figure 4.4.: **Summary: conditions for good data quality**

contribution are good to process. This includes data points where high-lift wing noise and isolated jet noise are similar.

- The processing gap occurs for the data points where high-lift wing noise becomes slightly more important than jet noise and the jet noise component cannot be neglected.

- A decrease in background noise sources (engine holder) may slightly diminish the region in which it is difficult to measure good quality data.

4.4. JFI measurement techniques

There are various possibilities to measure the jet-flap interaction delta. In general, the isolated jet, the high-lift wing as well as the installed engine to wing is measured. All of those three settings are checked against their respective background settings. All in all, the studying of one jet-flap interaction delta requires up to six data points (see figure 4.6).

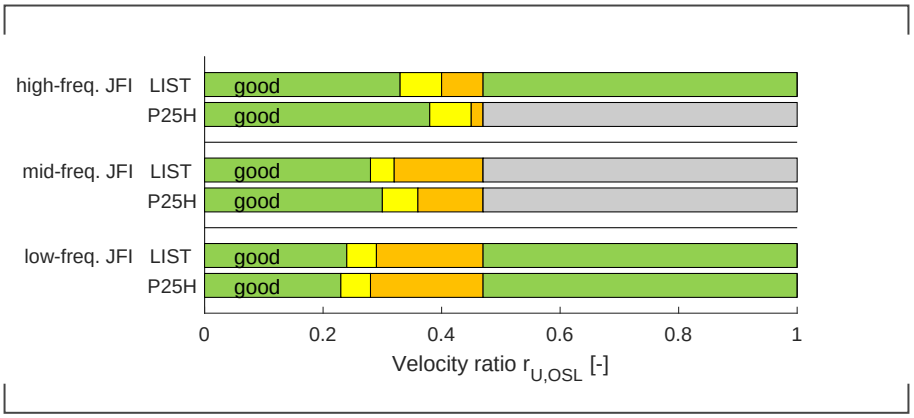

Figure 4.5.: **Good conditions depending on focus of evaluation**

The exact number of required builds and data points depends on the question whether the wing is actually important (quasi-single problems, e.g. all static jet operational settings), whether the wing must be measured as isolated wing (general option and best option for high lift wings w/o slat) or whether the integrated wing option is good (e.g. for high-lift wings with a slat and evaluation on full scale relevant frequency range).

There are more options (12 instead of 3) which depend on the decision whether side plates are part of the isolated jet measurement. The interested reader is referred to appendix G. For an introduction it is crucial to know that there are three general options:

- The general JFI noise test needs at least four build setups (with the more detailed options in appendix G, it is five build setups).
- A JFI noise test focused on operational settings with quasi-single jet noise requires merely 2 builds. It is valid for all types of wings, but requires knowledge of the quasi-single source limit (e.g. $r_{U,OSL} \leq 0.2$ from a pre-test).
- If a wing is measured where high-lift wing noise is sufficiently greater than the noise of the engine holder (e.g. because of slat noise), it can be measured as an integrated wing setting. Only two builds are required.

Two of those examples are to be extracted here: a full build (5 data points / 4 builds) as well as a time-efficient build (4 data points / 2 builds). Those figures summarize how each of the wanted noise group must be corrected against its background noise.

In the 5/4 build settings (figure 4.7), the full build is corrected against the setting

		SIGNAL **int. / iso. HL wing**		SIGNAL **iso. engine**		SIGNAL **full build**		empty wind tunnel	side plate + wt pipe + wing	side plate + wt pipe	side plate	side plate + wing			
		BGN HL wing		BGN engine		BGN w / w/o side plate									
Application	**wing**	**HL w.**		**eng.**		**JFI**		0	1	2	3	4	**dpts**	**builds**	**evaluation**
should work for all JFI-problems	no high-lift wing			2	-	1	-		X	X			2	2	static jet or JFI w/ quasi-single jet noise
	isolated high-lift wing	4	3	2	2	1	2		X	X	X	X	5	4	general JFI use
only high-lift wing w/slat & mid/high freq. range	engine integrated onto high-lift wing	1	2	2	2		2		X	X			4	2	optimal in time+cost

Figure 4.6.: **Minimal number of test builds for jet-flap interaction noise experiments, depending on model type.**

where the wing is removed, but the side plates are installed. This setting is also used for the isolated engine signal and background noise measurement. In this case the side plates have not been removed in order to resemble some of the aerodynamic and acoustic full build conditions. The removal of the side plate for isolated jet measurement is possible, but requires additional data points. The high-lift wing noise is measured with an isolated wing and the corresponding background setting is an empty wind tunnel where the side plates are installed.

A more time and cost efficient measurement can be done by using the 4/2 build setting (figure 4.8) where the wing setting has been changed to an integrated wing. This reduces the number of required builds to two. Note that only one background noise data point is needed for all of the three measured signals.

It is of course possible to apply different evaluation methods dependent on the test rig. For reason of processing, it would be best to stick to one concept that fits all. However, there is always a difference in the JFI evaluation chain between static jet operation and flight jet operation.

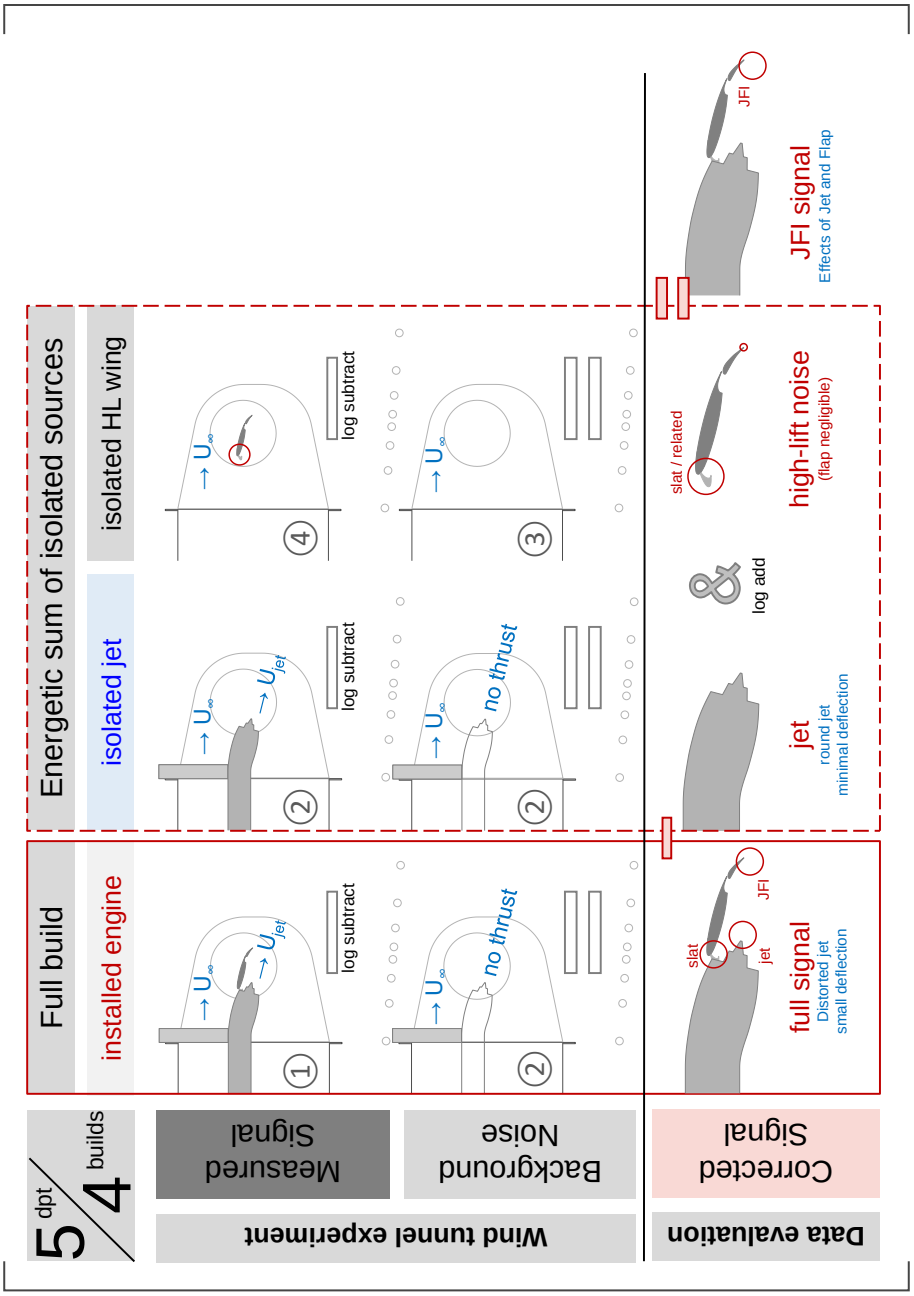

Figure 4.7.: **5/4 JFI noise measurement (i.e. 5 data points/4 builds)**

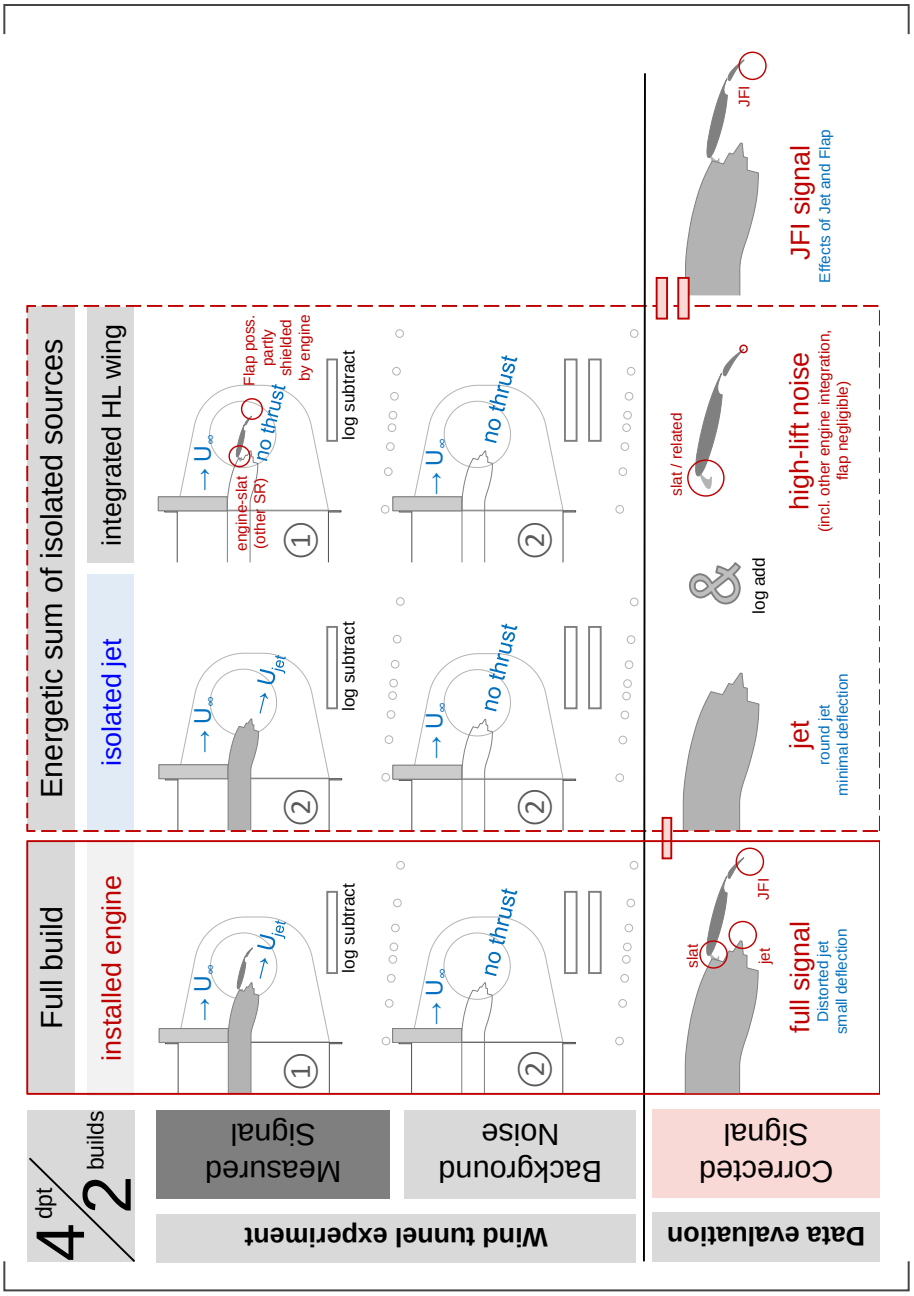

Figure 4.8.: **4/2 JFI noise measurement (i.e. 4 data points/2 builds)**

5. The influence of the high-lift wing aerodynamics

An understanding of underlying steady aerodynamics of the installed vs. isolated build is mandatory for the physical characterization and JFI noise prediction. The static pressure field underneath the wing influences the installed jet properties (see section 5.1). Two sets of jet-flap interaction are studied where the flap trailing edge position is constant. The main wing changes in position due to different flap deflection angles. Hence, secondary effects due to the positioning of the main wing and the flap deflection angle can be evaluated (see section 5.2).

5.1. Flow physics at the wing pressure side

One of the aerodynamic questions is how the jet is deflected due to the presence of the wing. This depends on wind tunnel speed:

1. At no or very low wind tunnel speed, the flow can be approximated as a subsonic 3/4 open channel flow which is initially not attached to the wall. The 1/4 wall is the pressure side (concave side) of the wing and finite in length. If the pressure side is positioned close to and approximately parallel to the jet, the Coanda-effect occurs: An isolated jet entrains air axisymmetrically which results in the symmetric low pressure region around the jet. The presence of the wall on one side causes an imbalance of the installed jet w.r.t. the engine axis: Since entrainment on the wall side is restricted (scarce amount of air particles), the jet deflects towards the wall and may even attach.

2. At mid and high wind tunnel speed, high-lift aerodynamics become prevalent: The "finite side wall" finally acts like an airfoil, i.e. there is flow circulation which induces a static pressure field around the wing. This results in a vertical velocity component downstream the wing (downwash). Likewise it induces a vertical upwash upstream the wing. The downwash helps to deflect the jet

away from the wing. Moreover, the higher static pressure on the wing pressure side changes the position where the jet is fully discharged.

5.1.1. Secondary flow analysis

The deformation of the jet can be studied by analysing the flow properties normal to the engine axis, especially just downstream the flap trailing edge.

One of the most important features of the flow distribution is the outer shear layer (OSL). In the secondary flow field the stream traces can be drawn using the velocities V and W. The stream traces of the shear layer are bend whereas the stream traces of the potential field are rather straight (compare figure **??**). The resulting flow between flap downwash and jet shear layer depends on the state of the equilibrium between vertical flow components in the shear layer compared to the downwash. The build height can impact the top part of the shear layer by no interaction, compression, damaging etc.
An undamaged shear layer redistributes the vertical downwash flow to the sides, as long as some vertical components of the shear layer are larger than the downwash. Otherwise, the downwash induces a *natural turn*.

The following secondary flow images were measured during the LIST test campaign using a five hole pressure rake (see figure 5.1). The jet properties are evaluated by using a so-called divergent color scheme (blue-yellow-red), whereby jet features were characterized by a selection of critical velocities (equation 5.1).

$$\text{sort}\left(U_{\infty}{}^{+1\,\text{m/s}}_{-1\,\text{m/s}}, U_{c}{}^{+2\,\text{m/s}}_{-2\,\text{m/s}}, U_{Core}{}^{+2\,\text{m/s}}_{-2\,\text{m/s}}, U_{Byp}{}^{+1\,\text{m/s}}_{-1\,\text{m/s}}\right) \text{ \& omit min value/max value} \tag{5.1}$$

The resulting color scheme contains five distinctive colors (dark blue, light blue, yellow, orange, red). Those colors resemble different flow regions of the jet, whereby the outer shear layer (OSL) and the bypass potential core are especially relevant (in the jet plots of figure 5.1):

- For normal dual stream jets, i.e. $U_{Byp} < U_{Core}$ (case 3 in figure 5.1), the OSL outer part is light blue and the OSL inner part is yellow, the bypass potential core is orange.

normal		U_∞	<	U_c	<	U_{Byp}	<	U_{Core}	
——-	Flight	OSL outer		OSL inner		Bypass		Core	
inverted		U_∞	<	U_c	<	U_{Byp}	>	U_{Core}	

- For inverted dual stream jets, i.e. $U_{Byp} > U_{Core}$ (cases 1,2 and 4 in figure 5.1), the bypass potential core is dark red. The OSL inner part can be identified by the combination of yellow and orange.

The results of the campaign can be clustered by wind tunnel velocity as well as installation height (figure 5.1):

1. For low wind tunnel velocities and sufficient space, the outer shear layer is hardly damaged and redirects the vertical flow very close to the wing. This setting coincides with large additional noise. The jet potential core top part is greater affected than its bottom part. Downstream the flap, the installed and isolated jet mixed diameter match very well. This means that there is no bend on the jet bottom part. However, the geometric center of the jet does not align with the engine axis (turning angle of $\varphi = 0.5\,^{\circ}$). In other words, the turn is caused by balance redistribution which is why the type of flow turning is defined in this dissertation as a *virtual turn*.

2. For low wind tunnel velocities and restricted space, the redistribution of potential core flow to the sides increases. The jet top part is straightened out and looks rectangular. The shear layer top part is decimated due to space restrictions forced by the flap (*forced turn*). The small downwash is most effective at the very center of the jet top part (Z+). At this position, the jet potential core opens like the wings of a butterfly downstream the flap. The turn of the jet bottom part is visible but rather small in dimension compared to the turn of the geometric center of the jet.

3. For higher wind tunnel velocities and sufficient space, there is a state where the outer shear layer is in equilibrium with the vertical downwash. Two symmetrically aligned vortices deflect the downwash flow components to the sides. The bottom part of the jet and shear layer remains undamaged. Yet, the entire jet does also turn by some angle. If the downwash is larger than opposing components in the OSL, the jet underneath the flap will naturally turn.

4. For high wind tunnel velocities and restricted space, the outer shear layer cannot equalize the downwash very well. The natural turning is very strong and the mechanisms for flow redistribution seem to be weaker. The least amount of vertical flow redistribution components in the shear layer is located at the top jet center (Z+) position. There, the potential core gets penetrated hardest which forces the flow to a kidney shape downstream the flap (figure 5.1, [4]), comparable to case 2.

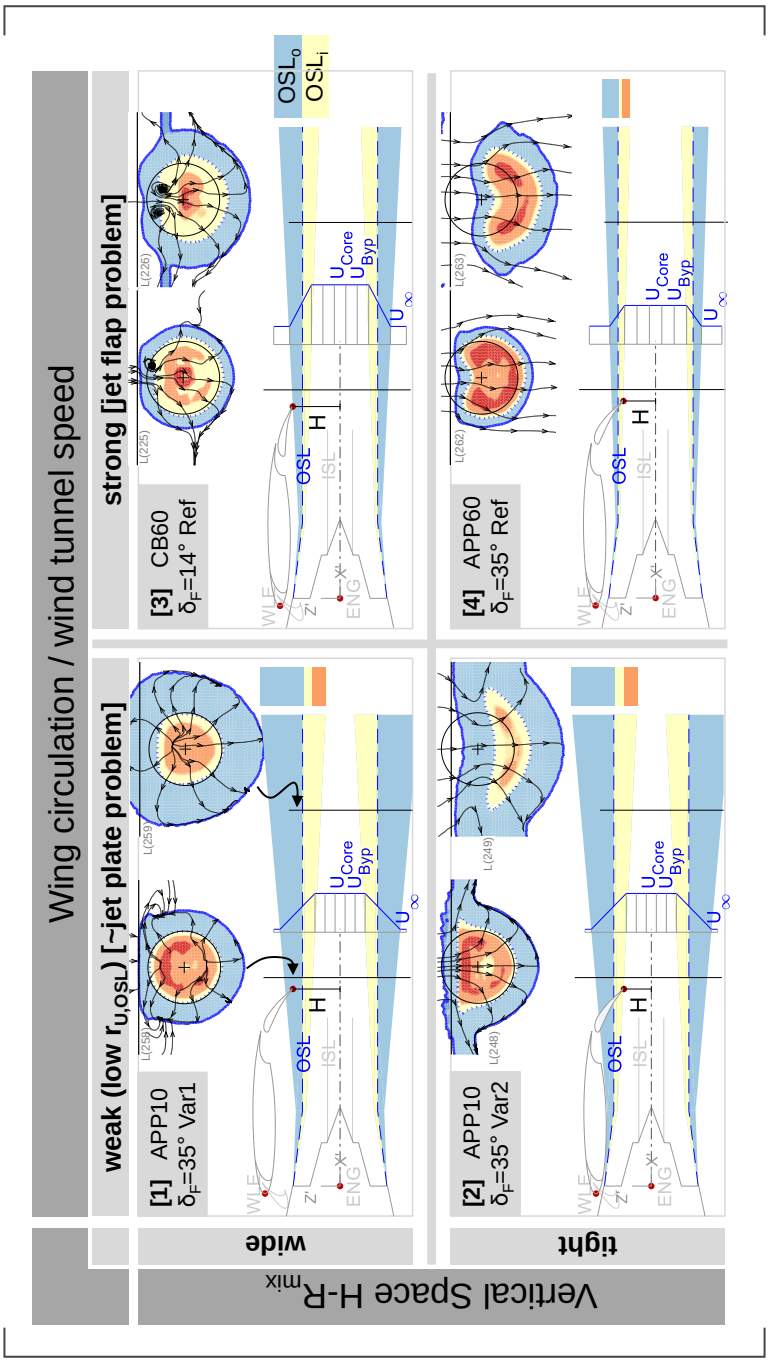

Figure 5.1.: **Jet-flap interaction depending on wing circulation and installation height**

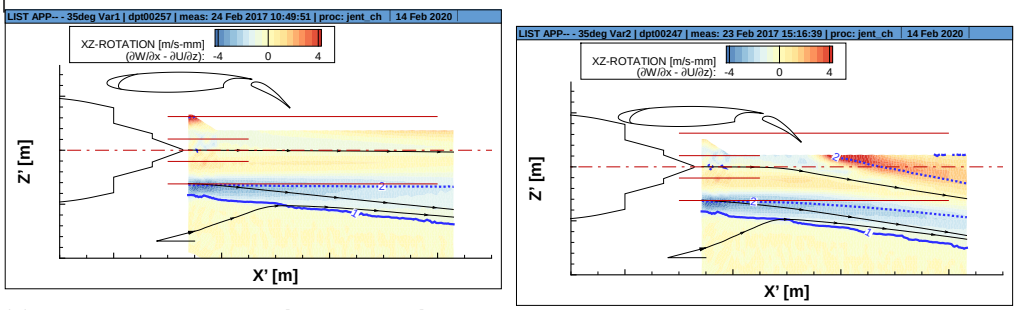

(a) $H/D_{mix} = 0.63$: **no (or: virtual) bending**

(b) $H/D_{mix} = 0.36$: **forced turning**

Figure 5.2.: **Jet bending for static jets. The blue solid line (1) shows a streamwise velocity criterion for the OSL and the blue dotted line (2) the velocity criterion for the mixed jet diameter.**

5.1.2. Turning angles

The aerodynamic data gathered in the measurement campaigns suggests that the turn of the flow occurs approximately below the flap leading edge streamwise position and is finished near the flap trailing edge streamwise position (at least for $r_{U,OSL} \rightarrow 0$). See figure 5.2b, where the mixed jet diameter of an isolated jet is specified in red (with help of the U_c velocity criterion) and the jet shear layer is visible because of the flow rotation in the XZ-plane. This example shows also that even for static operations (wind tunnel off) jet turning can be forced.

Strong jet bending can potentially cause a noise mechanism on its own. This could be shown during a DLR campaign on a Coanda flap with active flow control [38]. However, high values for turning angles on their own are not a safe indicator for jet bending noise: While the flap-induced forced turn (case 2 in figure 5.1, $H/D_{mix} < 0.5$ and $r_{U,OSL} < 0.3$) causes large additional noise and could potentially feature jet bending noise, the downwash-induced natural turns ($r_{U,OSL} > 0.3$) cause very low or no additional noise.

Aerodynamic data of the flow field is used to quantify the bending angles: There are three planes normal to the engine axis, which are located at one nozzle diameter downstream the engine (1D), shortly behind the flap trailing edge (FTE) as well as at four engine diameters downstream the engine (4D). Some results at x=FTE and x=4D are displayed in figure 5.1 and 5.3. The turning angles are evaluated by calculating the geometric center of the jet contour[1] (see results in figure 5.4).

[1] Note that there is room for improvement regarding the mechanism of calculating the real, e.g. mass-flow-weighted or momentum-weighted center of the jet.

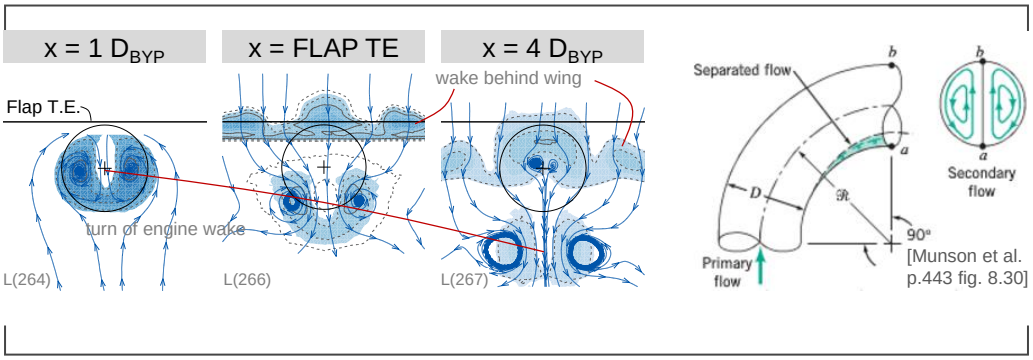

Figure 5.3.: **Turning of flow below high-lift wing (engine-off operation) vs. turning of internal flow [36]. Light blue shades indicate wake flow with help of a velocity criterion. The streamlines consist of Y- and Z-velocity and visualize normal flow features.**

The strongest bend measured occurs at the low noise engine-off condition (see figure 5.3), where the wing is at reference position and the flap at a deflection angle of $\delta_F = 35\,°$. As there is no jet issued from the engine, a different method than the center of the geometric contour was used: The wake behind the engine can be tracked using the center point of the vortex-like feature in the secondary flow field. Streamlines are plotted using y-velocity and z-velocity and they show two approximately symmetrical vortices at the wake position. The secondary flow field contains some similarities to the secondary flow of an internal flow turning (here: $90\,°$ bend, image extracted from [36]). The largest evaluated flow turning angle is $\varphi = 14\,°$.

This result is also depicted in figure 5.4, which summarizes all main results of the aerodynamic study: In most settings, flow reshaping and turning must be expected. The build height H is an essential parameter for the start of the bending. At the right equilibrium of jet velocity, wind tunnel speed and build height, there is a balance between the vertical flow of the downwash behind the flap and vertical velocity components of the outer shear layer (case 3 in figure 5.1). Consequently, two symmetrical vortices are induced at the edge of the shear flow. This stretches the jet in Y-direction. At a certain velocity ratio (somewhere in between $0.3 \leq r_{U,OSL} < 0.47$), this equilibrium between shear layer and downwash cannot be matched anymore and the jet starts to bend more.

5.1.3. Streamwise flow properties near the flap trailing edge

There are other interesting effects which can complicate the modelling of the effect. All in all, they are of minor importance. These effects are shown with the help of

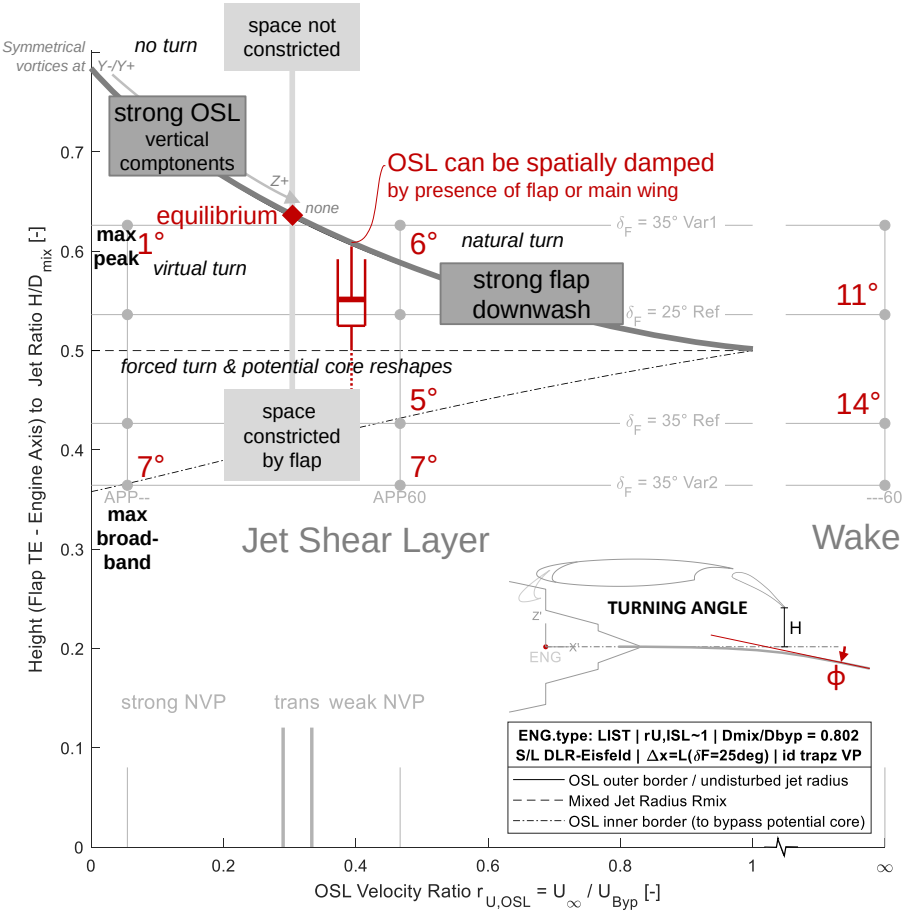

Figure 5.4.: **Jet-flap interaction diagram, including aerodynamic features**

mean flow data from a CFD simulation by Dirk Boenke [5]. Additional figures are listed in appendix J.

The circulation around the wing results in a high pressure region below the wing with corresponding low local velocities. Consider that the spatial influence of the wing's static pressure field is large (approximately full AWB wind tunnel height when combining suction side and pressure side, see figure J.2a) and that it does influence the jet underneath the wing (figure J.2b).

This shows two things. First of all, the wing influences the static pressures of the jet's near-field and delays the jet expansion under the wing to being fully discharged. Furthermore, the wing static pressure field is not causes the installed jet to be truly axis-symmetric. Second, the velocities on the wing pressure side are also below the target flight velocity. This means that characteristic velocity criteria from the installed jet may slightly differ compared to the isolated jet. This could theoretically complicate the modelling of jet-flap interaction effects. The details can be seen in figure 5.5 where the velocities are resolved around the Bypass velocity:

- A. The shear layer centerline velocity (see equation 3.3) is used as a criterion to identify the mixed jet diameter (white line). The mixed jet diameter is almost constant except in the initial flow region where the jet real expansion effect can be observed. In streamwise direction, the jet potential core reduces constantly.

- B. An exception is the area underneath the wing. There, the jet velocity is significantly lower than downstream the wing. In fact, there is an acceleration of the bypass jet flow towards the flap trailing edge.

- C. The cause for low velocities underneath the wing is the higher static pressure caused by the wing. Four deliberately chosen pressure levels are displayed. The pressure lines are almost vertical to the jet top part (near the trailing edge). At the jet bottom part, some pressure lines point in streamwise position. Hence, the wing high pressure region causes asymmetry within the jet near the flap trailing edge.

- D. This asymmetry may influence the jet even downstream the wing, e.g. in terms of different jet potential core lengths around the circumference of the jet. Moreover, it could be an enabler for the flow to bend.

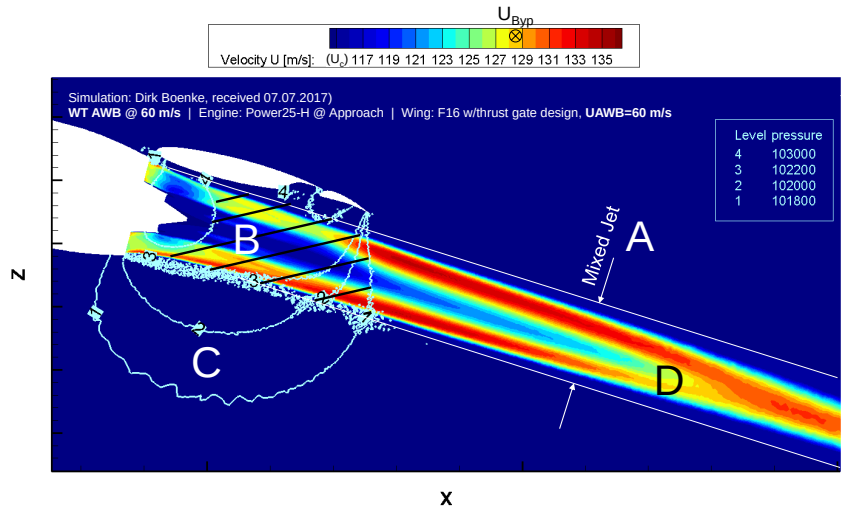

Figure 5.5.: **Flow acceleration at F16 flap pressure side**

5.1.4. Static pressures on flap pressure side

The following figures show static pressure on the pressure side of the flap for the three ports 11, 12 and 13 (see figure 5.7). The static pressure are depicted as difference pressures w.r.t. port 1 (flap trailing edge). The y-axis is reversed in order to help indicate flow deceleration (decreasing trendline) or flow acceleration (increasing trendline). The x-axis displays wind tunnel speeds in meters per second, the left column shows engine-off operations, the right column a same speed jet engine operation at $160\,\mathrm{m/s}$. The following conclusions on installed builds can be drawn from figure 5.6:

1. For settings with no jet flow, the static pressure maximum is located closer to the leading edge and the pressure reduces in streamwise direction towards the flap trailing edge. The static pressures on the flap pressure side (left diagrams in figure 5.6) are comparable in magnitude - independent on engine integration height. The only difference can be explained with the influence of the jet wake behind the engine nozzle.

2. Depending on the wind tunnel speed, the static pressure in the vicinity of the flap (pressure port 13) increases. This is also true for some settings where the engine is running. The flap trailing edge must be positioned out of jet flow.

3. For some jet operations with no or low wind tunnel speed, the static pressures increase due to the close proximity between the jet and the wing. Contrary to the typically decreasing pressures in streamwise direction (1, there is an increase (potential flow deceleration) before the flow accelerates across the flap trailing edge. This atypical pattern coincides with large jet-flap interaction deltas.

4. For radical integration heights $H/D_{mix} < 0.5$, some of the described characteristics change. For low wind tunnel speed, high static pressures are recorded. They are so large that a new y-scale (blue) is introduced. The high static pressures may correlate to high accelerations along the flap. Contrary to the out-of-jet flow positioned flap, the static pressures near the flap decrease with increasing wind tunnel speed. The pressure peaks on the pressure side of the flap are rather close to the flap trailing edge, thereby causing potentially high accelerations across the flap trailing edge.

5. For some installed builds where flap space requirements and isolated outer shear layer space requirements mismatch, the pressure peak on the flap pressure side moves slightly to the flap leading edge again, i.e. it resembles more the "normal" characteristics of to isolated wing. It must be further investigated whether this is or is not a criterion for jet flow which is attached to the flap. However, those settings show an interesting effect:

6. In general, flows along steep curved geometry (here: the $\delta_F = 35\,^\circ$ flap, see figure 5.7) represent wing settings which can produce very high lift. This also means that the static pressures are higher than the ones at the flaps which are more favorably aligned with the flow (here: the $\delta_F = 25\,^\circ$ flap). Yet, data points which underlie the effect mentioned in conclusion 5, can show the opposite behavior.

5.2. Acoustical study of different flaps which are installed at the same height

In this section, the difference in noise is to be examined when the main wing is installed at different heights, but the flap trailing edge remains at the same height (see figure 5.8). The different main wing height has been achieved by using two different flap deflection angles, $\delta_F = 25\,^\circ$ and $\delta_F = 35\,^\circ$ at their reference settings. On the one side, the jet under the main wing with $\delta_F = 25\,^\circ$ encounters higher static pressures which are induced by the main wing pressure side. Therefore, immediately

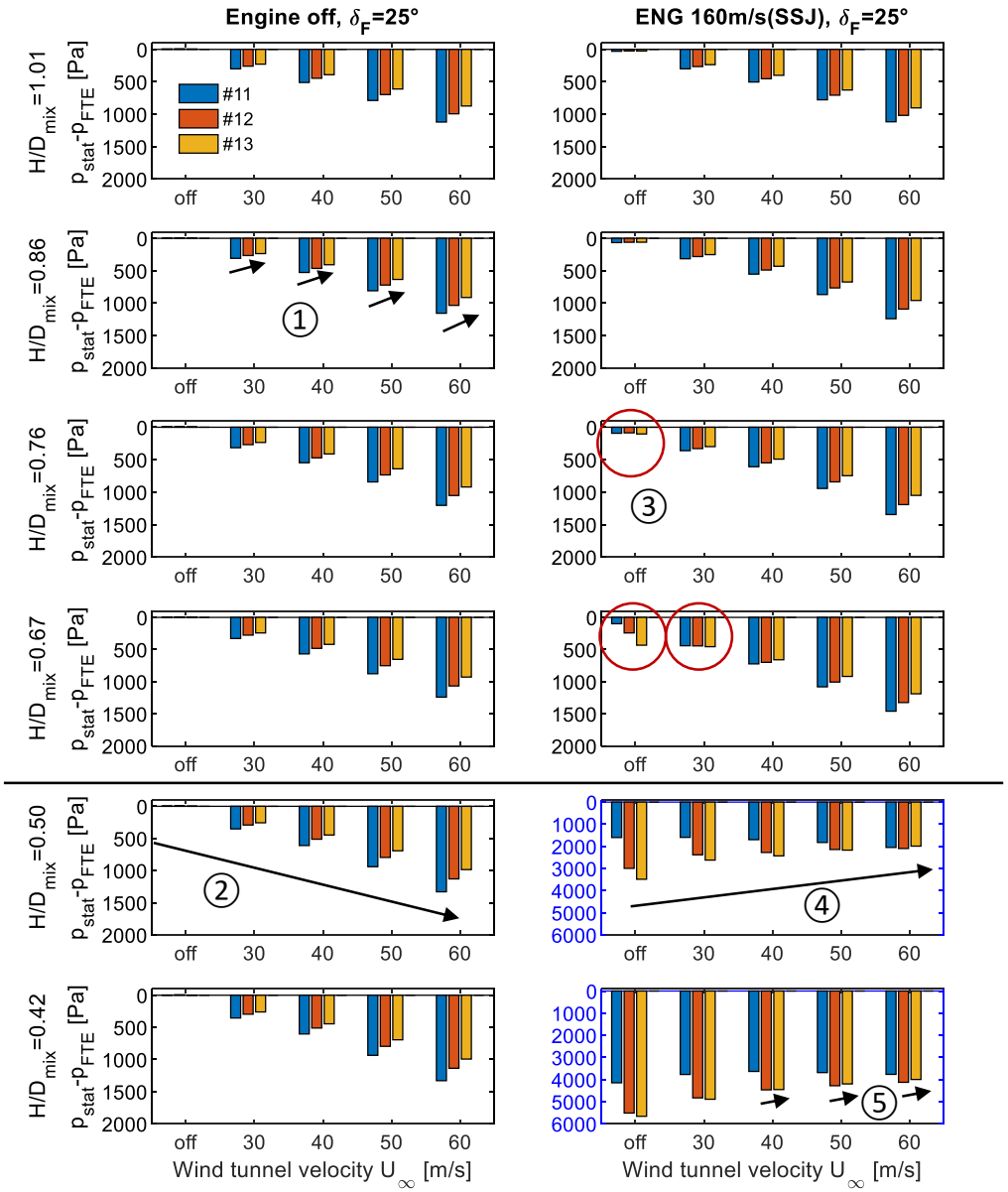

Figure 5.6.: **Static pressure distribution on flap pressure side depending on build height and operational setting**

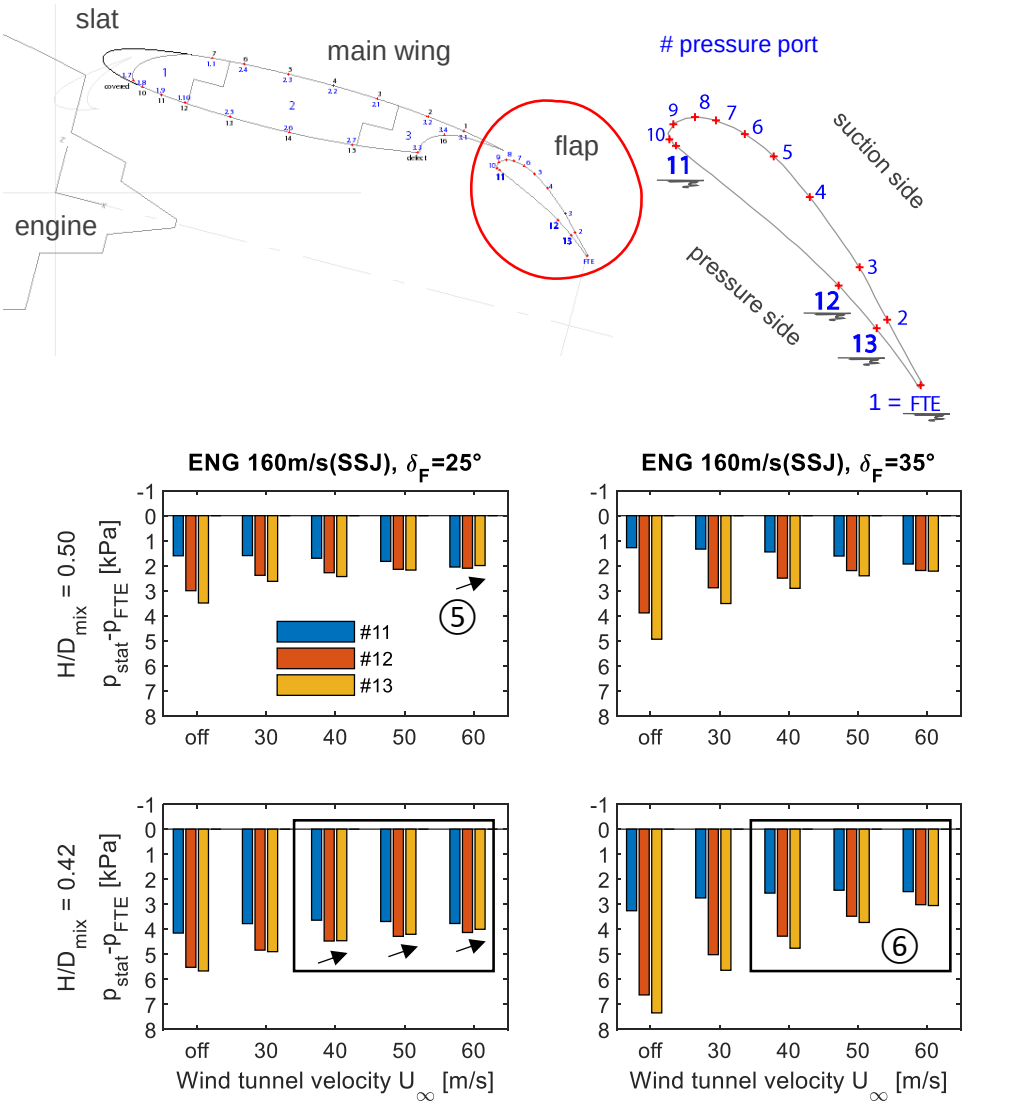

Figure 5.7.: **Static pressure ports and distribution on flap pressure side depending on build height and flap angle**

below the wing, there may be greater local flow acceleration and deceleration as well as greater flaws in the symmetry of the jet shear layer. On the other side, the acceleration into the free field under the flap trailing edge should be smaller than at the $\delta_F = 35\,^\circ$ build setting.

In fact, the greater distance with the steeper flap deflection angle ($\delta_F = 35\,^\circ$, red spectra in figure 5.8) provides an additional jet-flap interaction noise of $\Delta SPL_{JFI,35deg} - \Delta SPL_{JFI,25deg} = 0.5 \ldots 1\,\mathrm{dB}$ when comparing it to the $\delta_F = 25\,^\circ$ setting.

How can this result be interpreted w.r.t. the influence of the wing? The sound pressure levels are higher for the main wing which is farther away. This does not necessarily mean that closeness of the main wing is the reason behind the decreased noise. The noise benefit of the main wing with the $\delta_F = 25\,^\circ$ flap is likely to be caused at the flap. The curvature of the wing allows a smoother interaction angle between shear layer and flap. The static pressures near the wing are smaller compared to the steeper angle. Thus, the acceleration of any vortices in the shear layer near the flap should be slightly smaller for the $\delta_F = 25\,^\circ$ flap. Depending on the setting, flow attachment can be involved.

It can be argued that the main wing is not directly relevant in the chosen setting and that the main effect is caused by the flap. The main wing influences high-lift aerodynamics and forms a reflective surface of finite length. But, the build height H may be the single most important contributor to a JFI-problem with same length L and operational settings. In the above problem, this factor was eliminated by comparing two builds with the same flap trailing edge heights. As concluded, not the main wing height, but rather the flap deflection angle (and the resulting pressure field near the flap) is the driver of this problem.

In order to defend the above experiment: It is rather difficult to design an academic build where the effect of the main wing can be isolated since the flap is always involved. One approach could be the comparison of a normal engine integration compared to a radical engine integration (for the same flap trailing edge height). The normal integration requires a steeper angle than the radical integration in order to get the same flap trailing edge height. Then, it can be compared whether a radical integration of the wing outweighs the noise benefits of the less steep flap deflection angle.

One setting which is a first example of such a comparison is shown in figure 5.8 (left). The radical build is not the most extreme. However, it is the only one which was measured and is comparable. Normal engine integration does not encounter any (theoretically) predicted interaction with the main wing whereas in the radical setting, the shear layer may locally attach to the main wing.

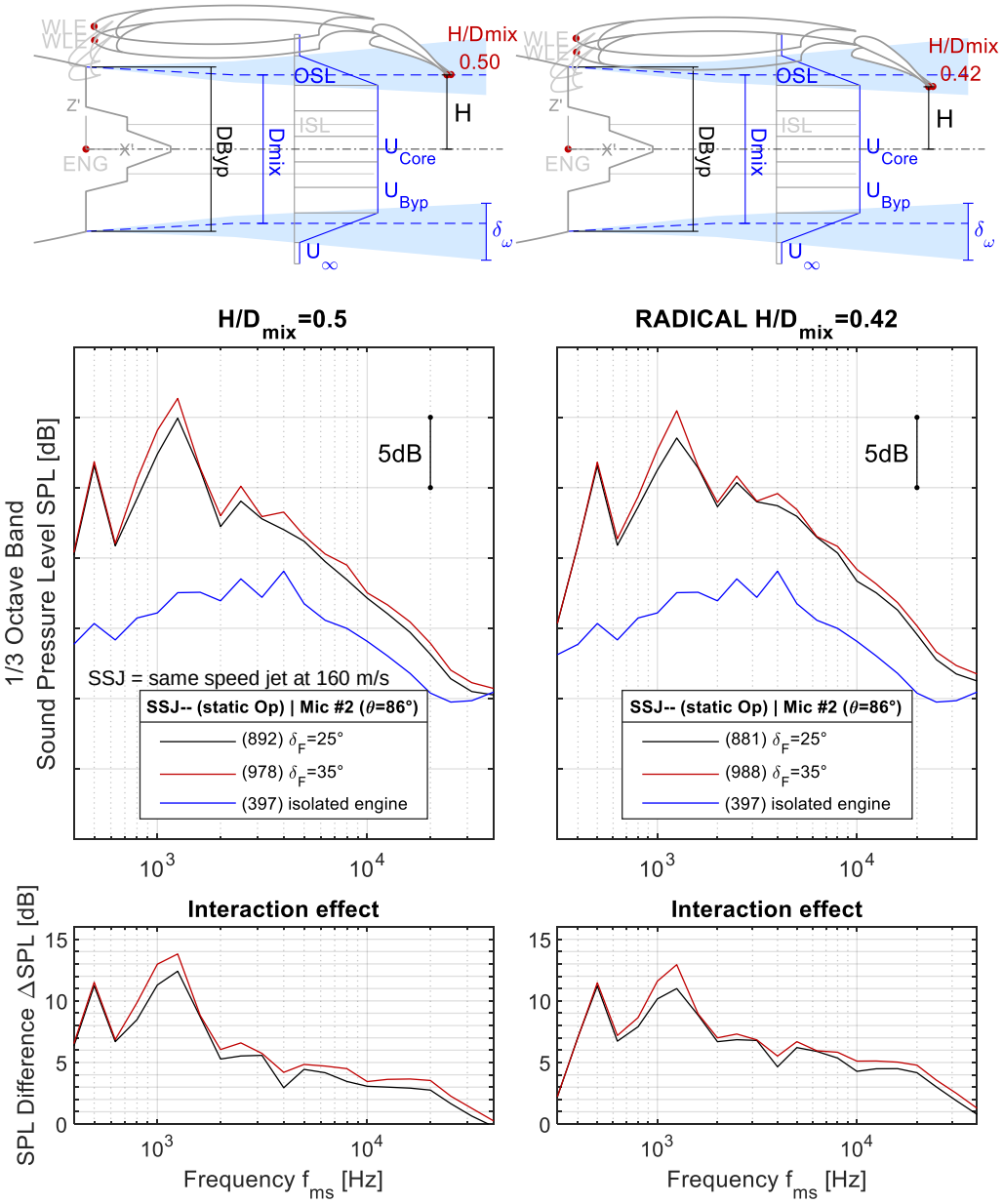

Figure 5.8.: **Engine interaction with same flap trailing edge heights**

It turns out that the additional noise ($\Delta SPL_{JFI,35deg} - \Delta SPL_{JFI,25deg} = 0.5 \ldots 1$ dB) is very similar for both build heights (compare figure 5.8, right). Since the additional noise is comparable, it is likely that those secondary noise mechanisms have not changed. This means that the steep flap deflection angle is still more relevant to the problem than the main wing.

Further research, possibly with a more radical engine integration could possibly show an acoustical influence caused by the main wing. Nevertheless, it is also possible to draw a definition line here and to declare a new physical problem called "partially buried jet exhausts" which needs to be studied independently of the jet-flap interaction effect first.

5.3. Summary

In this chapter, evidence was presented that the presence of the jet close to the flap leads to static pressure profiles on the flap which cause a much greater acceleration on the trailing edge than without the jet. This mechanism is a much better explanation for JFI-Noise than the flow turning underneath the wing. Flow turning occurs at no thrust flight operations $r_U \to \infty$ where the JFI effect is negligible. The great jet-flap interaction deltas are observed for jet reshaping under static operations. The reshaping has been analysed using secondary flow analysis.

Out of the high-lift elements (slat, main wing, flap), the main wing is acoustically speaking a reflective surface and otherwise a lesser acoustic JFI contributor[2] than the flap deflection angle. Smaller deflection angles are more beneficial to noise reduction than larger deflection angles.

All in all, it can be concluded that the direct noise generation by the main wing is negligible compared to the mechanisms at the flap. The main wing height H_{Wing} can be neglected in an analytical jet-flap interaction noise model against the flap height H and even against secondary flap parameters (here: flap deflection angle). Nevertheless, it is still a good idea to check whether the main wing plays a greater role than planned (possible jet flow attachment, collision with holders etc.). For example, the transfer of any insights from this work to partly buried engine exhausts may require such a check.

[2] A possible exception is the case of otherwise unwanted jet attachment to the main wing surface. It could be studied whether the main wing pressure side contributes to low noise by preconditioning the jet before hitting the flap.

6. The influence of different build parameters to JFI

The evaluation of jet-flap interaction parameters depends on the parameter type (compare figure 6.1). There are build parameters (e.g. engine integration parameters and flap settings) as well as operational parameters (e.g. the flow streams).
It is very handy to separate build parameters into parameters which directly characterize the outer shear layer (primary build parameters, see section 6.1) versus other (secondary) build parameters. Secondary build parameters are the typical aircraft definition parameters. They can be analysed with elemental motion analysis (section 6.2) as well as sensitivity studies.

The operational parameters can be either split by flow stream or outer shear layer properties. The flow stream property study can be used for certain combinations of jet and wind tunnel velocities, e.g. certification velocities. These operational parameters were used in the prior sections. From an academic point of view, the use of shear layer properties allows for more systematic physical conclusions. Similar shear layer geometries can be achieved by using the same velocity ratio $r_{U,OSL}$. A shear layer property study has been conducted in section 6.4.

6.1. Build analysis of primary parameters

The primary parameters have been defined before as length L, virtual shear layer origin $x0$, height H and mixing radius R_{mix} which describe the conical geometry of an isolated jet shear layer at the flap trailing edge position.

Change of height All the previous comparisons have been made for constant jet mixing radius R_{mix} and length L. Therefore, the most sensitive primary build parameters (see figure 6.2) in such a setting is the JFI height H. Hence, the height ratio has been assigned to the y-axis of the jet-flap diagram. The following study is a height variation study (see figure 6.3). The wing flap parameters are constant

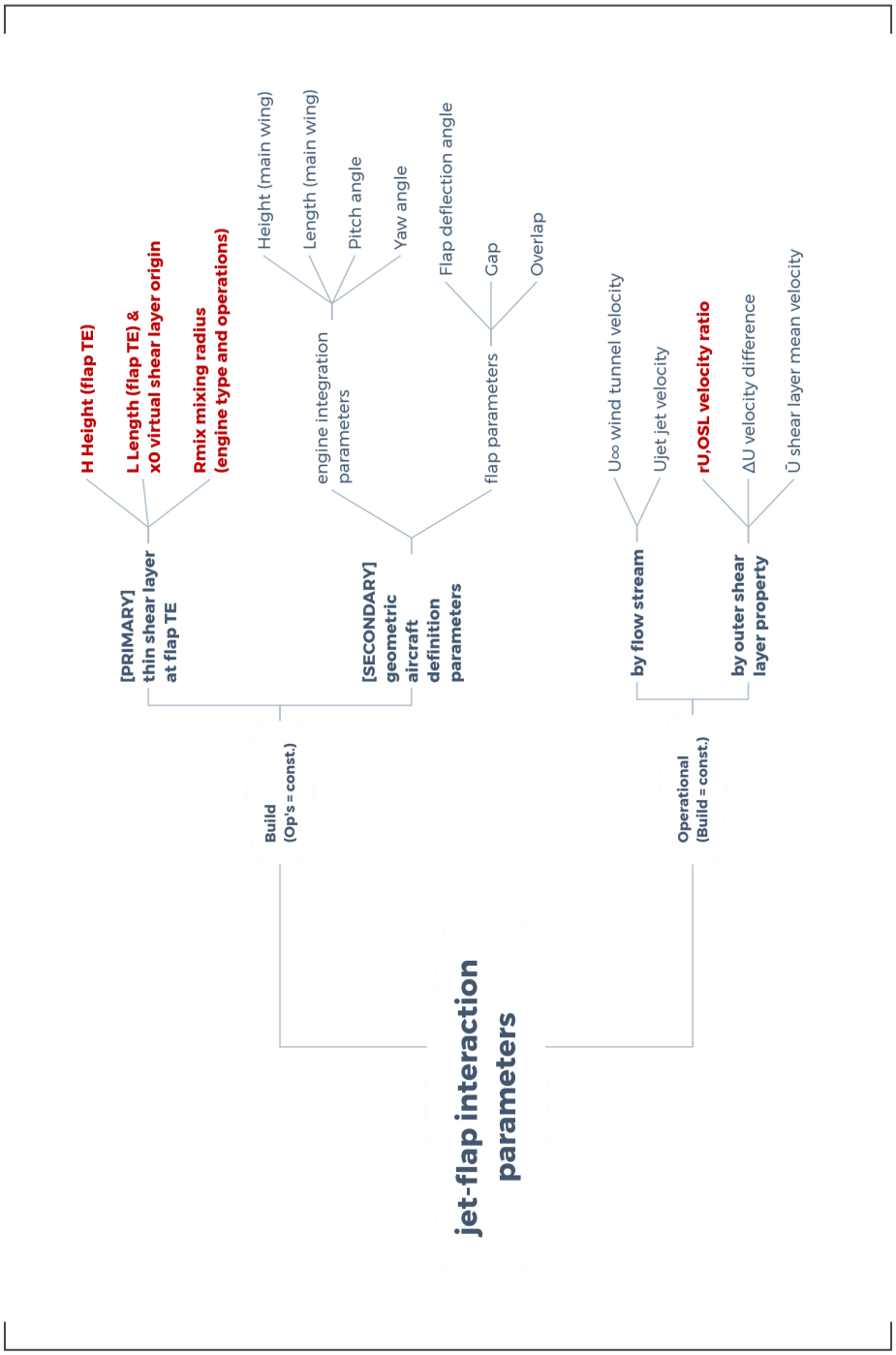

Figure 6.1.: **JFI Parameters**

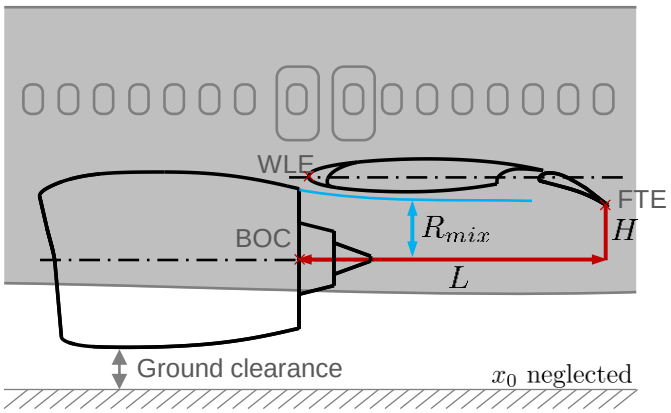

Figure 6.2.: **Engine integration (primary build parameters)**

($\delta_F = 25\,^\circ$ setting) whereby $\theta \approx 90\,^\circ$ (mic 2) is observed. The engine setting is the same for all data points (APCB), but the wind tunnel velocity changes between off, 50 m/s and 60 m/s. Installed noise (column 1) and energetic noise (column 2) are depicted as OASPL relative to a common maximum value. The JFI effect is shown in column 3 for all of the relevant JFI frequency ranges. The following conclusions can be drawn:

- The energetic sum (second column) is constant for the same velocity ratio because of the special situation in which the jet speed is constant and the wind tunnel speed changes. Since the jet speed remains the same, the isolated jet noise is constant for each velocity ratio. However, the wing-related noise has been measured for different integrated wing settings. If this wing-related noise changes for a constant velocity ratio, then this may be an indicator of engine integration noise other than jet-flap interaction noise. As this is not the case, the additional noise should stem from jet-flap interaction.

- The greatest effect of jet-flap interaction noise occurs within the mid frequency range where a maximum JFI delta of 16 dB was measured. Note, that this maximum occurs for a quasi-static jet at $H/D_{mix} = 0.54$. It is larger than the OASPL-value for $H/D_{mix} \approx 0.47$ which is closer to the jet mixing radius. Even though the number of test points is rather low, it can be assumed that the second peak OASPL maximum might occur at/or slightly below the calculated isolated jet width at static operations.

- The jet-flap interaction OASPL delta for the high frequency range is especially high for static jet conditions at low height. It can cause a JFI delta of up to 6 dB.

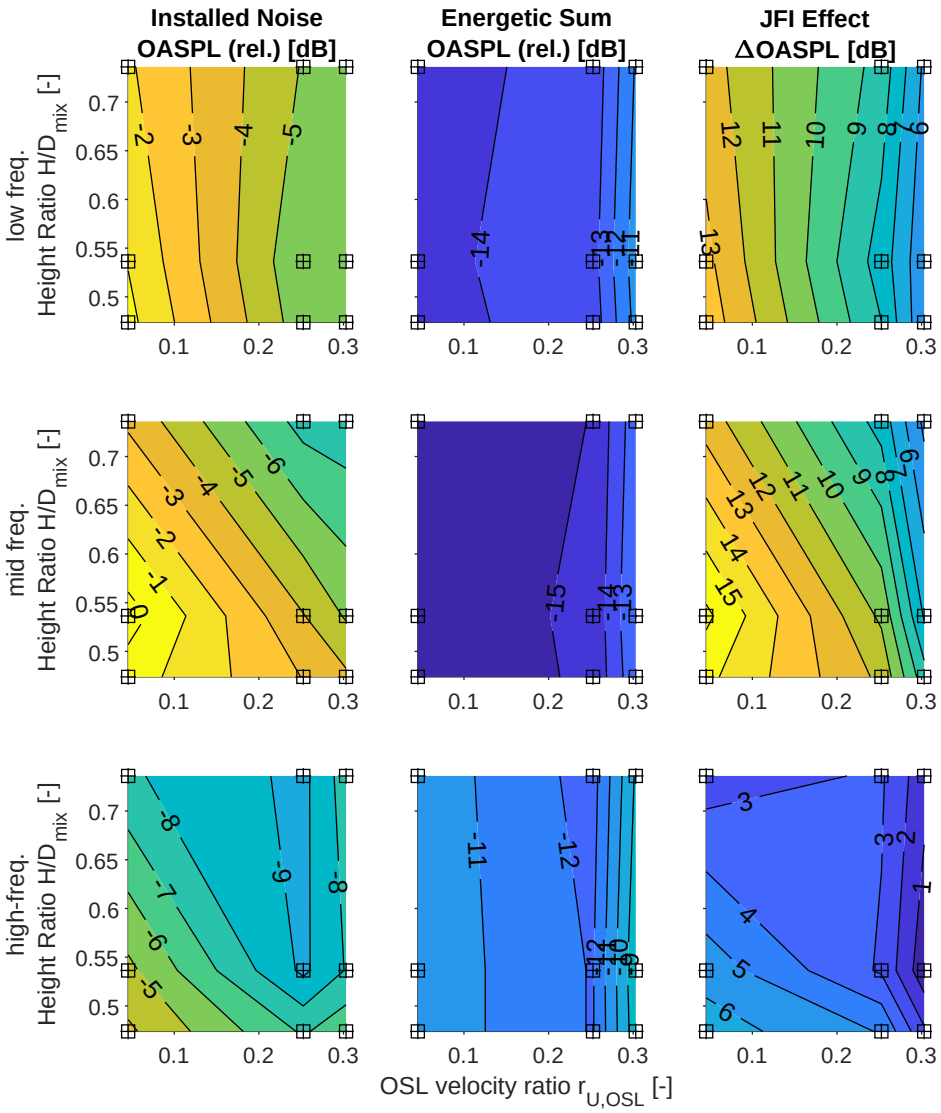

Figure 6.3.: **Height variation study (LIST-Engine operating at APCB (M=0.5), DLR-F16 dF=25deg, mic=90deg)**

Change of length The change of the length causes a change of the shear layer thickness which interacts with the flap trailing edge. Since the spreading of the outer shear layer is rather small ($\alpha_o = 0 \ldots 7\,^\circ$), small changes in length are less sensitive than small changes in height. An example of a rather large length variation is included in the example in section 6.4.2. In this example, the change of length is used to compare the effect of two operational settings with the same theoretical initial conditions at the flap trailing edge using OSL width conservation.

Change of engine type One important question of new engine options is how two different engine types can be installed to the same wing at comparable engine integration settings so that they present similar physics w.r.t. jet-flap interaction. The short answer to the question is that a similarity parameter has not been found yet. From a practical viewpoint, the new engine position is determined by simulation and must be optimized w.r.t. multiple factors. But for academic purposes and testing it would be great to find and use such a similarity in order to generalize JFI physics. The following candidates are thinkable:

1. shifted position: $H - R_{mix} = \text{const.}$ & $L - x_0 = \text{const.}$ (1D similarity parameter)

2. scaled position: $H/R_{mix} = \text{const.}$ & $(L - x_0)/R_{mix} = \text{const.}$ (1D similarity parameter), outer shear layer thickness at flap trailing edge changes.

3. Several 2D similarity candidates accounting for areas (cross-sectional/projected or real geometry), where intersection areas and/or redistribution areas are evaluated (see appendix K).

A thorough study for the similarity between two different engine types has not been conducted and it is out of scope for the dissertation. As a first idea, for similarity of engine options w.r.t. jet-flap interaction take candidate 1. It suggests that the top point of the outer shear layer origin remains at the same spot, i.e. the length L is approximately constant. In order to achieve this, the top point of the engine nozzle exit plane stays approximately at the same position. Yet, similarity candidate 1 does not produce similarity in intersection and/or redistribution areas.

Comparing two different engine operations with different mixing radius (e.g. same speed jet vs. bypass flow only/no core flow) does reflect very similar similarity questions as the change of the engine.

6.2. Build study of aircraft definition parameters using elemental motion analysis

It would be great to know any effects which result from changing engine integration and flap parameters because these parameters are the geometries which are typically used to characterize an aircraft. However, a simple change to those parameters typically affects the JFI physics in more than one dimension. The study of elemental motions w.r.t. a fixed flap trailing edge position solves this problem.

The engine integration is defined between the engine (origin is here the point of interception between Bypass outlet plane and the jet axis, BOC) and the main wing (wing clean chord leading edge, WLE). Four parameters are typically used: a horizontal distance L, a vertical distance H as well as engine yaw angle and engine pitch angle (see figure 6.4).

Furthermore, the flap positioning is defined between main wing and flap by the parameters gap, overlap (OvL), and flap deflection angle (δ_F). The more vertically relevant parameters are gap and flap deflection angle.

All of those parameters influence the relevant isolated jet shear layer parameters at the position of the flap trailing edge (FTE). From an academical point of view, the effects caused by aircraft definition parameters can be studied very well as long as the initial conditions for the jet shear layer remain constant. However, this is typically not the case:

Take the effect of changing the flap setting as an example (figure 6.5). A new flap setting does not only cause a change of the flap deflection angle[1], but also a shift of the flap trailing edge height. The effect caused by changing the flap setting can be better evaluated if the two different flap settings can be studied at the same primary build parameters, a so-called *elemental motion analysis* (EMA) with reference to a fixed trailing edge position. Such a study with the same primary parameters is rather academic. However, it allows for comparable initial conditions of the isolated jet shear layer and helps to identify how much of the effect is induced by height and how much is caused by the different pressure field, flap inclination etc.

The change of the flap setting for $\delta_F = 25\,^\circ$ (1) to the flap setting for $\delta_F = 35\,^\circ$ (3) can be decomposed by *elemental motions* around the flap TE. The first elemental motion (1-2) is to change the flap setting, while keeping the engine integration

[1] Gap and overlap were changed as well to the correct reference setting.

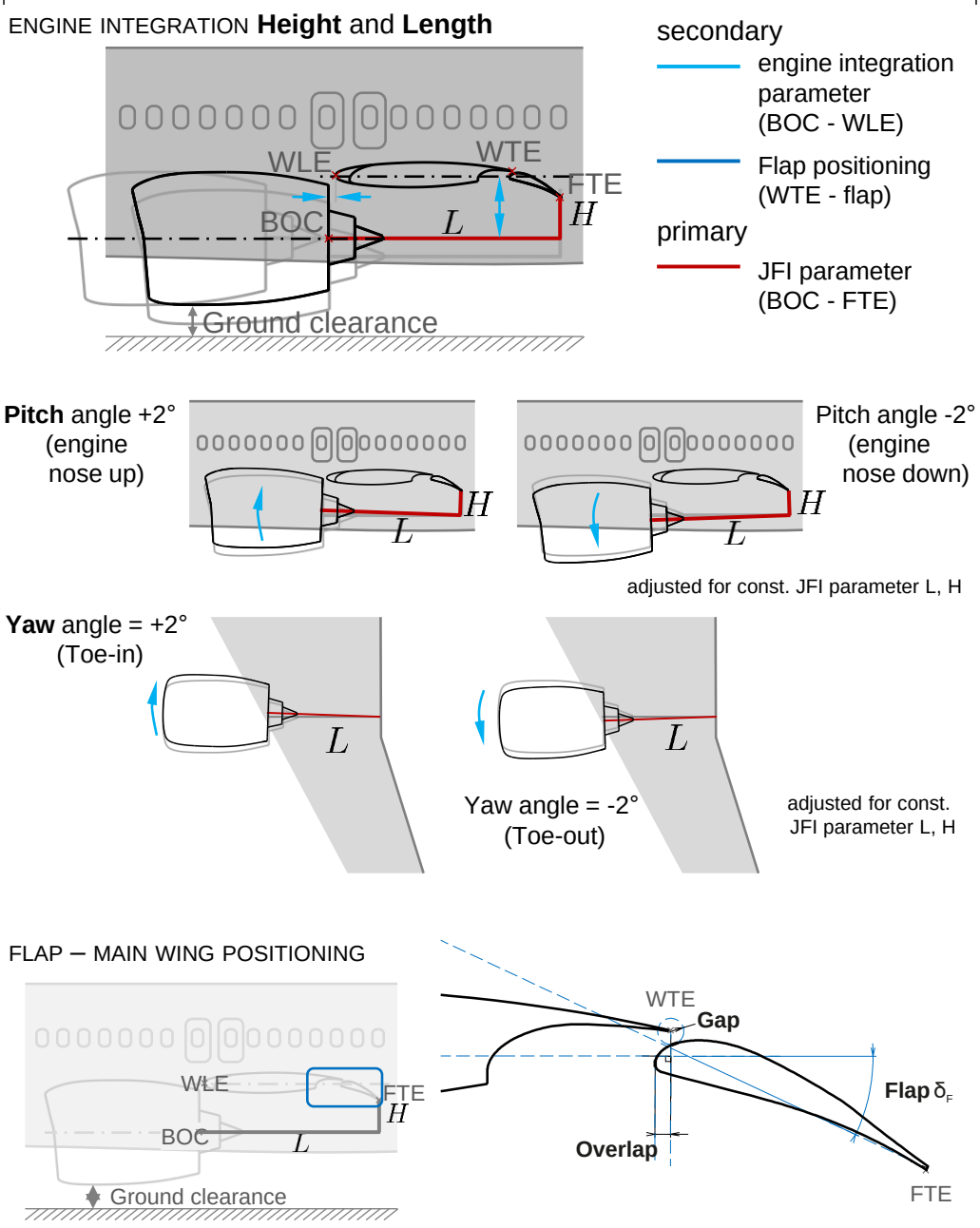

Figure 6.4.: **Aircraft definition parameters (secondary)**

height H, a primary interaction parameter, constant. This is the secondary effect about which insights need to be gathered: The (isolated) shear layer as well as the flap trailing edge are still at the same position, but the main wing is positioned farther away from the engine. Hence, it must be checked whether the other source region remains at the same sound pressure level in order to make sure that the engine integration effect results from the flap. The second elemental motion is the change in height to the new flap trailing edge position (2-3). This allows to account for the height change which is a primary effect. The position of the main wing of 1 and 3 are the same.[2]

The difference in the overall sound pressure levels show that both of the elemental motions, the steeper flap setting as well as the change of height increase jet-flap interaction noise.

Summary The measurement of aircraft relevant parameters can be separated by the elemental motions listed in table 6.1. Some of the aircraft relevant parameters are equivalent to a single elemental motion: changes in engine integration height coincide with changes in the JFI height H. Small changes in JFI length L are assumed to be negligible, especially in comparison to small height differences. As a result, the yaw angle can be studied without the help of any elemental motions.

If the variation of an aircraft parameter requires a difference in JFI height, then the elemental motion analysis helps to identify whether an aircraft parameter actually benefits JFI or whether this is an effect stemming from the new engine integration height. Note that an overlap study causes small geometrical shifts which do mainly affect the JFI length, but may also lead to tiny changes in height.

The assessment of the pitch angle can be studied in 3 elemental motions: change of height, flap pitch (by adjustment of flap deflection angle) as well as main wing pitch.

[2]The method is explained in simple terms for reason understanding. As two different heights are studied, there is not only one, but two elemental motion data points which can be compared and evaluated. The more sophisticated method takes the $25\,°$ flap at $H/D_{mix} = 0.42$ into account.

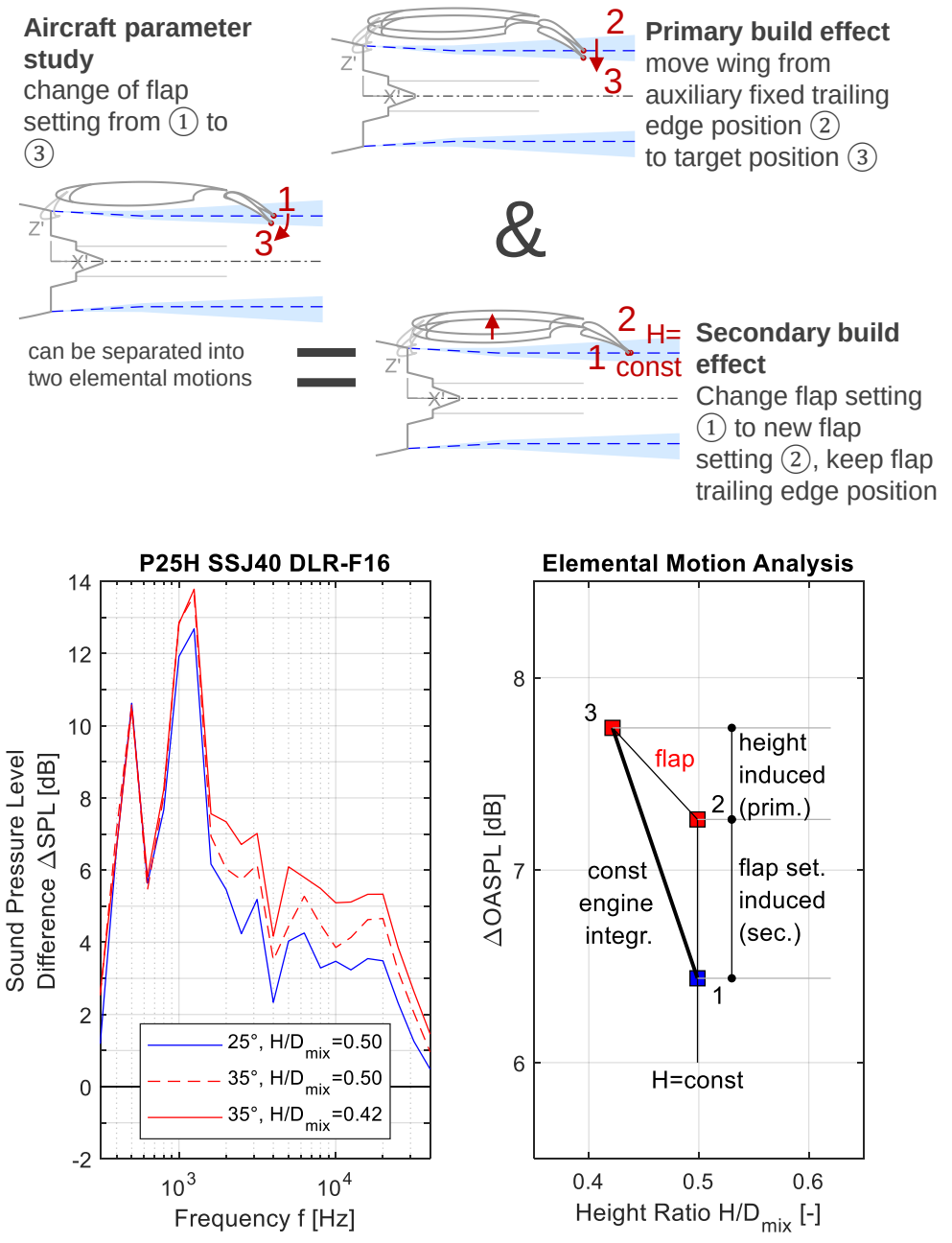

Figure 6.5.: **Evaluation of secondary effects using elemental motion analysis**

Table 6.1.: **Geometric definitions and elemental motion study of JFI (small changes in length neglected)**

		move		engine integration build		crucial elemental motions			
Type	**Parameter**	↔	↕	**other SR**	**flap SR**	#	**1st**	**2nd**	**3rd**
engine	Height		X	check		1	ΔH		
inte-	Length	X		check		1	ΔL		
gra-	Pitch $\pm 2\,^\circ$		X	check		3	ΔH	$\Delta\alpha_{Flap}$	$\Delta\alpha_{Wing}$
tion	Yaw $\pm 2\,^\circ$	(X)		check		≈ 1	ΔYaw		
flap	Flap deflection		X	const.		2	ΔH	$\Delta\delta_F$	
	Gap $\pm 1\,c$		X	const.		2	ΔH	ΔGap	
	Overlap $\pm 1\,c$	(X)	(X)	const.		1-2	(ΔH)	ΔOvL	

6.3. Build analysis of aircraft parameter sensitivities around a reference setting

Elemental motion studies are special cases of parameter sensitivity studies around a fixed reference setting. They require the evaluation of the reference build at the same fixed trailing edge position. This strict positioning allows to evaluate and compare full spectra instead of merely OASPL. However, builds are costly in wind tunnel campaigns. Especially, if two settings are similar, e.g. height difference within installation uncertainty $\Delta H \leq 0.5\,\mathrm{mm}$, it may not be worth the money to measure such a setting. Instead, a more interesting setting can be chosen and the physics for the needed auxiliary setting can be interpolated. Such an interpolation is only good as long as there are sufficient data points or known physical laws to back up the interpolation. The advantage of this method is that each aircraft parameter can be tested according to its own practically relevant and freely chosen resolution around a priorly defined reference setting. Unfortunately, the comparison of sensitivities is only feasible in OASPL and therefore a bit more uncertain.

The following study (figure 6.6) shows the build sensitivities of aircraft parameters that alter mainly the height, i.e. gap, flap deflection angle and the height shift of the entire wing. The results have been published in detail by Jente et al. [25]. All of the settings operate with the Power25 engine on the Approach setting APP60 ($r_{U,OSL} = 0.47$). This is a low thrust setting where wing-related noise is more significant than isolated jet noise. Even though the expected JFI deltas are small, jet-flap interaction noise can be measured. Only the integrated beamforming spectra in the flap source region have been used for the evaluation in order to analyse only the flap-induced effects.

A general result of the study is that a decreasing jet-flap integration height increases the jet-flap interaction noise delta. Acoustical benefits can be achieved at flat flap deflection angles, small gaps as well as large engine integration heights. Since the space is limited, information about the sensitivity of each of the parameters is valuable: It can be shown that slight variations of the gap are particularly sensitive compared to the variation of the flap deflection angle or the height variation.

Due to low number of interpolation points, this conclusion can be only drawn when making assumptions on the physical behavior of the flap deflection angle (2 data points) and height variation (3 data points). The gap variation is well-resolved because of the small changes compared to the other two parameters. According to Belyaev et al. [4], the flap deflection angles have a linear influence on jet-flap interaction noise. The TsAGI team investigated the effect of seven flap deflection angles ($\delta_F = 5\,^{\circ} \ldots 36\,^{\circ}$) on JFI noise at their anechoic chamber AC-2 facility. The previous study on height variances shows an inversely proportional behavior of jet-flap interaction noise versus height for $H - H_{OSL,o} \geq 0$. For $H < R_{mix}$, a non-linear interpolation has been also used.

The interpolations of the sensitivity study in figure 6.6 make it difficult to judge whether the flap effect or height effect are more important. This is a clear referral for the advantages of elemental motion analysis.

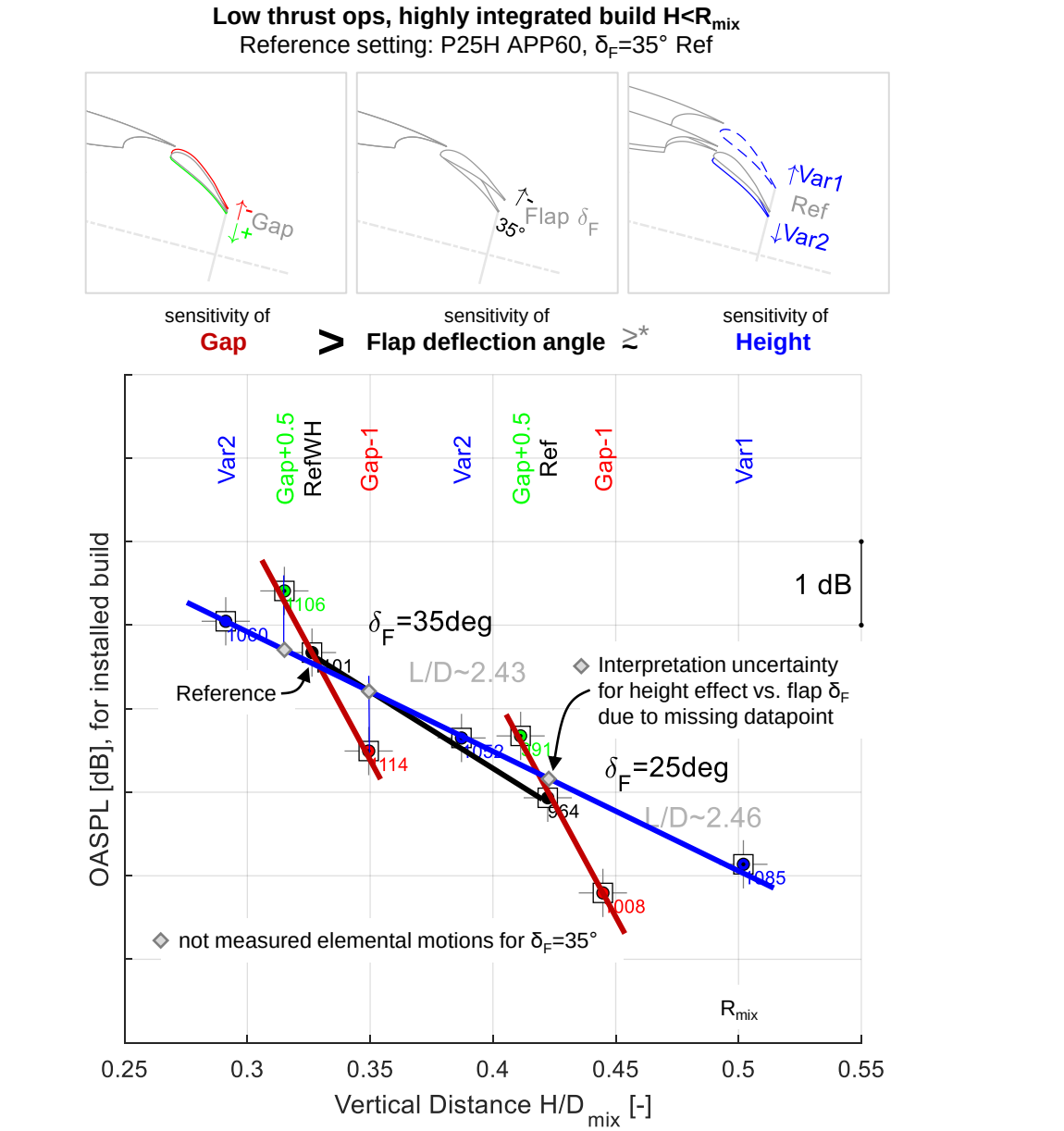

*This has been shown in the previous section (EMA), but cannot be derived from this diagram: There is some uncertainty in the sensitivity analysis due to interpolation with low number of datapoints.

Figure 6.6.: **Aircraft parameter sensitivity study**

6.4. Operational parameters

In the previous chapters, the jet-flap diagram was introduced. The x-axis of the diagram is the velocity ratio because it is the one relevant operational parameter in order to geometrically describe the isolated jet shear layer. This does not mean that it is also the acoustically characterizing parameter for jet-flap interaction noise. This section provides answers on how to test jet-flap interaction w.r.t. operational parameters.

While the previous build parameter study used fixed operational parameters, the study of operational parameters requires a comparable build (see table 6.2): The LIST engine is integrated to the DLR-F16 wing at reference position and the flap at the $\delta_F = 25\,^\circ$ (see figure 6.7). This corresponds to a height ratio of $H/D_{mix} = 0.48$.

Table 6.2.: **Comparable builds for the study of operational JFI parameters**

S/L constant	symbol	build
velocity ratio	$r_{U,OSL}$	fixed
difference velocity convection velocity mean velocity	ΔU $U_c = c_U \Sigma U$ $\overline{U}$	mainly length adjustments

6.4.1. Analysis of operational parameters with the same velocity ratio

A shear layer with constant velocity ratio $r_{U,OSL}$ is self-similar and can therefore be measured with a fixed build. The data has been evaluated as overall sound pressure levels in the high frequency region using the 4/2 measurement method (see section 4.8). The following conclusions can be drawn (see figure 6.7):

- The installed overall sound pressure level is large for high difference velocities and velocity ratios (see figure 6.7, installed OASPL), i.e. for large thrust velocities.

- The high frequency jet-flap interaction delta $\Delta OASPL_{JFI}$ depends more on the velocity ratio rather than the difference velocity. It is particularly strong for high difference velocities with comparably low wind tunnel velocity, i.e. the setting which is closest to a static jet setting.

- The energetic sum is not constant for the same velocity ratio, contrary to the

special case of testing the same jet velocity (compare figure 6.3).

Studies with constant velocity ratios can be used to identify an overall scaling exponent $q = o + m + n + p$.

$$I \propto U_{jet}^{o}(\Delta U)^{m}(\Sigma U)^{n}U_{\infty}^{p} \tag{6.1}$$

$$I \propto U_{jet}^{o+m+n+p} \underbrace{(1 - r_{U,OSL})^{m}(1 + r_{U,OSL})^{n}(r_{U,OSL})^{-p}}_{\text{const.}} \tag{6.2}$$

For a constant velocity ratio, any velocity parameter scales with the same exponent, since all the velocity parameter candidates depend on the velocity ratio (see lines in figure 6.8, $q = 5.8$). In this particular example, the overall sound pressure levels have been derived for the installed build and the high frequency range.

Two parameters appear to be very promising candidates for scaling because they align well even for different velocity ratios: the acoustic speed U_{ac} as well as the thrust speed U_{thrust} (defined below).

$$U_{ac} = U_{jet} \cdot (1 - r_{U,OSL})^{5/8} \left(0.5 \cdot (1 + r_{U,OSL})\right)^{3/8} \tag{6.3}$$

$$U_{thrust} = \sqrt{U_{jet} \cdot \Delta U} = U_{jet} \cdot \sqrt{1 - r_{U,OSL}} \tag{6.4}$$

An open research question is whether operational similarities of different velocity ratios can be measured using a fixed build. It is unclear, whether the OASPL values in figure 6.8 have to align. One could argue that the impact conditions for comparing similar conditions at the flap trailing edge are not the same. Take the study of velocity ratios for the same shear layer difference speed ΔU as an example: the three velocity ratios cause three different shear layer thicknesses at the flap trailing edge (compare the isolated jet shear layer in figure 6.7).

6.4.2. Shear layer width conservation at the flap trailing edge

A test hypothesis for a similar criterion could be the same theoretical isolated shear layer thickness (see equation 3.8). This requires the engine integration position to shift[3] in length L for changing velocity ratios. There are three viable options in order to integrate two comparable shear layers to the wing (see figure 6.9).

[3]The microphones should be fixed w.r.t. the flap trailing edge. If the engine is fixed and the wing is adjusted, the microphones should be shifted. For a high number of microphones, the shift may not be necessary

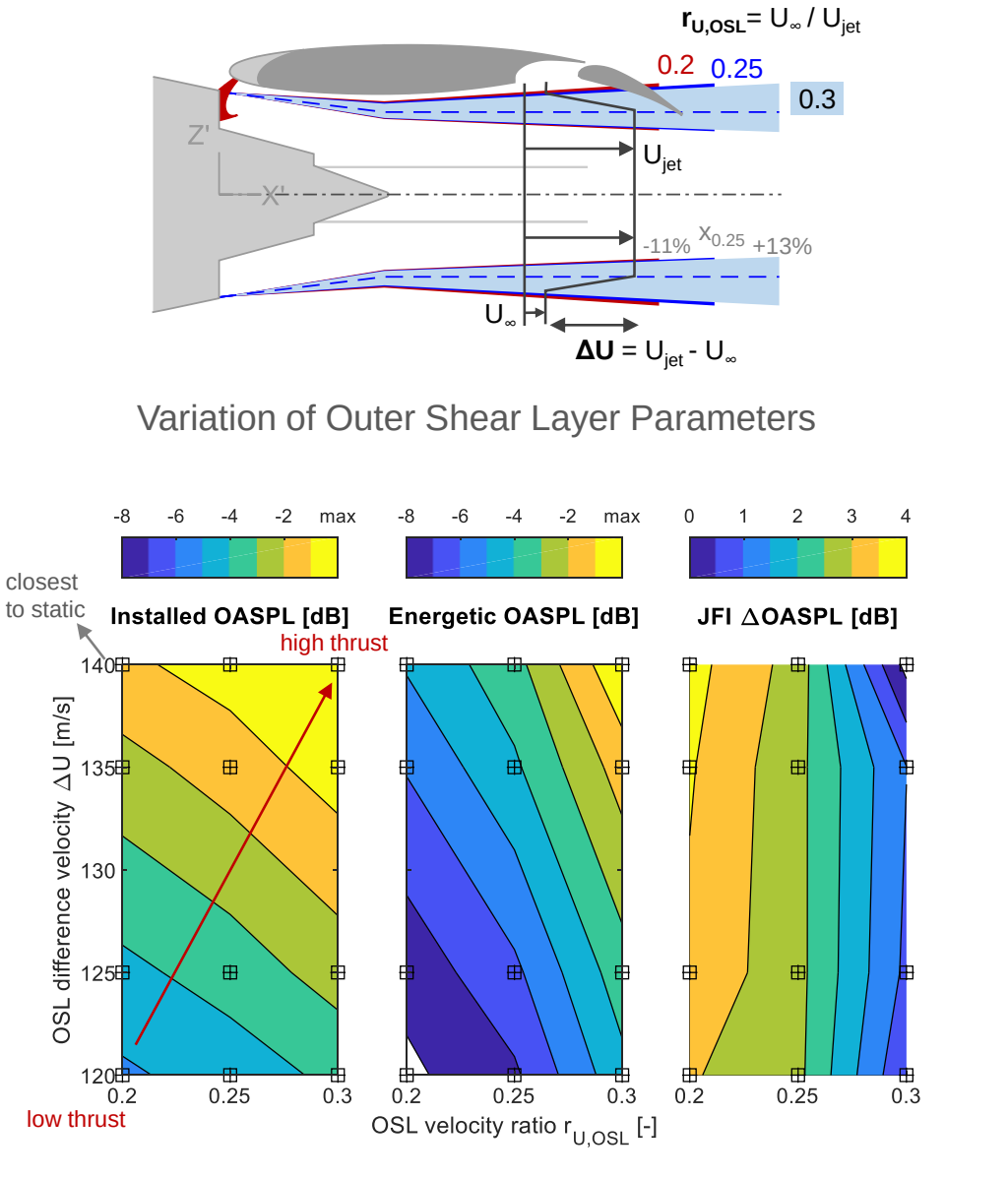

Figure 6.7.: **Shear layer parameter evaluation for high frequency JFI-effect**

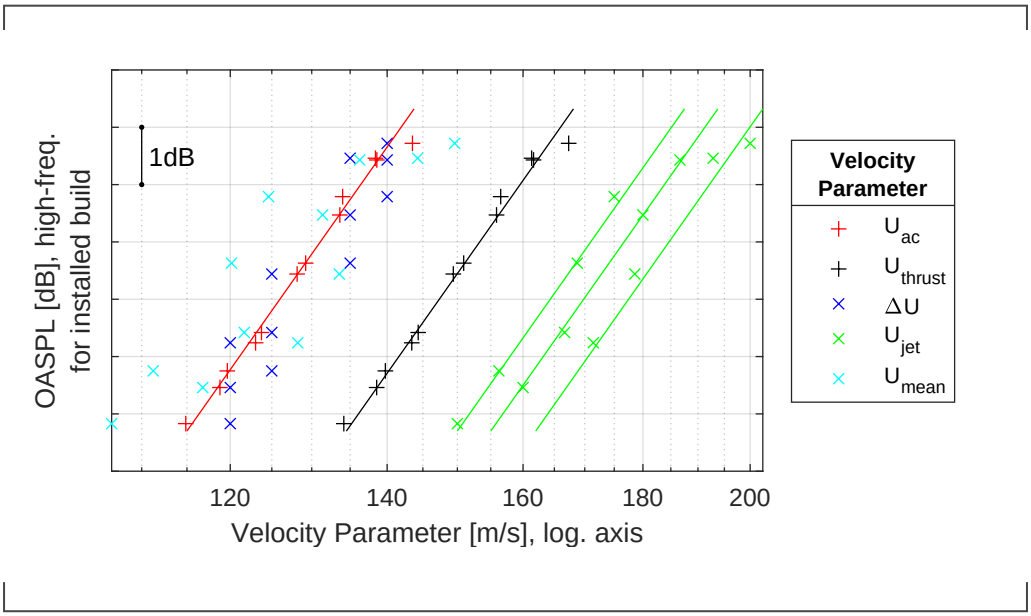

Figure 6.8.: **Velocity scaling parameter for high frequency JFI. Same 12 data points as in figure 6.7, shown in different color for each velocity candidate. The lines connect data points of constant velocity ratio $r_{U,OSL}$ and represent an exponent of 5.8.**

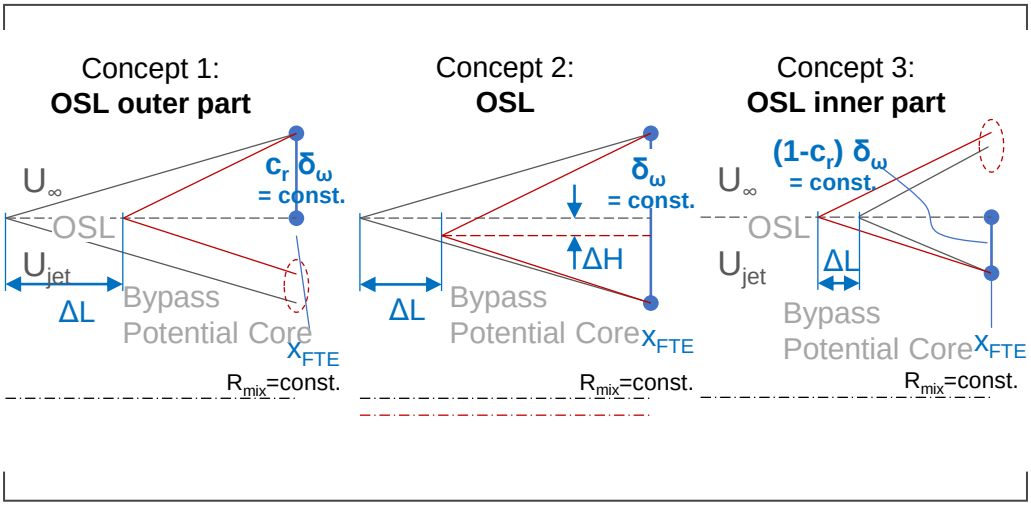

Figure 6.9.: **Three options for OSL width conservation**

1. Constant OSL outer part, i.e. the mixed jet radius remains at the same position (equations 6.5 to 6.7). The bypass jet potential core shifts.

$$H_{OSL,o} - Rmix = \text{const.} = c_r \cdot \delta_\omega \tag{6.5}$$
$$H - H_{OSL,o} = \text{const.} \tag{6.6}$$
$$H = \text{const.} \tag{6.7}$$
$$(L - x_0) = \frac{1}{c_r}\frac{1 + r_{U,OSL}}{1 - r_{U,OSL}}\frac{\sigma_0}{\sqrt{\pi}}\underbrace{(H_{OSL,o} - R_{mix})}_{\text{const.}} \tag{6.8}$$

   The length L changes mainly depending on the new outer shear layer velocity ratio $r_{U,OSL}$ (see equation 6.8).

2. Constant shear layer thickness (equation 6.10), the bypass jet potential core remains at the same position. The engine changes in height because of different convection parameters c_r (equations 6.10 to 6.12).

$$\delta_\omega = \text{const.} = \frac{H_{OSL,o} - R_{mix}}{c_r} \tag{6.9}$$
$$H_{OSL,o2} = H_{OSL,o1}\frac{c_{r,2}}{c_{r,1}} - R_{mix}\left(\frac{c_{r,2}}{c_{r,1}} - 1\right) \tag{6.10}$$
$$H_1 - H_{OSL,o1} = H_2 - H_{OSL,o2} = \text{const.} \tag{6.11}$$
$$H_2 = H_{OSL,o2} + H_1 - H_{OSL,o1} \tag{6.12}$$
$$(L - x_0) = \frac{1 + r_{U,OSL}}{1 - r_{U,OSL}}\frac{\sigma_0}{\sqrt{\pi}}\underbrace{\frac{H_{OSL,o} - R_{mix}}{c_r}}_{\text{const.}} \tag{6.13}$$

3. Constant OSL inner part, i.e. the mixed jet radius remain and the bypass jet potential core stay at the same position (equations 6.14 to 6.16). The jet shear layer width changes.

$$H_{OSL,i} - R_{mix} = \text{const.} = (1 - c_r) \cdot \delta_\omega \tag{6.14}$$
$$H - H_{OSL,i} = \text{const.} \tag{6.15}$$
$$H = \text{const.} \tag{6.16}$$
$$(L - x_0) = \frac{1}{1 - c_r}\frac{1 + r_{U,OSL}}{1 - r_{U,OSL}}\frac{\sigma_0}{\sqrt{\pi}}\underbrace{(H_{OSL,i} - R_{mix})}_{\text{const.}} \tag{6.17}$$

   The length L changes mainly depending on the new outer shear layer velocity ratio $r_{U,OSL}$ (see equation 6.8).

The three options depend on an estimation of the way the outer shear layer is compressed, as well as which parts of the potential core are deformed. In order

to perform an experiment with good similarity, shear layer parameters must be determined with good accuracy. As long as this is not possible, it is advisable to test all of the methods in order to verify or reject the hypothesis. If it can be assumed that the estimation of the convection parameter c_r amounts to some uncertainty, option 1 or 3 might be preferred. This is because the uncertainty is projected in the length L alone which is less significant to the jet-flap interaction effect than the height H.

There is the possibility that two builds are comparable if the changes caused by different length scales are dimensionally negligible. Assume that the three velocity ratios in figure 6.7 are compared. Then, the correct lengths are $L_{0.3} \approx 1.13 \cdot L_{0.25}$ and $L_{0.2} \approx 0.89 \cdot L_{0.25}$ according to option 1 (equation 6.8). This change by approximately $L_{0.25} \pm 12\,\%$ is rather large, but how much does it affect the studies?

For the investigation of the length scale shift problem, a slightly different data set is used (figure 6.10). The effect of the wind tunnel speed is studied with two operational settings, (1) CB60[4] ($r_{U,OSL} = 0.3$) and (2) CB50 ($r_{U,OSL} = 0.25$). If the build is fixed ($1 \rightarrow 2$), operation 2 produces a larger shear layer at the flap trailing edge. Furthermore, the velocity difference ΔU between jet and wind tunnel flow increases. Those two effects cause a full-scale jet-flap interaction delta of approx. $\Delta OASPL_{JFI} = 1.8\,\mathrm{dB}$. Both effects can be separated with OSL width conservation around the flap trailing edge:

- The data point (3) which resembles common features of both operational settings is defined by a shifted length L where an isolated engine produces the same shear layer width at the virtual[5] flap trailing edge position. The length shift can be calculated based on the velocity ratios (here: option 1, equation 6.8).
  The comparison ($1 \rightarrow 3$) with similar impact conditions at the flap trailing edge shows that the change in wind tunnel velocity contributes most of the jet-flap interaction delta, i.e. $\Delta OASPL_{JFI,13} = 1.3\,\mathrm{dB}$. The first frequency peak is approximately similar in ΔSPL.

- The horizontal shift from $3 \rightarrow 2$ at the same operations results in a smaller change in jet-flap interaction noise ($\Delta OASPL_{JFI,32} = 0.5\,\mathrm{dB}$). The length shift influences the frequencies: The 2^{nd} peak is similar in ΔSPL, but slightly shifted in frequency. Hereby, the smaller length corresponds to a higher frequency. In the past, the length between nozzle lip and flap trailing edge has been used in order to determine a characteristic length scale for shear layer eddies passing the flap trailing edge (see Miller[35], p.2, or Mengle[30], p.18).

[4] CB (Cutback) is an operation with a mixed jet velocity of ≈ 200 m/s, the wind tunnel velocity is 60 m/s.
[5] The wing is not installed in an isolated engine test setting. Thus, the point is not real, but virtual.

Hence, this example shows that the changes which are due to different shear layer thicknesses δ_ω lead to rather small jet-flap interaction noise deltas of $\Delta OASPL_{JFI,32} = 0.5\,\mathrm{dB}$. Such a margin could potentially eliminate the little discrepancies in overall sound pressure level for the same difference velocities ΔU in figure 6.8. Then, jet-flap interaction noise could possibly scale with the difference velocity ΔU. In order to be certain about the velocity scaling, a study based on constant shear layer width at the flap trailing edge is suggested for future work and a test campaign was proposed by Jente [22].

The take-away from this section is that testing with a high number of academically suitable test operations (compare also the static JFI tests of PPRIME, e.g. [28]) will enhance the potential of the physical understanding of the effect.

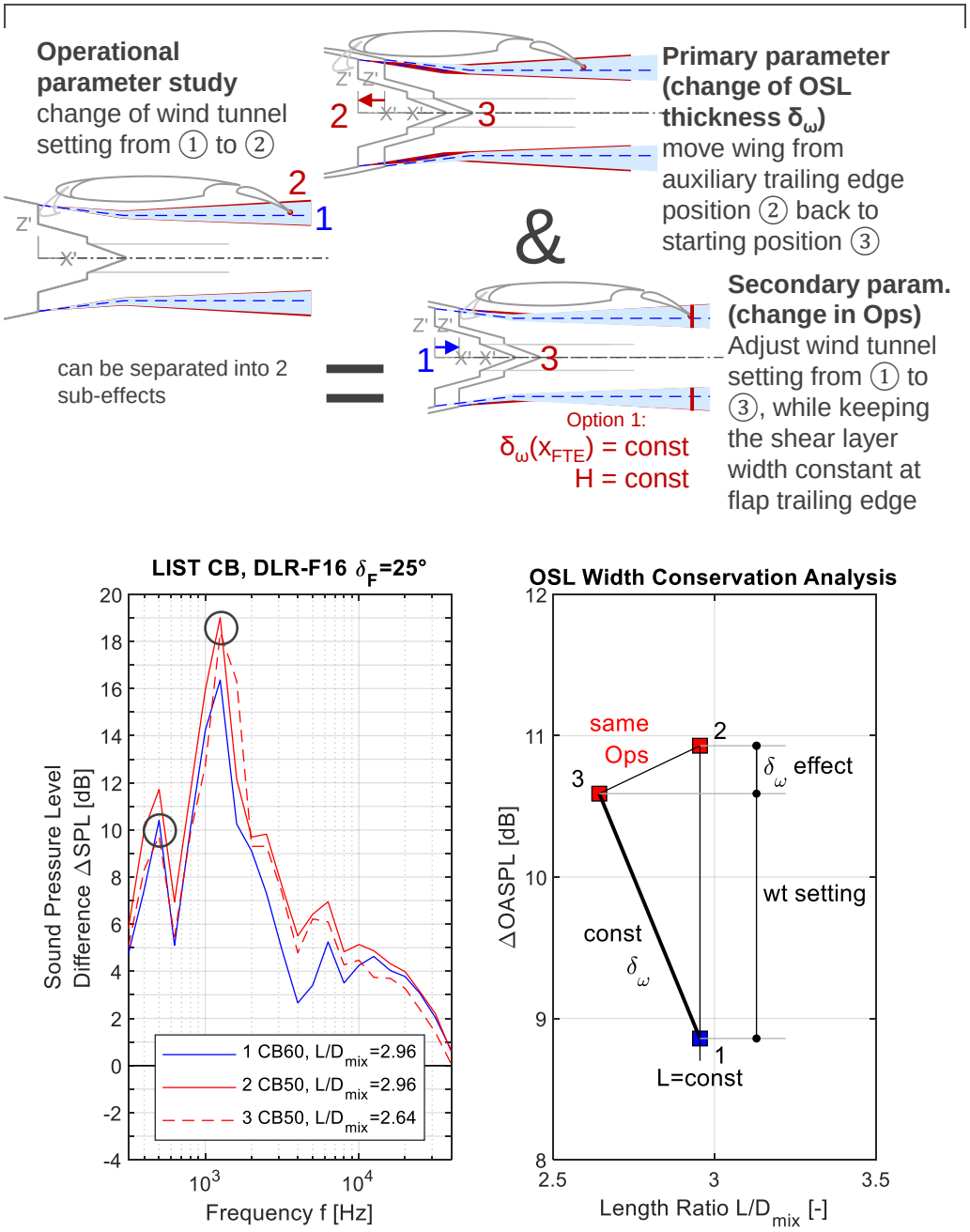

Figure 6.10.: **Operational parameter study using OSL width conservation at flap TE**

7. Summary

The dissertation work is subdivided into the building of the experimental setup and the theoretical modelling, testing and evaluations. The AWB secondary air supply was redesigned for aeroacoustic testing of UHBR nozzles. Duct noise tests, external measurements as well as industry data reveal that the test conditions are good, but not ideal. The ducts represent real engine conditions, the measured spectra are not very smooth. The engine model and the related noise sources region are rather large for testing in the AWB facility. Consequently, the far-field microphones are installed too close to produce reliable information on directivity. A decrease of the model below F16 high-lift wing size is not feasible.

What is jet-flap interaction noise? The conducted experiments help to address the question for a practical definition and physical description of the jet-flap interaction effect: Jet-flap interaction noise is an acoustic engine integration phenomenon which is caused by an under-the-wing engine installation at low distance between engine axis and flap trailing edge.

The engine integration is a 4-body problem (engine, as well as slat, main wing, flap) and contains 3 flow potentials (flight, bypass, core stream). This means that the amount of parameters included in this problem is high. In order to reduce complexity, a very simple model is key to understanding the more complex sides of the physics.

Jet-flap interaction is related to jet impingement problems. Contrary to jets impinging on perpendicular (rocket vs. ground) or inclined plates (jet vs. runway), the length scale and associated streamwise jet regions is not the most sensitive property. Instead, the positioning of the flap trailing edge restricts the flow which interacts with the flap to the jet initial region (streamwise positions of $L/D_{mix} = 1 \ldots 5$). Hence, jet flow characteristics normal to the streamwise direction, such as the bypass potential core and the outer shear layer become relevant.

The flow characteristics of an isolated jet can be modeled by calculating the mixed jet radius, the shear layer width (using a thin mixing layer) as well as a function which divides the shear layer width into outer part OSL and inner part OSL. The shear layer geometry at the flap trailing edge is defined by conical geometries, especially the

characteristic features which define the arc tangent of the half cone angle: height position of bypass core and outer shear layer, mixed jet radius, length, virtual shear layer origin, velocity ratio between flight stream and bypass jet.

The wing coordinates, especially the flap trailing edge, can be also expressed in the same cone angle coordinates. This allows to compare the 1D geometry of isolated jet shear layer space requirements and flap space constriction for each velocity ratio $r_{U,OSL}$ (abbreviated as jet-flap diagram). This basic diagram is valuable with additional information on the deformability of the jet shear layer.

A closer look on operations shows that two different physical problems must be investigated: a jet-like shear layer flow that interacts with a finite plate (static operations) or airfoil (flight operations).

A first acoustic evaluation targets jet-flap interaction for static jets or high thrust settings with negligible wing-related noise. For the evaluation of static jets, the 2/2 method has been shown. The 4/2 method has been developed for thrust settings with negligible wing-related noise.

It could be shown that the flap is positioned at a spatial region which is fits neatly in between nozzle exit noise and the downstream jet peak noise. The flap noise is also not particular characteristic for high-lift wing noise, when compared against slat-related noise sources.

JFI noise originates within the region around the flap and propagates to the observer approximately perpendicular to the flap pressure side (forward arc).

In the shown third-octave spectrum, there are two broadband like peaks of $10 \ldots 20\,\mathrm{dB}$, one in the low and one in the mid frequency region.

The low frequency JFI effect is defined for $He < 1$. This part of the JFI effect can be detected even if the engine integration height is rather large. As the jet pressure near field fluctuations scatter at the flap trailing edge, a pressure wave propagates into the far-field. The lateral decay of the pressure wave is rather small for low jet speed. This explains why there is the anomaly that slow jets produce a higher low frequency JFI effect than fast jets.

The mid frequency JFI effect is located around $He_L = 1$ and prone to tones (additional $20 \ldots 30\,\mathrm{dB}$) at high jet speed. Hence, this is the most prominent jet-flap interaction noise feature. The largest low-frequency peaks can be found for high thrust static jets and installation heights $R_{mix} \leq H \leq H_{OSL,o}$.

The high frequency JFI effect is non-tonal and consists of a smaller constant broadband-

like delta than low and mid frequency JFI. It is rather large for highly integrated builds $H/D_{mix} < 0.5$ at static operations and high-thrust settings.

A height study shows that jet-flap interaction noise sets in at $H/D_{mix} = 1$, which corresponds to an installation angle of $\alpha_{geo} = 9.5\,^{\circ}$. At velocity ratios higher than a certain limit, e.g. $r_{U,OSL} \approx 0.3 \ldots 0.5$, the jet-flap interaction effect loses importance in comparison to other aircraft-relevant sources such as high-lift noise.

How can JFI noise be measured acoustically? The commonly used method to conduct static jet-flap interaction noise tests is suitable within limits, but must be extended to account for the wind tunnel speed. This causes two effects: (1) If the wind tunnel speed is switched on, the engine integration region around slat, engine and pylon may become another source region. Academic experiments with the goal to measure jet-flap interaction alone take action to minimize effects from the other noise source (e.g. 2D-extruded wing profile, minimization of 3D effects, no pylon). If the other source region is significant in comparison to the flap source region, source location measurement and corresponding evaluation methods are advised.
(2) Not only jet noise, but also slat-related noise sources (3-element wing) are aircraft-relevant signals which can be measured individually. The best guess for the combined noise is the energetic sum of isolated jet noise and isolated high-lift wing noise.

This combined noise is subtracted from the measured installed noise in order to calculate the jet-flap interaction delta.

The most general measurement method for one jet-flap interaction evaluation requires six data points and five builds (6/5 technique).

There are operational points where either of the isolated noise sources is greater than the other one. This allows a shorter evaluation chain, the 4/4-technique. For the example of a certain combination of engine type and wing section, velocity ratios of $r_{U,OSL} < 0.2$ allow to neglect isolated high-lift wing noise and velocity ratios $r_{U,OSL} > 0.5$ allow to neglect isolated jet noise. The values depend on a variety of parameters and must be evaluated for each model and wind tunnel anew.

Depending on the engine and wing, a processing quality gap should be expected at velocity ratios where isolated jet noise is smaller than high-lift wing noise, but not negligible.

Which aerodynamic effects are present around the flap? In order to find an answer on the differences between the combined isolated noise sources and the

jet-flap interaction noise source, the corresponding flow fields are investigated.

In a thought experiment, the jet-like shear layer flow underneath an airfoil is studied as a 3/4 open channel flow which is centered around the engine axis. This leads to the mass-damper analogy: The shear layer works like a damper; it is a flow which can be compressed. The potential core is more rigid and works like a mass; it must turn or be reshaped.

In an analysis of flow properties normal to engine axis it has been shown that the jet top part gets straightened (reshaped). Moreover, the flow forcefully turns, unless (1) there is enough space (shear layer vortex possible), (2) there is even more space (unharmed jet) or (3) a natural turn is happening (strong downwash behind flap). These results can be portrayed in the jet-flap interaction diagram.

An external flow study near the flap trailing edge shows that there is a local flow acceleration underneath the flap. This acceleration is particularly strong for high thrust settings. The acceleration near the flap trailing edge is studied with pressure data. It reveals that without any jet or the flap being far away from the jet, there is no impact. High static pressures can be shown for cases where the flap is interacting with the jet shear layer. One result is that the steeper flap produces the higher accelerations. In the following examples, it can be shown that this corresponds well with the higher jet-flap interaction noise for steeper flap angles.

Which parameters influence JFI? How can they be measured? The jet-flap interaction parameters can be structured into build parameters and operational parameters. w.r.t. the conical shear layer geometry, primary parameters can be identified, the engine integration length, height, mixing diameter, virtual shear layer origin and OSL velocity ratio.

The easiest type of aircraft parameter studies can be made at a fixed engine operation (constant mixed radius): Build parameters can be compared by adjusting the model to the same height (and length). This is called a elemental motion analysis around a fixed flap trailing edge position. Operational parameters can be compared for the same velocity ratio.

It was found that out of the vertical parameters, Gap is a very sensitive parameter compared to the change of flap deflection angle or a height variation. High installed JFI noise is measured for high thrust settings. The greatest jet-flap interaction deltas can be seen for operations close to static operations and for high shear layer difference velocity ΔU.

Future work The details of the OSL width conservation are not solved in detail. Three options have been suggested for OSL width conservation: The conservation (1) of the full OSL width (i.e. outer and inner part), (2) of the outer part of the OSL, and (3) of the inner part of the OSL. It must be found out which of the options is the real conservation property.

Once this conservation property is known, OSL width conservation can be exploited in order to find velocity scaling laws.

The similarity parameters for comparing different mixed radii is presumably not known. This concerns both, different engine options (e.g. Power25 nozzle vs. LIST nozzle) as well as different engine operations at the same engine (e.g. same speed jet vs. bypass only). For very close engine integration, it is very likely to find an analogy based on areas (2D) rather than distances (1D). These areas could be the derived the cross-sectional flap intersection and redistribution areas. Such a 2D geometry analysis is the standard procedure in characterizing internal flow components and could be a logical follow up to further the jet-flap interaction studies.

While the above suggested methods are of rather theoretical nature, it is worthwile to extend studies to higher jet speeds where tonal JFI effects are present. Moreover, noise reduction technologies are to be investigated at static, flight and cruise operations.

A. Mixed jet mean flow properties

Mixed jet mean flow properties of short cowl nozzles are calculated by combining the bypass and core flow properties into mixed (or: effective) properties. The calculations are based on conservation of momentum, conservation of energy, definition of total temperature, ideal gas law, mass flow, and circular area (see Khavaran [29] or the standard SAE ARP876F).

The needed measurement properties are the mass flows and temperatures for core and bypass flow as well as the outlet pressure. The static pressure is assumed to be constant for all the flows as well as the mixed flow (subsonic nozzle outlet condition $p = p_{atm}$). In the nozzle exit region, some real expansion effects are expected (see figure A.1). This means that the static pressure is slightly greater than the ambient pressure. Since the acoustically relevant velocities are in fact mean flow properties $\bar{U}$ (compare Tam [44], p. 8), higher velocities[1] $\hat{U} \approx 1.1 \ldots 1.2 \cdot \bar{U}$ can be measured in the flow field.

$$\text{Bypass ratio: } \mu = \frac{\dot{m}_{Byp}}{\dot{m}_{Core}} \tag{A.1}$$

$$\text{Cons. momentum: } U_{mix} = \frac{\mu}{\mu+1} \cdot U_{Byp} + \frac{1}{\mu+1} \cdot U_{Core} \tag{A.2}$$

$$\text{Cons. energy: } T_{t,mix} = \frac{\mu}{\mu+1} \frac{[c_p]^{T_{Byp}}}{[c_p]^{T_{mix}}} \cdot T_{t,Byp} + \frac{1}{\mu+1} \frac{[c_p]^{T_{Core}}}{[c_p]^{T_{mix}}} \cdot T_{t,Core} \tag{A.3}$$

$$\text{Def. total temp.: } T_{mix} = T_{t,mix} - \frac{U_{mix}^2}{2 \cdot [c_p]^{T_{mix}}} \tag{A.4}$$

$$\text{Ideal gas law: } \rho_{mix} = \frac{p}{R T_{mix}} \tag{A.5}$$

$$\text{Cons. Mass: } A_{mix} = \frac{\dot{m}_{Byp} + \dot{m}_{Core}}{\rho_{mix} U_{mix}} \tag{A.6}$$

$$\text{Circ. Area: } R_{mix} = \sqrt{\frac{A_{mix}}{\pi}} \tag{A.7}$$

The sole purpose of the equations A.3 to A.5 is to calculate the density of the mixed

[1] This estimation is based on an empirical function for a velocity profile stated in Munson [36] and it depends on Reynolds number.

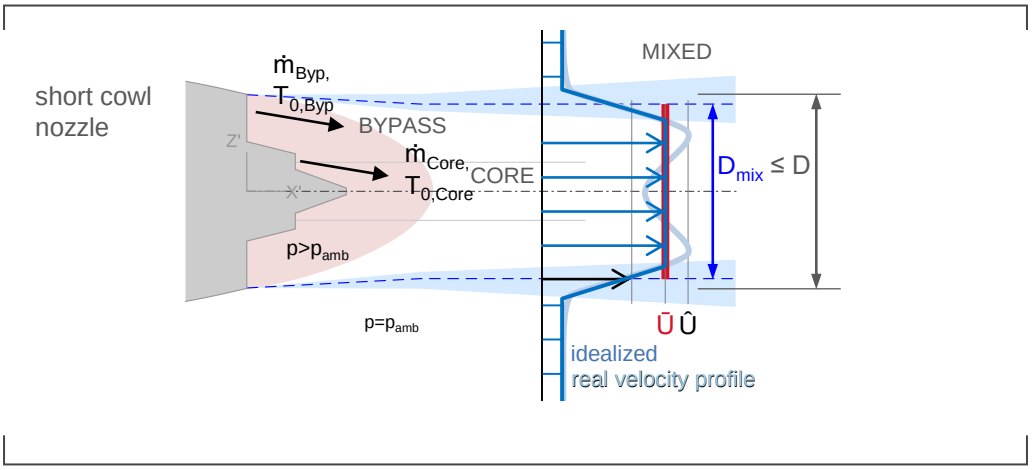

Figure A.1.: **Mixed jet mean flow properties**

jet ρ_{mix}. Some sources do not mention these equations. There may be manifold reasons for this: the mixing density might be measured, or the derivation left out for simplicity, or an assumption used for calculation.

Such an assumption could be the **isothermal jet** ($T_{Byp} = T_{Core} = T_{mix}$). This is a condition which is suggested e.g. in order to meet ISA-conditions. However, it also requires moderate heating ($< 90\,°C$) of the ducts - even for cold testing. The mixed jet area can be calculated considering bypass and core area as well as the velocity ratio:

$$\mu_A = \frac{A_{Byp}}{A_{Core}} \tag{A.8}$$

$$r_{U,ISL} = \frac{U_{Byp}}{U_{Core}} \tag{A.9}$$

$$\mu = \mu_A \cdot r_{U,ISL} \tag{A.10}$$

$$A_{mix} = \frac{\dot{m}_{Byp} + \dot{m}_{Core}}{\rho_{mix} U_{mix}} \tag{A.11}$$

$$A_{mix} = \frac{U_{Byp} A_{Byp} + U_{Core} A_{Core}}{\frac{\mu}{\mu+1} \cdot U_{Byp} + \frac{1}{\mu+1} \cdot U_{Core}} \tag{A.12}$$

$$A_{mix} = \frac{r_{U,ISL} A_{Byp} + A_{Core}}{\frac{\mu_A \cdot r_{U,ISL}}{\mu_A \cdot r_{U,ISL}+1} \cdot r_{U,ISL} + \frac{1}{\mu_A \cdot r_{U,ISL}+1}} \tag{A.13}$$

$$R_{mix} = \sqrt{\frac{A_{mix}}{\pi}} \tag{A.14}$$

The cold isothermal mixed jet diameter at norm conditions ($T_{ISA} = 15\,°C$) is displayed in figure A.2 for the LIST nozzle, a UHBR engine model with an area ration of $\mu_A \approx 8$. The investigated operations in AWB are all so-called "near unity velocity ratios". The near unity limits in the figure are the ones that Segalini [41] used for a nozzle of

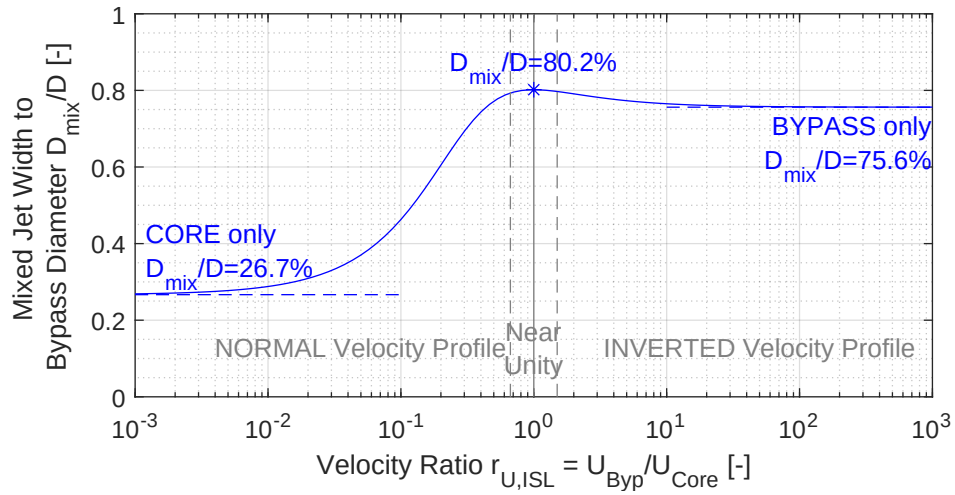

Figure A.2.: **Mixed jet diameter for various operations of LIST Nozzle**

smaller area ratio. Hence, the drawn limits are rather conservative. Note, that the while the jet width depends on the velocity ratio between bypass and core, it is approximately constant for near-unity velocity profiles.

B. Thin mixing layer model

B.1. Shear Layer convection functions

The shear layer convection parameter functions quantify the relative positioning (as shown in equation 3.4) around the mixed jet radius as well as the relative velocity (equation 3.3). The static jet properties $r_{U,OSL} = 0$ are well documented. However, there is only a few data points available for flight jets $r_{U,OSL} > 0$ which were used by the author [24] to close this scientific gap.
Future research or an aerodynamic measurement campaign could help improve the convection parameter functions or possibly help find a better approach.

The outer shear layer is characterized by an ideally infinite volume. The ambient flow cannot be classified by extensive flow properties - contrary to the calculation of the mixed jet where bypass and core mass flow rates are used. Therefore, another mechanism must be found to identify the velocity at the boundary between jet and ambient.

B.1.1. Option 1: mean total pressure determines centroid

The approach is to use a force-based postulation where it is assumed that the shear layer centroid is located at the mixed diameter position. If this is true, then the centroid velocity can be calculated by determining the mean of the total pressure. Since the static pressure is assumed to be constant (subsonic outlet condition), the mean of the dynamic pressures can also be chosen to calculate the centroid velocity.

$$\overline{p_{tot}} = 1/2 \cdot \left(p_{tot,jet} + p_{tot,\infty}\right) \tag{B.1}$$

$$\overline{\cancel{p_{stat}} + \Delta p} = 1/2 \cdot \left(\cancel{p_{stat,jet}} + \Delta p_{jet} + \cancel{p_{stat,\infty}} + \Delta p_{\infty}\right) \tag{B.2}$$

$$\overline{\Delta p} = 1/2 \cdot \left(\Delta p_{jet} + \Delta p_{\infty}\right) \tag{B.3}$$

In order to get a simple relation for the convection parameter, the assumption of constant density is made (subsonic). Using the formula for dynamic pressure,

$\Delta p = \rho/2 \cdot U^2$, and the velocity ratio, the centroid value can be determined.

$$U_{c,mp}^2 = 1/2 \cdot (U_{jet}^2 + U_\infty^2) \tag{B.4}$$

$$c_{U,mp} = \frac{U_{c,mp}}{U_{jet} + U_\infty} = \underbrace{c_0}_{\sqrt{2}/2} \frac{\sqrt{1 + r_{U,OSL}^2}}{1 + r_{U,OSL}} \tag{B.5}$$

$$c_{r,mp} = c_{U,mp} \cdot \frac{1 + r_{U,OSL}}{1 - r_{U,OSL}} - \frac{r_{U,OSL}}{1 - r_{U,OSL}} \tag{B.6}$$

This model suggested a static jet shear layer convection parameter of $c_0 = 70.7\,\%$. Bridges and Wernet [7] investigated among others the velocities along the nozzle lip line of a single stream jet. This is the position where the convection velocity is measured for single stream jets. They found that especially for low Mach number data (figure 17, bottom left), $c_0 \approx 0.7$ might be a suitable limit for the virtual shear origin. But, as the convection velocity decreases in streamwise direction, their convection parameter also decreases (to $c_0 \approx 0.67$, assuming $x/D_{mix} = 3$ where the flap TE might be located). Such a lower value around $c_0 \approx 0.64 \ldots 2/3$ is especially good for high Mach numbers (Bridges and Wernet [7], figure 19, bottom left). Thus, it comes with no surprise that factors around $c_0 \approx 0.65$ (Fuchs and Michel [16]) or $c_0 \approx 0.6$ (for a dimensional estimation, Miller [35] and Denisov [11] or as simulated result, Rego [37]) were reported.

B.1.2. Option 2: empirical function based on trapezoid centroid function

The reported factors around $c_0 \approx 2/3$ are very close to the centroid function of a trapezoid shear layer profile. However, velocity is not a conservation property. Therefore, the following function must be categorized as an empirical approximation rather than a physical function.

$$c_{r,id} = \underbrace{c_0}_{2/3} \cdot \frac{1 - r_{U,OSL}}{1 + r_{U,OSL}} + \frac{r_{U,OSL}}{1 + r_{U,OSL}} \tag{B.7}$$

$$c_{U,id} = c_{r,id} + (1 - 2 \cdot c_{r,id}) \cdot \frac{r_{U,OSL}}{1 + r_{U,OSL}} \tag{B.8}$$

B.2. Calibration of model

Note that the static jet shear layer convection parameter c_0 was written for reason of calibrating the function for static jets $r_{U,OSL} \to 0$. For unity velocity ratios $r_{U,OSL} \to 1$,

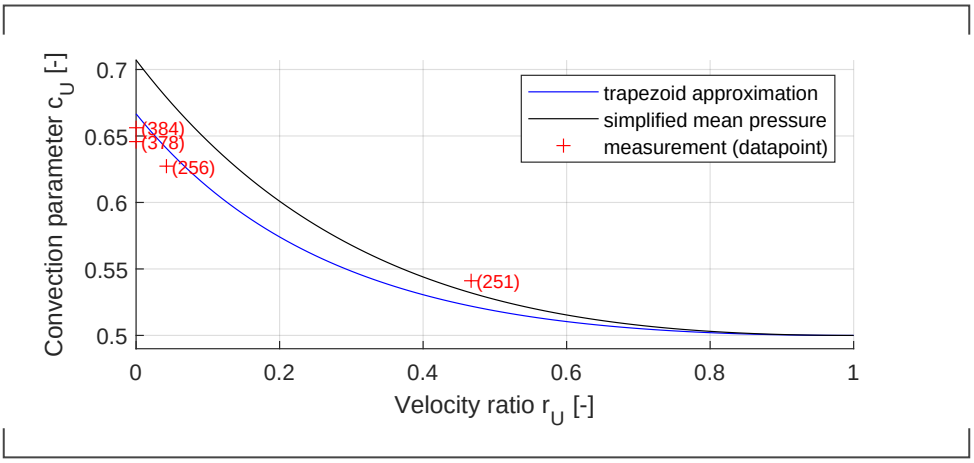

Figure B.1.: **Approximation for the convection parameter and experimental data, data published in [24]**

the calibration causes a "wake defect velocity" when calibrating option 1 and a perfect unity velocity or top hat profile when calibrating option 2. The wake defect effect is a physical reality, but may be here quantitatively incorrect. Depending on the measurement range, different calibration formulations may be better.

The uncalibrated convection parameter function for the relative velocity is displayed in figure B.1 and compared to own data. This data can be gathered by evaluating velocities at the mixed jet positions. A more elaborate and iterative process is to determine the velocity which encloses the theoretically correct mixed jet area at a plane normal to the jet axis. For the dissertation, the empirical approximation (option 2) which assumes a trapezoid velocity profile is chosen and calibrated. In the following example, the thin mixing layer model is calibrated for typical round jet features. It is assumed that (1) the shear layer of a static jet $r_{U,OSL} = 0$ spreads at an angle of $\alpha_o = 7\,^\circ$. The shear layer convection parameter c_0 remains unknown at this point. Equation 3.8 is used to calculate σ_0.

$$\text{Ansatz: eq. 3.8: } \tan(\alpha_o) = \frac{H_{osl,o} - R_{mix}}{L - x_0} = c_0 \cdot \frac{\sqrt{\pi}}{\sigma_0} \tag{B.9}$$

$$\sigma_0 = \frac{\sqrt{\pi} r_c}{\tan(\alpha_o)} \tag{B.10}$$

Furthermore, it is assumed (2) that the jet core length (position $H_{osl,i} = 0$) of a static jet $r_{U,OSL} = 0$ is 7 mixed jet diameters, i.e. 14 mixed jet radii $L_{pot}/R_{mix} = 14$. With

the help of equations 3.7 and 3.1, the following correlation can be derived:

$$\frac{H_{osl,i}}{R_{mix}} = 1 - (1 - c_0) \cdot \frac{\sqrt{\pi}}{\sigma_0} \frac{x_{pot} - x_0}{R_{mix}} \tag{B.11}$$

$$\sigma_0 = (1 - r_c)\sqrt{\pi} \cdot 2\frac{L_{pot}}{D_{mix}} \tag{B.12}$$

Those two conditions can be combined to calculate the shear layer convection parameter.

$$c_0 = \left(1 + \frac{1}{\tan(\alpha_0) \cdot 2\frac{L_{pot}}{D_{mix}}}\right)^{-1} \tag{B.13}$$

$$c_0 = \left(1 + \frac{1}{\tan(7\,^\circ) \cdot 14}\right)^{-1} \approx 0.6322 \tag{B.14}$$

$$\sigma_0 = \frac{\sqrt{\pi}}{\left(2\frac{L_{pot}}{D_{mix}}\right)^{-1} + \tan(\alpha_o)} \approx 9.13 \tag{B.15}$$

This calculated value is close to the reported value of Eisfeld for planar shear layers ($\sigma_0 \approx 11$). There are other options to calibrate the model, as long as two of the three parameters (potential core length, jet shear layer spreading angle, shear layer convection parameter) are selected (see figure B.2).

B.3. Virtual shear layer origin

The virtual shear layer origin is determined using measurement data (see figure B.3). It depends on a number of parameters, e.g. engine type, nozzle TE thickness, boundary layer thickness (in the duct as well as externally), and engine operations. Even though the value may not be entirely constant, an averaged estimation is a great improvement compared to using $x_0 = 0$: Let's assume the engine in figure B.3 is installed to a wing at $L/D_{mix} \geq 2.5$. Then, the length estimation $(L - x_0)$ produces an error of $\geq -10\,\%$ when using $x_0 = 0$.

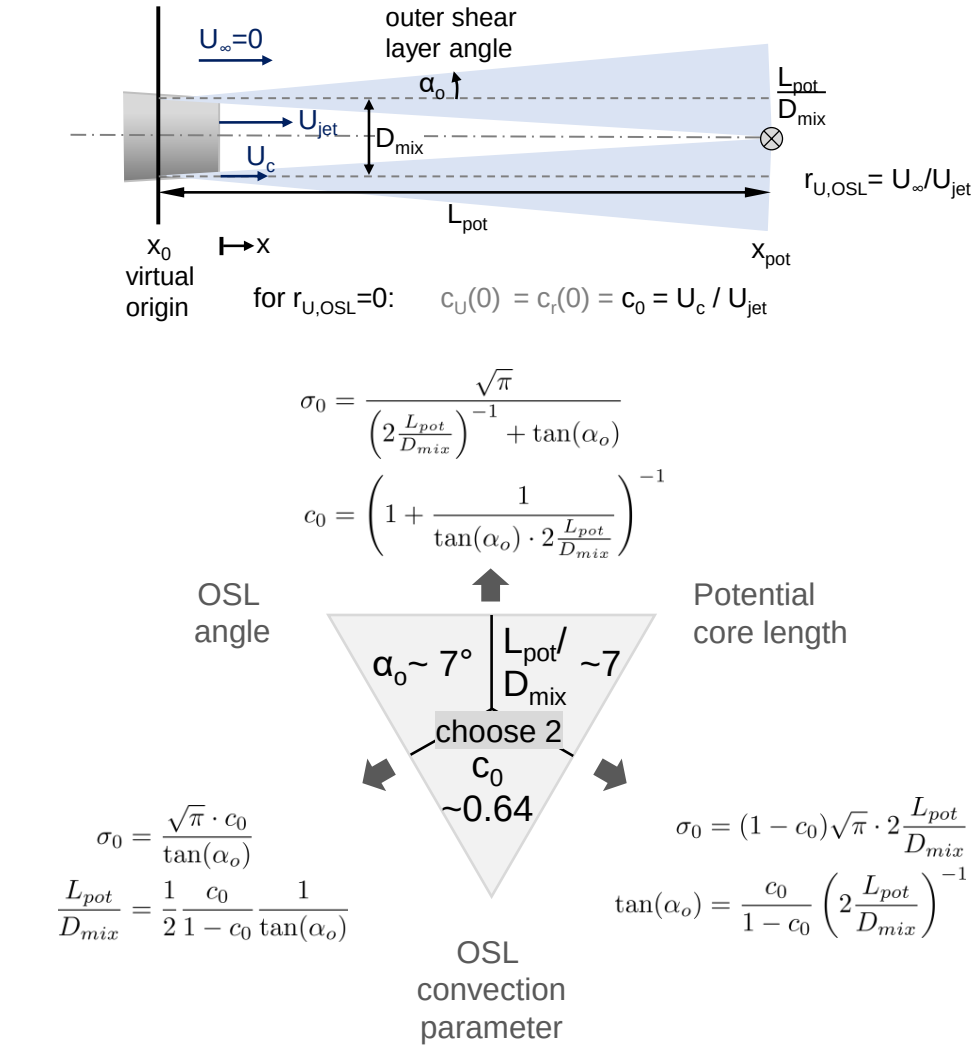

Figure B.2.: **Calibration of thin mixing layer model using static jet properties**

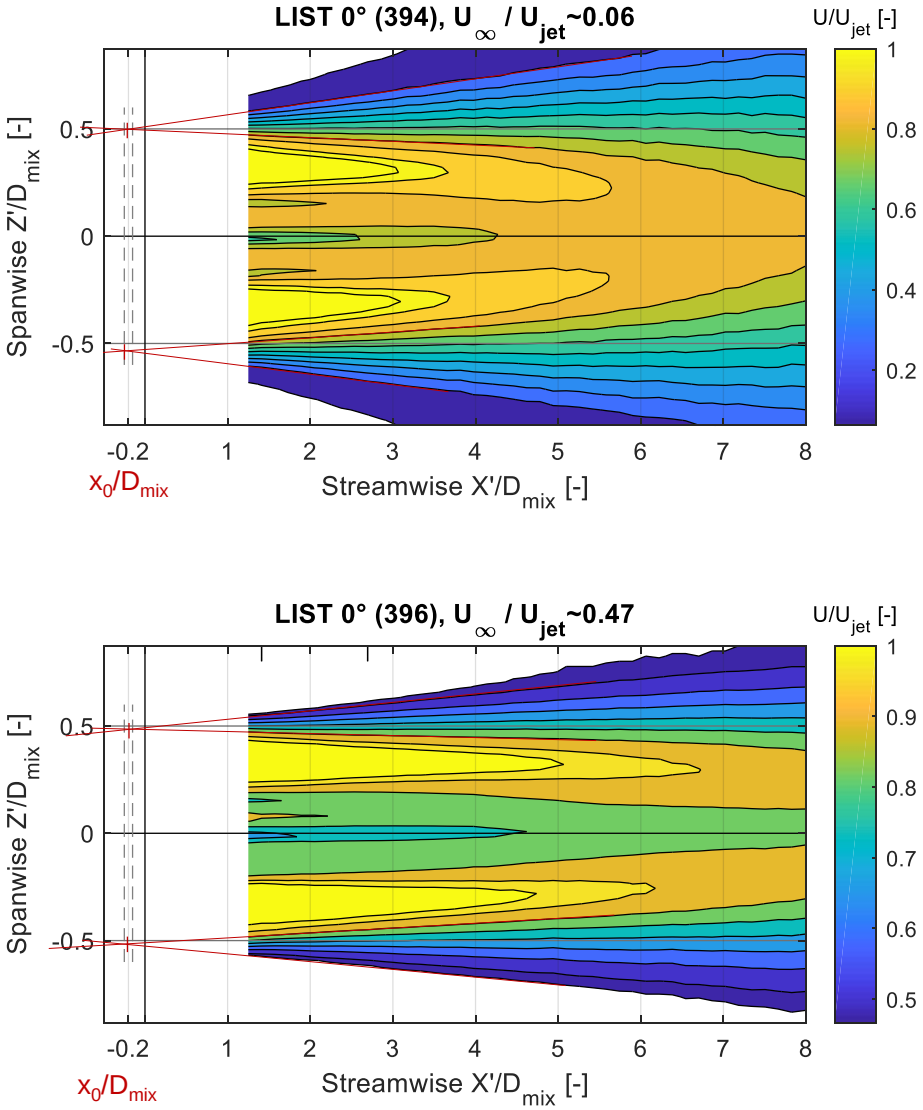

The virtual shear layer origin $x_0 < 0$ depends on engine type, nozzle TE thickness, boundary layer thickness, operational setting $r_{U,OSL}$

Figure B.3.: **Determination of the virtual shear layer origin**

C. Far-field microphone measurements and corrections

Depending on the measurement campaign, 8 to 10 Brüel&Kjær BK4136 1/4" condenser microphones were aligned underneath the wing ($\psi = 0\,°$). This allows to study the directivity in a polar angle of $\theta = 71 \ldots 135\,°$ (relative to engine BOC).

The measured data (or online data) of the far-field microphones must be corrected as it does not represent the true noise sources. The following corrections should be made (order as listed):

1. energetic subtraction of background noise from measured signal (given a sufficient signal to noise ratio)

2. correction of shear layer refraction and wave convection caused by wind tunnel stream

3. correction of microphone free field characteristics

4. correction of atmospheric damping

5. correction of convective amplification

The final step is the projection of the data onto a constant distance to the source, here $R = 1\,\mathrm{m}$. In the following subsections, the applied correction methods are described. Detailed descriptions can be found in the cited references.

C.1. Background noise correction

The side condition for background correction is a sufficient (measured) signal to noise ratio. Corrections can be made with the help of energetic subtraction of the noise

SPL_{BGN} from the signal SPL_{meas} (equation C.1) for each frequency. It is common practice to define a correction limit (see criterion C1 and C2 in section E.0.1).

$$SPL_{corr} = 10\log_{10}\left(10^{SPL_{meas}/10} - 10^{SPL_{BGN}/10}\right) \text{ if } SPL_{meas} - SPL_{BGN} > \text{criterion} \tag{C.1}$$

C.2. Shear layer refraction

Sound waves refract and disperse when passing a wind tunnel shear layer. The refraction causes a change in directivity whereas the dispersion causes an amplitude decrease of the signal. On top of those effects, the wind tunnel stream influences the wave propagation, since the sound waves convect in streamwise direction. This effect influences directivity as well as amplitude. Amiet [1] suggested a method for correcting the three effects. One of Amiet's assumption is the refraction of sound waves at an infinitesimally small shear layer positioned in a distance h to the source $\vec{S}_{geo}$. The correction depends on the position of the noise source $\vec{S}_{geo}$, the observer (mic) $\vec{M}$ as well as the flow Mach number M_∞ (figure C.1).

The definition (figure C.1) of the two angles, θ and φ_x, are complimentary. θ is the definition used by Amiet, however, as th AWB evaluation uses the polar angle φ_x, the angles can be transformed using equation C.2 to C.4:

$$\theta = 180^\circ - \varphi_x \tag{C.2}$$
$$\theta' = 180^\circ - \varphi' \tag{C.3}$$
$$\theta_M = 180^\circ - \varphi_M \tag{C.4}$$

The corrected angle θ' is defined for a flow without the presence of a shear layer between source and observer. According to Amiet, it must be determined in an iterative process, using equations C.5 to C.7:

$$\tan(\theta_M) = \frac{\tan(\theta') \cdot \tan(\theta)}{\left(\frac{h}{Y}\right) \cdot \tan(\theta) + \left(1 - \frac{h}{Y}\right) \cdot \tan(\theta')} \tag{C.5}$$
$$\tan\left(\theta'\right) = \frac{\xi}{(1 - M_\infty^2) \cdot \cos(\theta) + M_\infty} \tag{C.6}$$
$$\xi = \sqrt{\left[1 - M_\infty \cdot \cos(\theta)\right]^2 - \cos^2(\theta)} \tag{C.7}$$

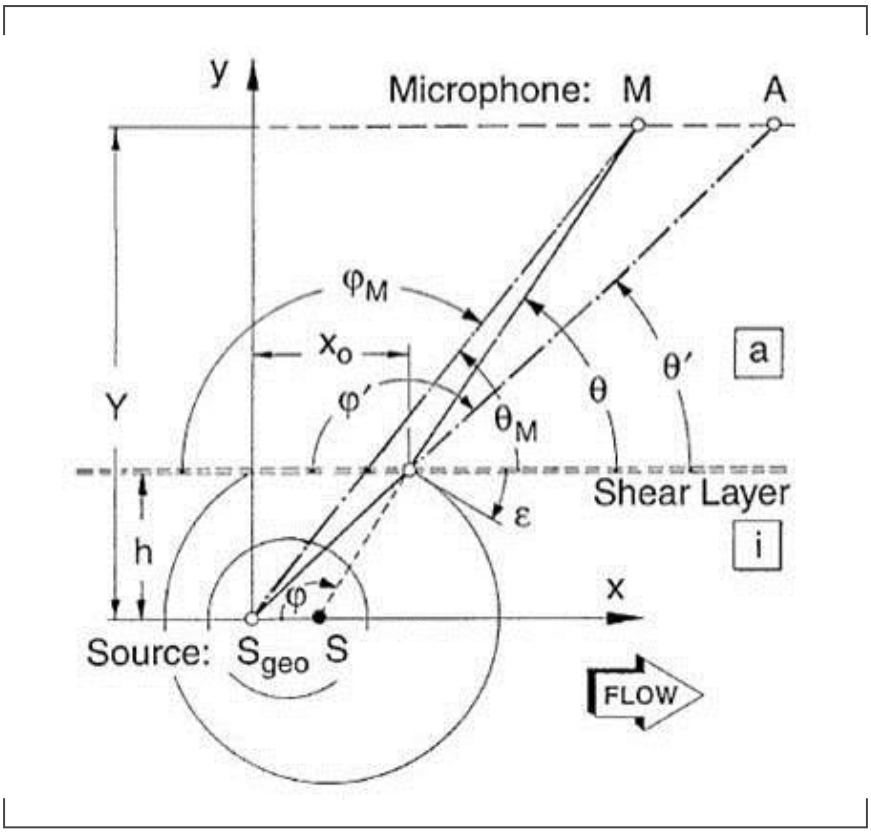

Figure C.1.: **Shear layer refraction for a planar shear layer. Image:[13]**

The sound pressure is calculated according to equation C.8:

$$\frac{P_A}{P_M} = \frac{h/Y}{2 \cdot \xi \cdot \sin^2(\theta)} \cdot \left[\xi + \sin(\theta) \cdot (1 - M_\infty \cdot \cos(\theta))^2\right] \ldots \\ \ldots \cdot \sqrt{\left[\sin(\theta) + \xi\left(\frac{Y}{h} - 1\right)\right] \cdot \left[\sin^3(\theta) + \xi^3 \cdot \left(\frac{Y}{h} - 1\right)\right]} \tag{C.8}$$

The corrected direction of the noise source ϵ can be calculated considering the change of the source position from S_{geo} to S:

$$\epsilon = \alpha \cdot \sin\left[\frac{1}{1 + \tan^2(\theta')} \cdot \left(-M_\infty \cdot \tan^2(\theta') + \operatorname{sgn}[\tan(\theta)] \cdot \sqrt{1 + (1 - M_\infty^2) \cdot \tan^2(\theta')}\right)\right] \tag{C.9}$$

The corrected angle ϵ can be transformed into the φ_x definition using equation C.10:

$$\varphi_x = 90^\circ - \epsilon \tag{C.10}$$

The shear layer correction assumes the source as a point source from which the signal propagates. For this project, this reference point was assumed at the engine as well as the flap trailing edge.

C.3. Microphone directivity

The microphone manufacturer provides microphone characteristics for the microphones (see figure C.2). The amplitudes are corrected depending on the incidence angle of a sound ray propagating towards the Brüel&Kjær microphone.

C.4. Correction of atmospheric damping

In order to make measurement data comparable, the signal will be projected to the same distance, e.g. $R = 1\,\mathrm{m}$. Especially for large facilities, overflight experiments or cross-comparison, this correction is crucial. The chosen value for the distance must be larger than the noise source. The processing suggested by Sutherland [3] corrects the atmospheric influences to sound propagation along the projected distance.

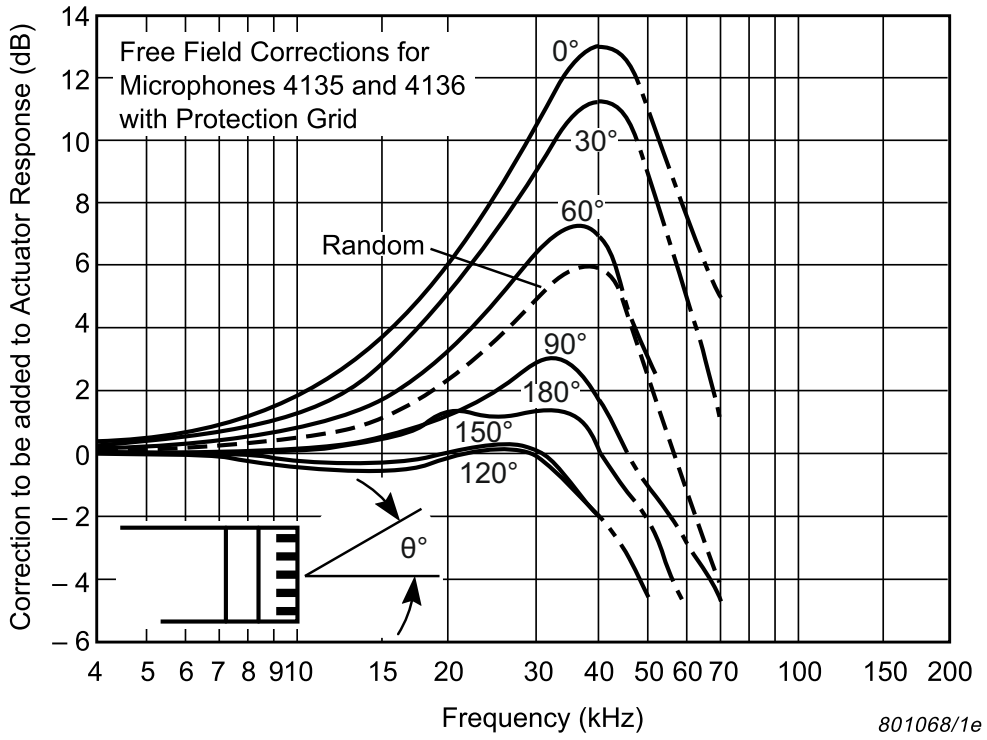

Figure C.2.: **Microphone free field corrections (Brüel&Kjær [9])**

C.5. Convective amplification

The directivity of a moving acoustic source differs from a source at rest. This is also valid for a noise source which is situated in a wind tunnel environment where the fluid is in motion. The differences in directivity is caused by convective amplification which either increases or reduces the signal. The pressure change can be calculated using equation C.11.

$$\frac{\tilde{p}}{\tilde{p}_{M=0}} = \frac{1}{(1 - M_\infty \cos(\varphi_x))^n} \tag{C.11}$$

$$n = \begin{cases} 2 & \text{monopole or dipole} \\ 3 & \text{quadrupole source} \end{cases} \tag{C.12}$$

$\tilde{p}_{M=0}$ is the RMS-value of the sound pressure for a source at rest and φ_x is the true directivity characterizing angle. Upstream noise sources will be amplified whereas downstream sources will be reduced. The exponent n in equation C.11 depends on the type of noise source: $n = 2$ for monopoles and dipoles, $n = 3$ for quadrupoles.

C.6. Geometric damping

The final amplitudes are normalized to a constant propagation radius of $R = 1\,\mathrm{m}$. This distance is the same distance mentioned in section C.4. The amplitude is corrected according to equation C.13:

$$SPL_{ref} = L + 20 \cdot \lg\left(\frac{R}{R_{ref}}\right) \tag{C.13}$$

D. The perfect wing model for good JFI noise measurement

D.0.1. The F16 wing model

The ideal high-lift wing model for the measurement of jet-flap interaction should produce no extra noise due to unwanted interaction between engine, slat and pylon. The insights from a KonTeKst test campaign [8] showed that it is good to use a 2D-extruded model wing with a straight slat cutout and without any pylon. The engine yaw angle should be zero degrees in order to avoid 3D effects. For the best comparisons, the slat geometrical settings (deflection angle, gap, overlap) are fixed.

The DLR-F16 model fulfills these criteria while also representing a wing section of a short range aircraft. In order to avoid a pylon, the wing is mounted wall-to-wall on circular turning plates. The turning plates are mounted in side plates, which serve as an extension of the wind tunnel nozzle and set the yaw angle to zero (see noise contribution of side plates in figure 4.2).

The wing is geometrically characterized by a reference chord length of $c = 300\,\mathrm{mm}$ and a span center part of $b = 800\,\mathrm{mm}$, which amounts to a reference area of $A_{ref} = 0.24\,\mathrm{m}^2$ as well as an aspect ratio of $\Lambda = 2.67$.

A characteristic aerodynamic flow feature is the boundary layers around the wing. The laminar-turbulent transitions within such a boundary layer do not scale with a geometric scaling factor. In the worst case, the wing boundary layers may be fully laminar, thereby producing less or unrepresentative turbulent structures. With some knowledge about the transition points, the wing can be tripped at the correct position which forces a transition from the laminar to a turbulent boundary layer.

However, there are operational states where scale-related acoustic phenomena appear at the model which are typically not a part of the full-scale wing. This concerns Rossiter-like tones [50] at frequencies of $1 \ldots 2\,\mathrm{kHz}$ in the model size

DLR - F16 modification for testing JFI Noise at high engine-integrations

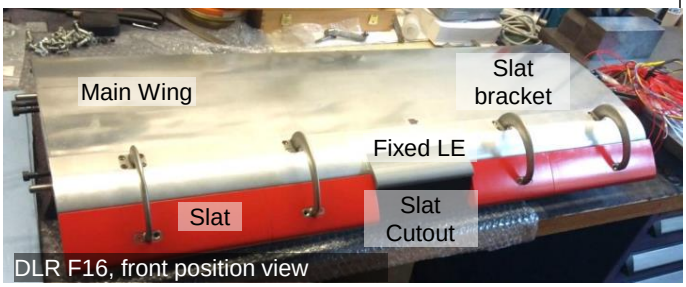

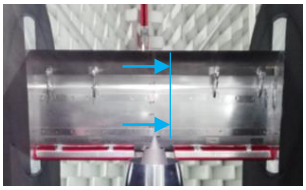

Treatment of unwanted noise

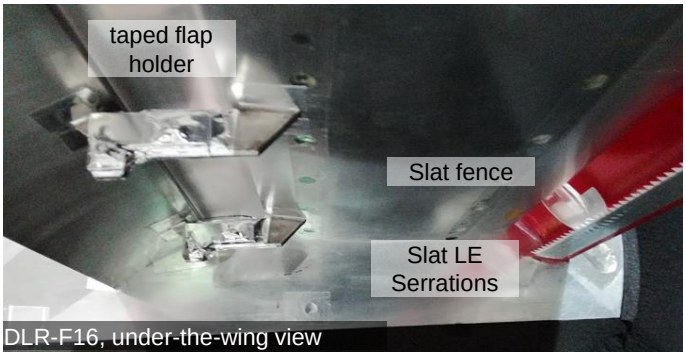

Figure D.1.: **DLR-F16 wing, modified for JFI testing**

spectrum. They can be reduced by limiting the slat cove source length by fencing[1]. The chances of very good reproducibility of signal in this frequency region is rather low. The typical target is to try to reduce the tones as best as possible.

In order to aerodynamically measure an angle of attack of $AoA = 6\,^\circ$ for the high-lift-system, CFD-simulations showed that the geometric angle needs to be adjusted to $\alpha = 14.5\,^\circ$. At this angle, the surge lines to the engine inlet align with fixed walls. Therefore, the wing as well as the engine are declined by $\alpha = 14.5\,^\circ$.

The F16 is a three-element wing with slat, main body, and flap. The slat is mounted to the main wing via 4 aerodynamically shaped over-the-wing slat brackets. The slat angle is fixed to $27.8\,^\circ$ for the entire test campaign. Around the nozzle area the slat is symmetrically cut out over a span width of $b_{cut} = 141$ mm and replaced by a clean chord leading-edge insert which is mounted to the main wing section.

The flap is fixed to the main wing via brackets, which are installed under the wing. The brackets allow for continuous adjustment of gap, overlap, and flap deflection angle.

[1] This measure is controversially discussed, especially w.r.t. representative aerodynamics.

The very tight fit of the engine underneath a wing causes space conflicts as long as the 2D slat profile is fully extruded along the entire span width. This geometrical challenge is not new, and has been solved by a local cutout of the slat and a replacement of the main wing contour by the clean chord slat contour (see figure D.1).

All in all, the high-lift wing settings of the experimental setup have been designed to maximize the measurement quality of jet-flap interaction with the least impact on other potential engine integration effects.

D.0.2. Method to prove that engine integration related noise is jet-flap interaction noise

Let us imagine that all conditions are good and it is possible to isolate the noise which stems from under-the-wing engine integration - how is it possible to prove that this noise is jet-flap interaction noise and does not stem from other engine integration related noise sources (e.g. from the slat-engine region)?

A method for this evaluation has been suggested by Pott-Pollenske and was evaluated and presented by Jente et al. [25]. It is here described using some images from that paper.

With the help of source location measurements (see figure D.2) and a beamforming algorithm, the noise source region which is located near the engine and the slat can be spatially isolated and a spectrum can be generated specifically for this spatial source region (SR). The region has been called *other SR* because it contains a mix of noise sources, among others nozzle exit noise (see figure 3.6), as well as slat & slat related noise.

As the goal is to show that the main effects are related to changes in the flap SR and not in the other SR, two equally sized regions as well as the combined/full region are defined. The quality of this separation technique can be determined by comparing the full region signal against the energetic sum of the two source regions. It can be shown that the signal is very similar for third-octave band frequencies $f_m \geq 2\,\mathrm{kHz}$. This means that the full scale relevant frequency range can be evaluated.

Unfortunately, the mix of noise sources limits the possibilities for the evaluation: The presence of an engine noise source (i.e. NEN) does only allow the comparison between data points with the same operational settings.

- Engine integration noise sources can be spatially divided into two regions
  - other source region: engine-pylon-slat
  - flap source region: jet-flap interaction
- They can be detected using microphone source location measurements and beamforming.
- The method of **spatial signal separation** and comparison (suggested by Pott-Pollenske) can be used to study JFI-relevant high frequencies

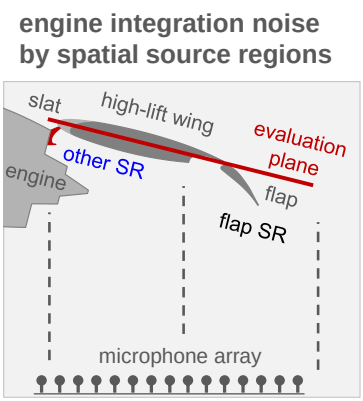

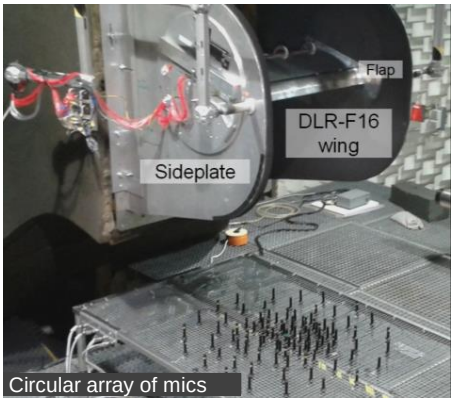

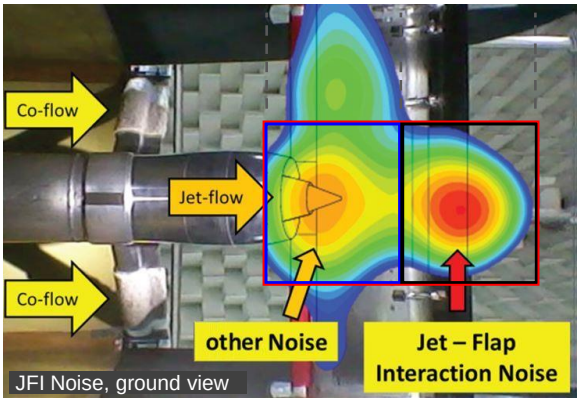

Limit 1: Method
Low frequency signals stretch into both SR, a **spatial separation does only work for higher frequencies**.

Limit 2: Physics
There is a physical limit due to the size and design of the measurement system.

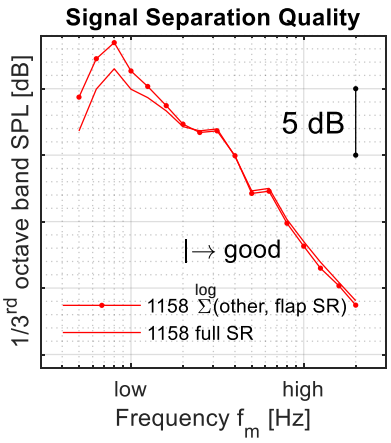

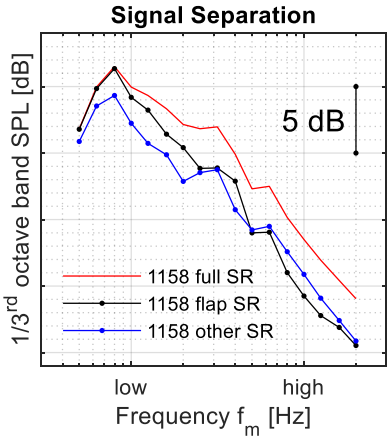

Figure D.2.: **Source location method to determine JFI noise, adapted from [25]**

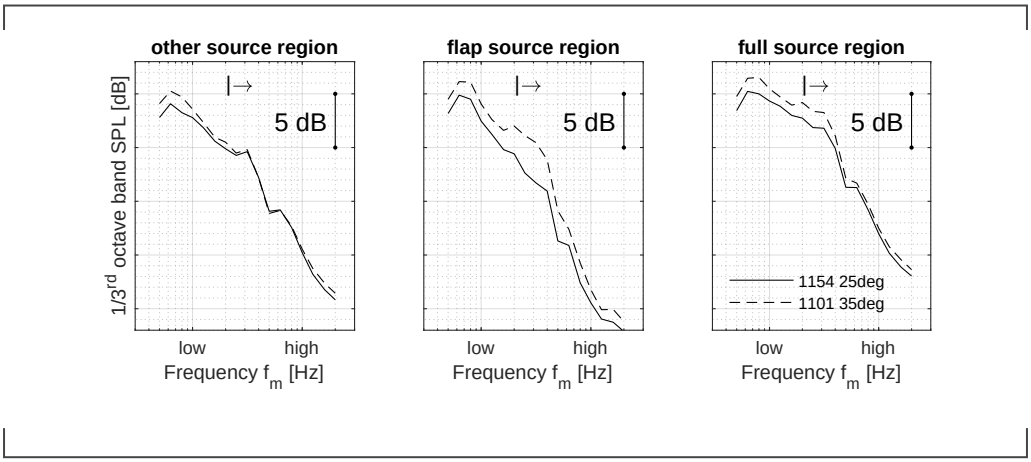

Figure D.3.: **Study of flap deflection angle using spatial source analysis Build: ENG=APP, WT=60 m/s, Wing=Ref**

Flap parameters For the same engine integration parameters (height, length, yaw, and pitch) the same sound pressure levels are expected in the other SR. This means that especially the geometrical flap parameters (gap, overlap, deflection angle) can be studied very well. For example, the change of the flap deflection angle is examined (see figure D.3). The signal in the other SR does not change for the high frequency range.

Engine integration parameters The study of engine integration parameters (height, length, yaw and pitch) is not as trivial as the study of flap parameters. There is an ambiguity problem in the other source region for direct comparison (see appendix F) of engine integration parameter changes. The reason is that the build change affects multiple noise sources at the same time. A good and simple method is to compare the other SR for isolated and integrated wing builds with the 'engine off' condition (see figure D.4). This helps to identify engine integration effects and supports decision making for a design change of the slat cutout.

If flap noise is negligible compared to the noise sources near the slat, it is also possible to compare far-field microphone data of the isolated and the integrated wing (see figure E.7). The microphone data should be corrected w.r.t. a slat geometry feature, e.g. the clean chord wing leading edge (WLE) as MRP.

Even without the ability to name the exact causes for changes in the other SR, it can be shown that the effects in the other SR are small compared to the effects in the flap SR (figure D.5).

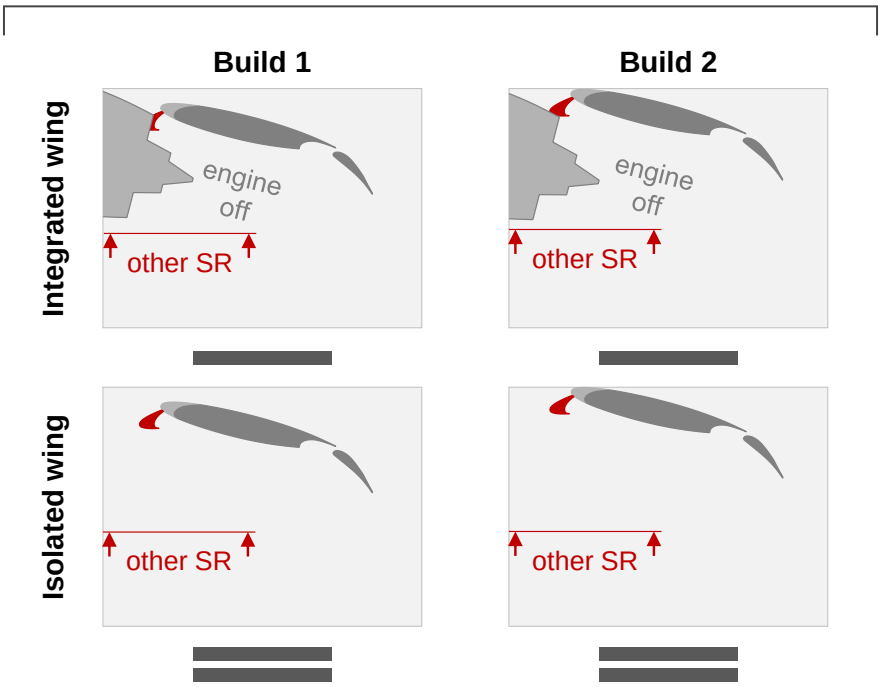

Engine integration effect 1 **Engine integration effect 2**

- If zero/negligible: good
- If not negligible: compare to engine int. effect of build 2
  - If similar: good
  - If different: engine wing integration effect, check dimension of signal against flap SR
    - If small compared to flap SR (JFI): good
    - Otherwise: engine integration is important

Figure D.4.: **Spatial source evaluation method using beamforming method to find slat design related engine integration noise sources**

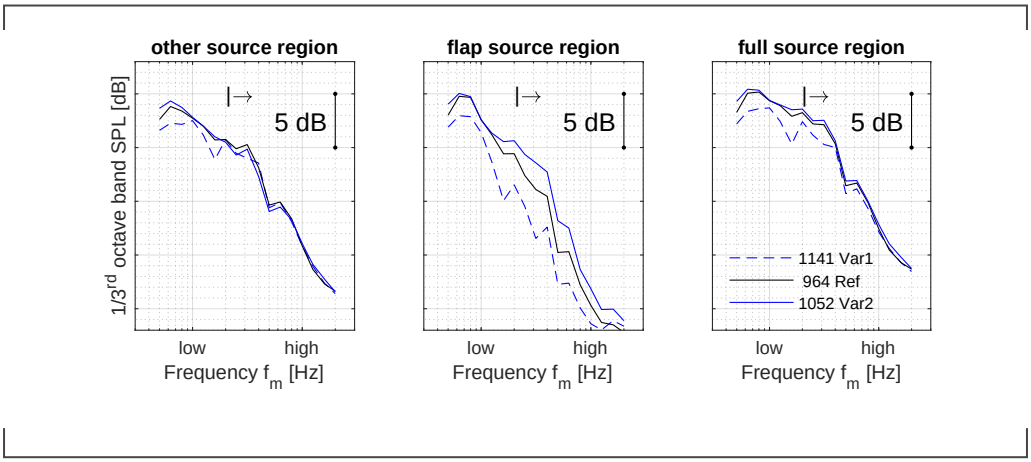

Figure D.5.: **Flight jet APP60 at different heights**

Conclusion The spatial source separation method shows that the acoustical engine integration effects are fully or almost completely related to jet-flap interaction noise. The method is especially good for acquiring proof for trivial cases where the other SR is the same by build and operational condition (e.g. flap parameter study). However, the evaluation is limited to the high frequency range due to the physical limits of the measurement apparatus.

The comparison of isolated and integrated wing (engine off) has been suggested in order to check whether the design of the cutout slat and the engine integration in this region is well-suited for the evaluation of jet-flap interaction.

E. Isolated comparison of wanted noise sources against unwanted noise sources

In this section, the acoustic tests of the isolated jet and the isolated high-lift wing are studied. The focus is set on finding any operational limits and on assuring good quality of the data points by assigning limits for unwanted background noise sources. This will be achieved by identifying minimum signal to noise ratio criteria (section E.0.1). The limits for correcting isolated jet noise are detected with this tool (in section E.0.2). The same method is also used for checking the correction of isolated high-lift wing noise (section E.0.2).

E.0.1. Correction of background noise

Even the best set up wind tunnel experiment is subject to unwanted noise sources. Hence, for every measured signal data point a background noise measurement must be conducted. The background noise is energetically subtracted from the measured signal. As a result, there is a corrected signal which can be used in the evaluation process (see figure E.1).

Note that there are four important ratios of noise to measured signal (compare table E.1): 0dB (mathematical limit for the use of real number range), -3dB (noise equals corrected signal), -6dB (industry criterion) and -10dB (corrections dimensionally negligible). Thus, there are the following background noise correction ranges:

- $>$ 0dB. The correction is only possible in complex numbers.
- $<$ 0 . . . $-$ 3dB. The background noise is higher than or equal to the corrected signal. Corrections to the signal are mathematically possible in real numbers, but they can be high in amount. If a background noise source is very large, then the background correction is not very good. However, an alternative is to accept the large noise source as a part of the signal mix and to choose

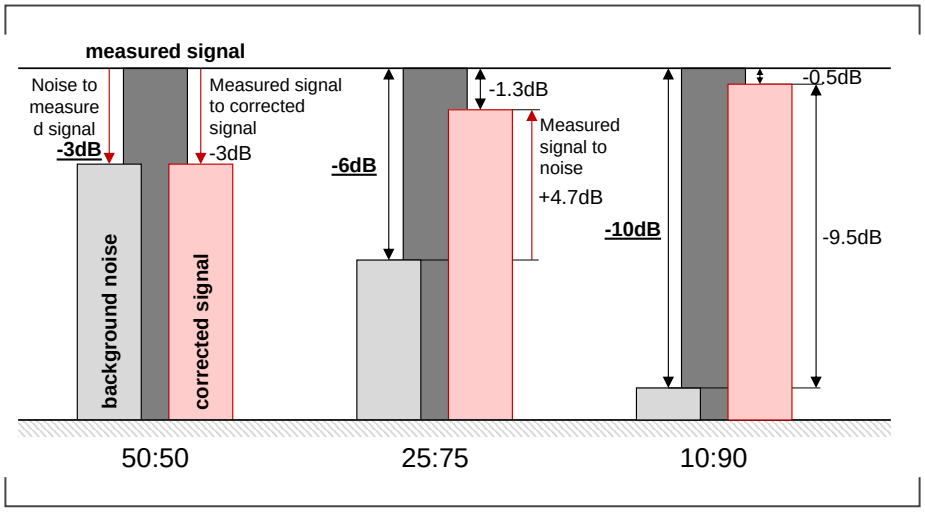

Figure E.1.: **Noise to measured signal ratio for background noise correction**

a different evaluation method. Another option is to evaluate whether the frequency band is essential to the evaluations. If yes, the experiment might need to be redesigned.

- $-3 \ldots -6$dB. The corrected signal is equal or up to three times higher than the noise. In logarithmic terms, this means that 3 to 1.7 dB are subtracted from the measured signal in order to account for the background noise.

- $-6 \ldots -10$dB. The corrected signal is three to nine times higher than the noise. In logarithmic terms, this means that 1.7 to 0.5 dB are subtracted from the measured signal in order to account for the background noise.

- -10dB. The signal is 9 times higher than the noise. This is a significant amount. The correction of 0.5 dB might be counted as dimensionally negligible.

Table E.1.: **Influence of background noise to measured signal on corrected signal**

Noise to Signal measured	**Signal corrected to Signal measured**	**Signal corrected to Noise** [linear]	[logarithmic]
[±0 dB]	$-\infty$	0 % : 100 % = 0	$-\infty$
−1 dB	−6.9 dB	21 % : 79 % = 0.3	(−5.9 dB)
−2 dB	−4.3 dB	37 % : 63 % = 0.6	(−2.3 dB)
[−3 dB]	−3.0 dB	50 % : 50 % = 1.0	(0 dB)
−4 dB	−2.2 dB	60 % : 40 % = 1.5	(+1.8 dB)
−5 dB	−1.7 dB	68 % : 32 % = 2.2	(+3.3 dB)
[−6 dB]	−1.3 dB	75 % : 25 % = 3.0	(+4.7 dB)
−7 dB	−1.0 dB	80 % : 20 % = 4.0	(+6.0 dB)
−8 dB	−0.7 dB	84 % : 16 % = 5.3	(+7.3 dB)
−9 dB	−0.6 dB	87 % : 13 % = 6.9	(+8.4 dB)
[−10 dB]	−0.5 dB	90 % : 10 % = 9.0	(+9.5 dB)

Let us think about the narrowband spectra of a measured signal and the corresponding background noise (see grey curves in figure E.2). These spectra are supposedly not extremely smooth: single values fluctuate around a mean curve which could be extracted by filtering. A very simple filtering mechanism is to discretize the spectrum according to the spacing of the third-octave band (red horizontal lines in figure E.2).

$$\text{third-octave band center freq.: } f_{m,i} = 1\,\text{kHz} \cdot 2^{(i/3)} \text{ , for } i = -5 \ldots 16 \tag{E.1}$$

$$\text{upper passband freq.: } f_{u,i} = f_{m,i} \cdot 2^{(i/3)} \tag{E.2}$$

$$\text{lower passband freq.: } f_{l,i} = f_{m,i} / 2^{(i/3)} \tag{E.3}$$

For each of those third-octave band sections, the mean can be calculated.[1] So, the first evaluation is to subtract the background noise mean from the measured signal mean (by third-octave band section) and identify the minimum. This value (A) is some representation for the minimum (averaged) measured signal to noise ratio.

$$\text{passband mean SPL: } A_i = \text{mean}\left[SPL_{jet}(f)\right]_{f_{l,i}}^{f_{u,i}} - \text{mean}\left[SPL_{bgn}(f)\right]_{f_{l,i}}^{f_{u,i}} \tag{E.4}$$

$$\text{overall passband mean SPL: } A = \min(A_i) \tag{E.5}$$

[1] This is a good idea for a simple analysis and can certainly be improved. The conversation from narrowband to third-octave band is more sophisticated. It involves signal filtering techniques where filter windows (e.g. Hanning window) and possibly an overlap of those windows (e.g. 50 %) are defined.

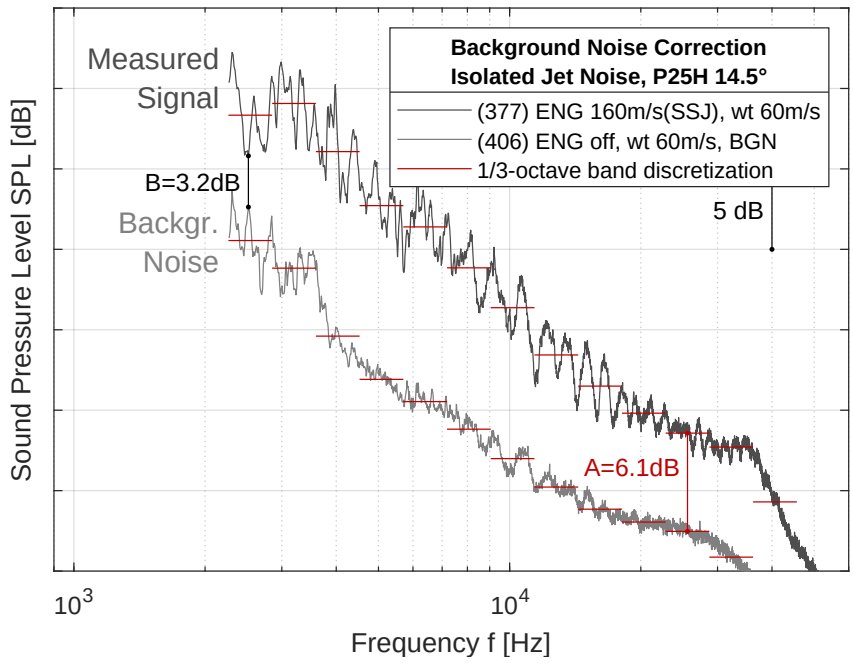

Figure E.2.: **Measured signal and background noise**

However, as an evaluation about the fluctuations in the spectrum is needed, the second assessment is to identify the minimum (value B) between the measured signal and the background noise (without any discretization).

$$\text{narrowband } \Delta\text{SPL: } B_i = \left[SPL_{jet}(f) - SPL_{bgn}(f)\right] \tag{E.6}$$

$$\text{narrowband min. } \Delta\text{SPL: } B = \min(B_i) \tag{E.7}$$

The two values (A and B) can be combined to criteria C1 and C2:

C1. A convenient criterion is when value $A = 6\,\text{dB}$ and value $B \geq 3\,\text{dB}$. This means that the averaged corrected signal to noise ratio is 75% to 25% noise in the discretized third octave bands. Individual narrowband frequencies may be lower than that ratio, but at worst this is 50% (corrected) signal to 50% noise. For rather smooth spectra where $A \geq 6\,\text{dB}$, it was often also observed[2]

[2]This is, however, by no means a rule. A tone at a single narrowband frequency of the background noise can decimate the correction of an otherwise good measurement below the accepted correction criteria.

that $B \geq 3\,\mathrm{dB}$. Note that C1 is a less strict criterion than the industry criterion, $B \geq 6\,\mathrm{dB}$.

C2. The lowest acceptance limit for any noise measured should be $A = 3\,\mathrm{dB}$ (corrected signal equals noise in the worst case frequency band) and $B > 0\,\mathrm{dB}$ (correction mathematical possible in real numbers).

In the following sections, this method will be used in order to derive the limits for background noise correction of isolated engine noise (section E.0.2) and isolated high-lift wing noise (section E.0.3).

E.0.2. Isolated engine noise

The measured signal to uncorrected background noise has been studied for Power25 (large engine) data points and the frequencies which are relevant to studying the relevant full scale signal range (figure E.3). The methods and criteria from section E.0.1 have been applied.

A rather interesting question of detail concerns the operational setting for the background noise. There are two candidates: the 'engine off' condition as well as 'matched jets'. However, both of the signals are very similar (see appendix I.2), because the engine holder noise is a strong source. Therefore, the cost-efficient 'engine off' operation has been used for all data points.

The final results are shown in a contour plot (figure E.3) where only the minimum of the averaged passband deltas of $A = 6\,\mathrm{dB}$ (criterion C1) and $A = 3\,\mathrm{dB}$ (criterion C2) are displayed. The curves are (here) 2D-interpolated from the data set. It turns out that the curves are linear because only a 4x2 data point set was available for evaluation.

For the tested field of velocities there is a good measured signal to background noise ratio until velocity ratios of $r_{U,OSL} \approx 0.38$. Beyond velocity ratios of $r_{U,OSL} \approx 0.46$ the noise is too high for the background noise correction.
Note, that sometimes the difference velocity ΔU is also used to derive some rules of thumb for a background noise criterion. Neither difference velocity nor velocity ratio resemble the correct background noise correction criterion very well on their own. Yet, velocity ratios are the better estimation for the chosen parameter field. This is indicated by the isolines of $3\,\mathrm{dB}$ and $6\,\mathrm{dB}$ in figure E.4 which are rather vertical than horizontal.

The results in figures E.3 and E.4 are part of an even larger assessment for different

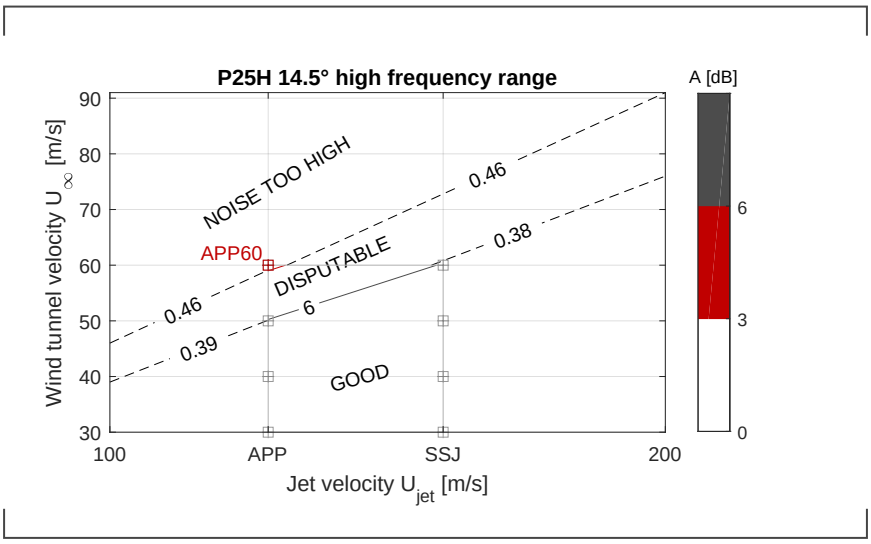

Figure E.3.: **Isolated jet background noise**

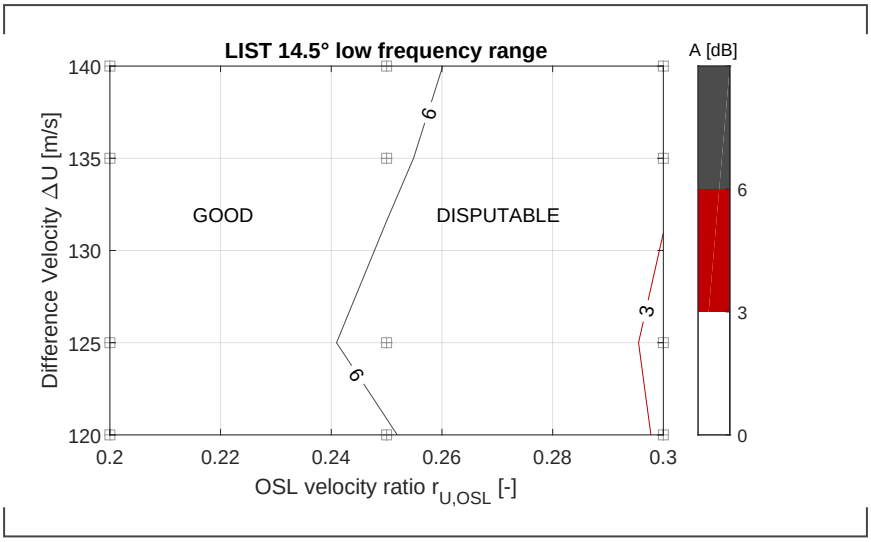

Figure E.4.: **Dependency of background noise correction criteria on jet parameters**

engine types and frequency ranges. The critical velocity ratios, are displayed in table E.2. They are here merely conservatively approximated, and serve as crucial side-conditions for the jet-flap interaction noise measurement diagram.

Table E.2.: **Background noise correction limits for isolated jet noise**

		GOOD		**TOO NOISY**	
		$r_{U,OSL} < \ldots$		$r_{U,OSL} > \ldots$	
frequency range	$f_{1/3,m}$ [Hz]	P25H	LIST	P25H	LIST
low	315 . . . 630 Hz	0.22	0.23	0.28	0.29
mid	800 . . . 3150 Hz	0.30	0.28	0.36	0.32
high	4 . . . 40 kHz	0.38	0.35	0.46	0.42

Dealing with bad data points According to the analysis in figure E.3, APP60 is a bad data point for analysis of isolated jet noise. Nevertheless it can be still used for jet-flap-interaction analysis (see section 4.2).

If the operational conditions for a certain data point are really important, the next question is whether the test setup needs improvement. This can be done by increasing jet signal (nozzle with larger jet) or decreasing the background noise. During a wind tunnel experiment, it is only practical to try to decrease the background signal rather than to design a new nozzle.
A large background noise source is the engine support system/engine holder (compare BGN2 and BGN3 in figure 4.2). Any noise reduction should increase the acceptable velocity range for good background noise correction.

However, there is a limit to good measurements, especially for wake flow or near unity velocity profile shear layers. With an ideal holder, the measurement limit for the P25H engine may be extended to velocity ratios somewhere below $r_{U,OSL} = 0.6$, but rather not higher (see appendix H).

Alternatively, the background noise correction may only be done for some of the frequency bands. The frequency bands with too low signal to noise ratio are typically corrected to a priorly defined default value, e.g. $SPL_{corr} = -300\,\mathrm{dB}$ for $B \leq 3\,\mathrm{dB}$.

E.0.3. Isolated high-lift wing noise

As mentioned in section 4.1.2, the DLR-F16 model was not tested with a full span width wing, but with the cutout slat (see figure E.5). There is a test where secondary

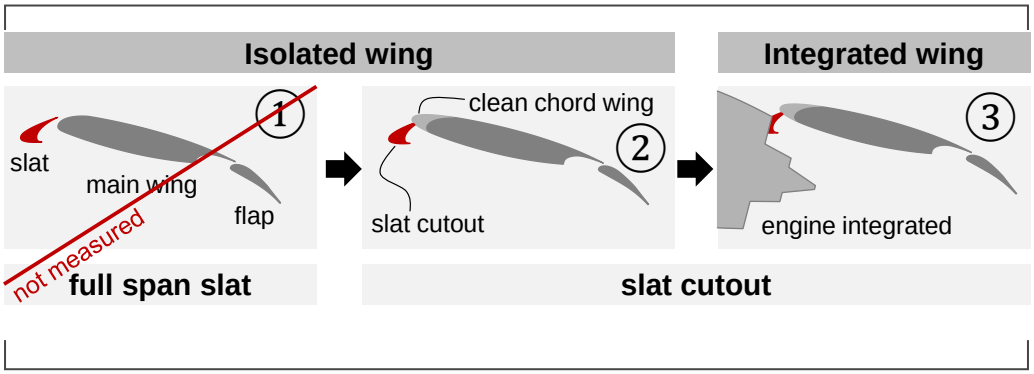

Figure E.5.: **Different high-lift wing builds**

air supply and engine are not installed (isolated wing), as well as the test where the engine is installed (engine integrated to wing). Hence, the background noise correction for the isolated wing is checked and thereafter, the integration of the engine to the wing is analysed.

Isolated wing background noise The method for the correction of background noise from section E.0.1 is also used for the evaluation of the isolated wing signal. The frequency range has been split as before (1st peak, 2nd peak, full scale relevant frequency range). The analysis has been conducted on the DLR-F16 wing which is installed at a geometric installation angle of $\alpha_{geo} = 14.5\,^\circ$ for two flap deflection angles ($\delta_F = 25\,^\circ$ and $35\,^\circ$) and operated at various wind tunnel speeds (see figure E.6).

Almost all of the data points have a sufficiently large measured signal to noise ratio. An exception are the wing settings with the lower flap deflection angle of $\delta_F = 25\,^\circ$: At high wind tunnel speeds, the correction of the 1^{st} low frequency peak is disputable. For the analysis of this peak in context of the jet-flap interaction problem, lower velocities or higher flap deflection angles can be used in order to ensure good data quality.

The integrated wing The data evaluation for an isolated wing (build #4) is straight forward: The operational settings are unambiguous (engine is deinstalled), and the unwanted background noise sources are minimal (only side plates, no engine holder).

Nevertheless, the measurement of the wing with a BGN1 setting (build #1, see figure 4.2) is also very promising because it is time-effective, accurate in installation, and it does not require a costly build change.

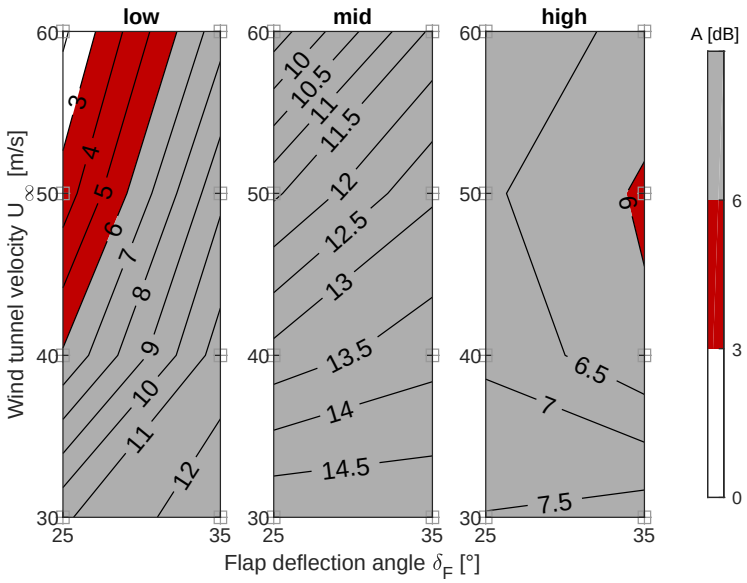

Figure E.6.: **Background noise of isolated wing**

Therefore, this setup is tested in figure E.7. The measured signals for the isolated wing and integrated wing are in general very similar. There are larger discrepancies around 1 . . . 2.5 kHz where Rossiter-like tones should be expected. The wings were slightly differently prepared which is one reason why they differ in this region. Furthermore, there is a difference in the low frequency peak (figure E.7a, solid lines).

The background noise correction has been initially done w.r.t. the correct background settings (figure E.7b, dashed lines), i.e. BGN3 for the isolated wing as well as BGN2 the integrated wing. Since the integrated wing signal appears to be over corrected for low frequencies, a mixed correction has been tested, i.e. integrated wing (BGN3).

The evaluation of the SPL differences between integrated and isolated wing (figure E.7c) show, that the integrational wing setting may be useful for analyzing the high frequency and possibly the mid frequency JFI effect. It is, however, debatable to evaluate the low frequency JFI effect with the integrated wing setting.

It is not very easy to decide which setting is more trustworthy for comparison. According to the mathematical analysis of the full scale relevant frequency range (figure E.7c), the integrated wing minimally underestimates the isolated wing signal.

An open question for using the integrated wing is the no thrust operational setting

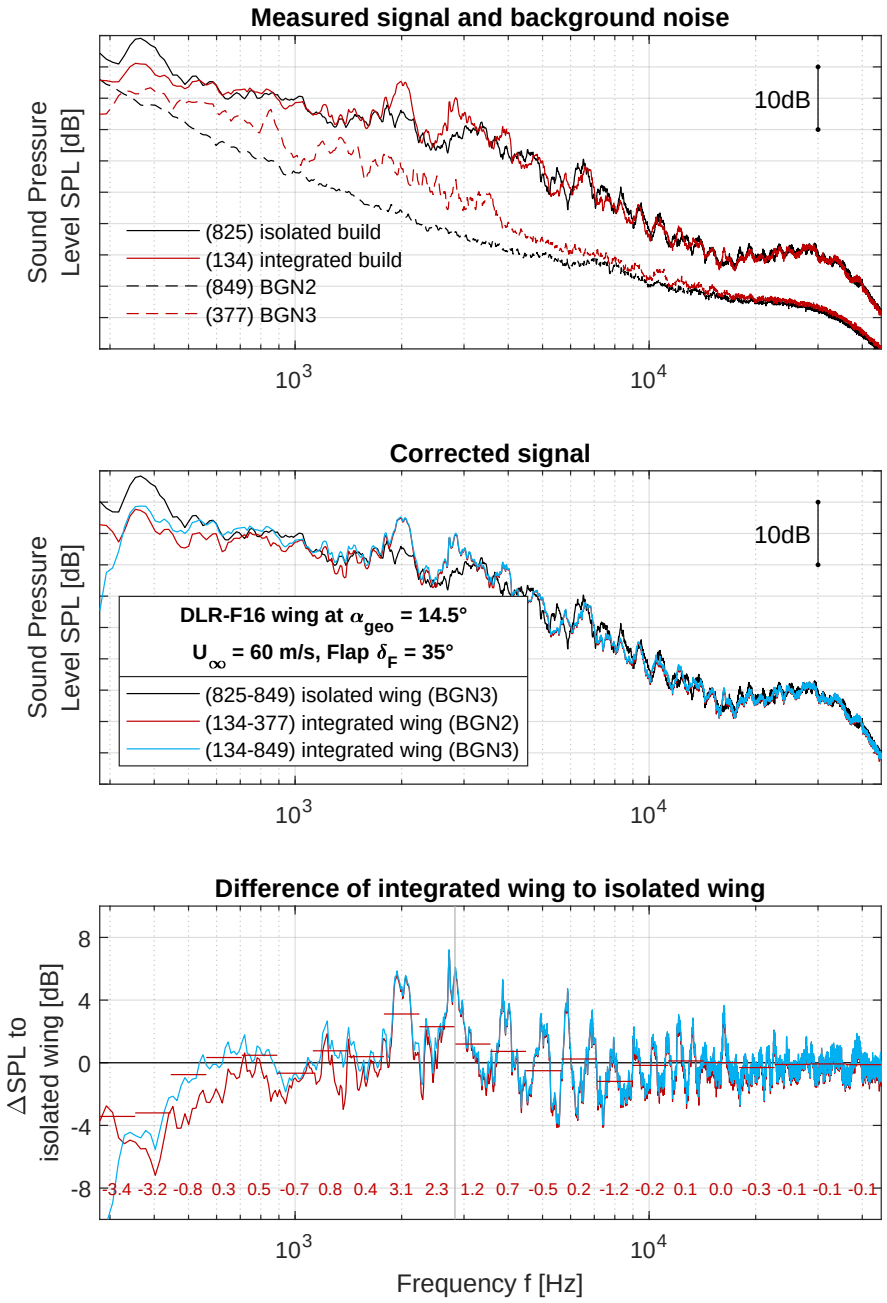

Figure E.7.: **Spectrum of isolated HL wing vs. integrated HL wing**

of the engine (engine off vs. matched jets). This is discussed in appendix I.1. The 'engine off' condition, which is also used in figure E.7, is very similar, but slightly higher than the 'matched jets setting'.

F. The ambiguity problem in the other source region

Engine integration effects other than jet-flap interaction are difficult to detect by direct evaluation of spatial source region using beamforming methods. The problem is the number and type of noise sources present in the other source region. Nevertheless, in this section a conventional evaluation is tried out. Contrary to the suggestions, an 'engine on' setting is used.

The example to be studied is height variation where the focus is on the wider setting (larger height). For both settings, it is assumed that the beamforming map is the same and the other SR is evaluated. The following conclusions can be drawn:

- Due to the greater height, the measured slat noise should decrease as the slat moves farther away from the microphones. The effect can be observed comparing the changes for an isolated wing (no data shown). The integrated wing with an 'engine off' condition may also show the effect, yet also include the sought other engine integration effect. An example is shown in figure F.1.
  When the engine is switched on, there will be some nozzle exit noise at a fixed position. With two source types present in the region where one source remains in position (engine related noise) and the other changes due to height (slat related noise), it is not possible to compare the two height builds by normalization of height.

- There is some reason for the nozzle exit noise to change underneath a wing when the height is altered. The wing pressure side determines the static pressure for the jet and its outer shear layer. Underneath the wing the jet is not fully expanded. Hence, all the velocities are below their target value. The greater height of the wing changes the static pressure in the jet and shear layer and thus the velocity profile. This change of initial conditions may be relevant or dimensionally negligible. Note that this effect is independent of the engine integration build design between engine and slat. It is a change to a jet-related noise source due to the presence of the main wing. One could say that this is a jet-wing effect. Unfortunately, it cannot be studied very well: As soon as the wind tunnel is switched on, slat-related sources and engine

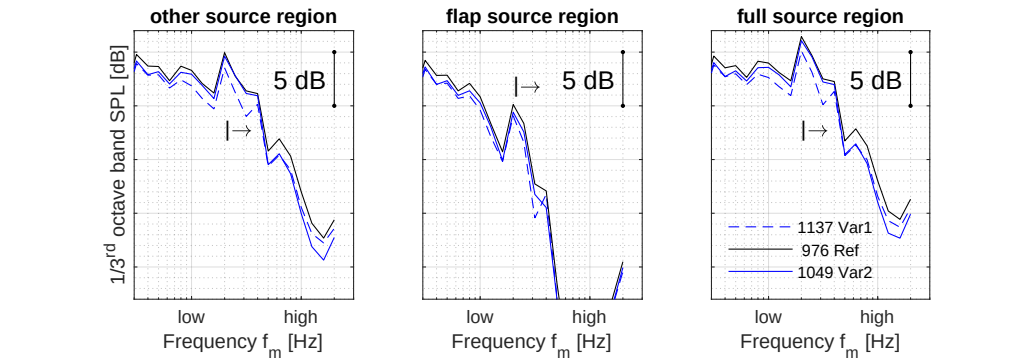

Figure F.1.: **Slat & slat related noise change with greater height**

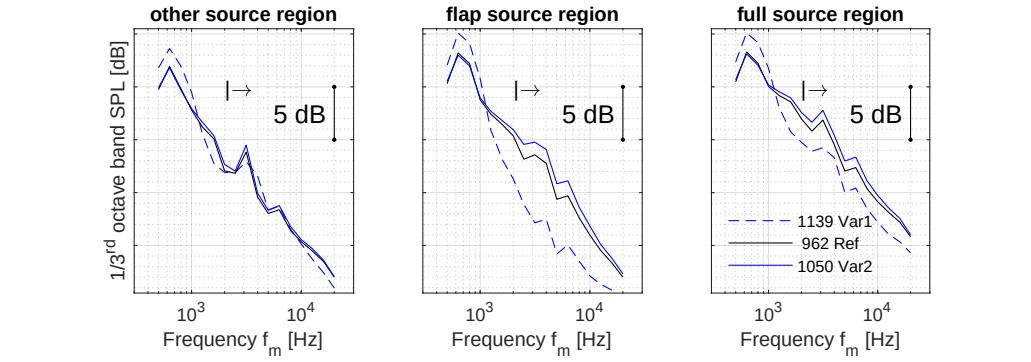

Figure F.2.: **Static jet APP– at different heights**

integration effects are present in the SR.

The only hypothetical chance is switching off the wind tunnel and studying different heights for static jet settings (figure F.2). However, it must be assumed that there is no flight stream induced static pressure field of the wing present - which would be necessary to study any changes to the nozzle exit noise. The more important change to nozzle exit noise may be rather caused by space confinement and the resulting jet deformation. In the example (figure F.2), there are some changes in the other SR ($\Delta SPL \approx 1$ dB) which support the theory, but they are also small compared to the changes in the flap source region.

With such existing effects, the 'engine on' operation cannot be used to distinctly

determine other engine integration related effects in the other SR.

The best option to figure out whether the experimental design is suitable, is to stick with a comparison between isolated and integrated wing (engine off) in order to study slat cutout design related effects. Such a study could possibly reveal a jet-wing interaction effect due to small changes of the nozzle exit noise. The question is how to deal with it, treat it as a separate phenomenon or account this to jet-flap interaction. There may be reasons to isolate noise sources as best as possible. However, it simplifies the evaluation procedure to account this phenomenon to the determination and evaluation of the jet-flap interaction effect.

G. Full measurement options for JFI noise problems

For reason of a minimal number of build options, the measurement of the isolated jet noise was suggested with the boundary conditions of a jet-flap interaction measurement (side plates are installed, see section 4.4). There might be good reasons to remove the side plates, because why would an engine manufacturer measure a wing holder?

However, for the background noise measurement of the acoustic jet-flap interaction problem, the effect of both of the holders must be measured as (unwanted) background noise unless the effect of the side plates is negligible. For high frequencies (see figure 4.2, $f \geq 8\,\mathrm{kHz}$), the side plates cannot be neglected against the engine holder.

In order to account for the options in which the wind tunnel pipe is installed, build option 2 (side plates installed) is extended by another build option 5 (side plates removed). This blows up the measurement and evaluation options (see G.1) from 3 to 12 - too many for a non-complex thought process in the main text. The optimal performance build needs 6 different data points for 5 builds (see figure G.2).

		SIGNAL **int. / iso. HL wing**	BGN HL wing	SIGNAL **iso. engine**	BGN engine	SIGNAL **full build**	BGN w / w/o side plate	empty wind tunnel	side plate + wt pipe + wing	side plate + wt pipe	side plate	side plate + wing	wt pipe			
Application	**crit. #1**	**HL w.**		**eng.**		**JFI**		0	1	2	3	4	5	**dpts**	**builds**	**evaluation**
should work for all JFI-problems	no high-lift wing	X		2	-	1	-		X	X				**2**	**2**	static jet or JFI w/
				5	-		-			X			X	**2**	**2**	quasi-single jet noise
	isolated high-lift wing	4	3	2	2	1	2		X	X	X	X		5	4	
							5		X	X	X	X	X	6	5	
				5	5		2		X	X	X	X	X	**6**	**5**	optimal performance
							5		X		X	X	X	5	4	good compromise
only high-lift wing w/slat & mid/high freq. range	engine integrated to high-lift wing	1	2	2	2	1	2		X	X				**4**	**2**	optimal in time+cost
							5		X	X			X	5	3	
				5	5		2		X	X			X	5	3	
							5		X	X			X	5	3	
			5	2	2		2		X	X			X	5	3	
							5		X	X			X	5	3	
				5	5		2		X	X			X	5	3	
							5			X			X	**4**	**2**	optimal in time+cost

crit. #2: side plates installed (2) or removed (5)

Figure G.1.: **Measurement options for jet-flap interaction noise problems**

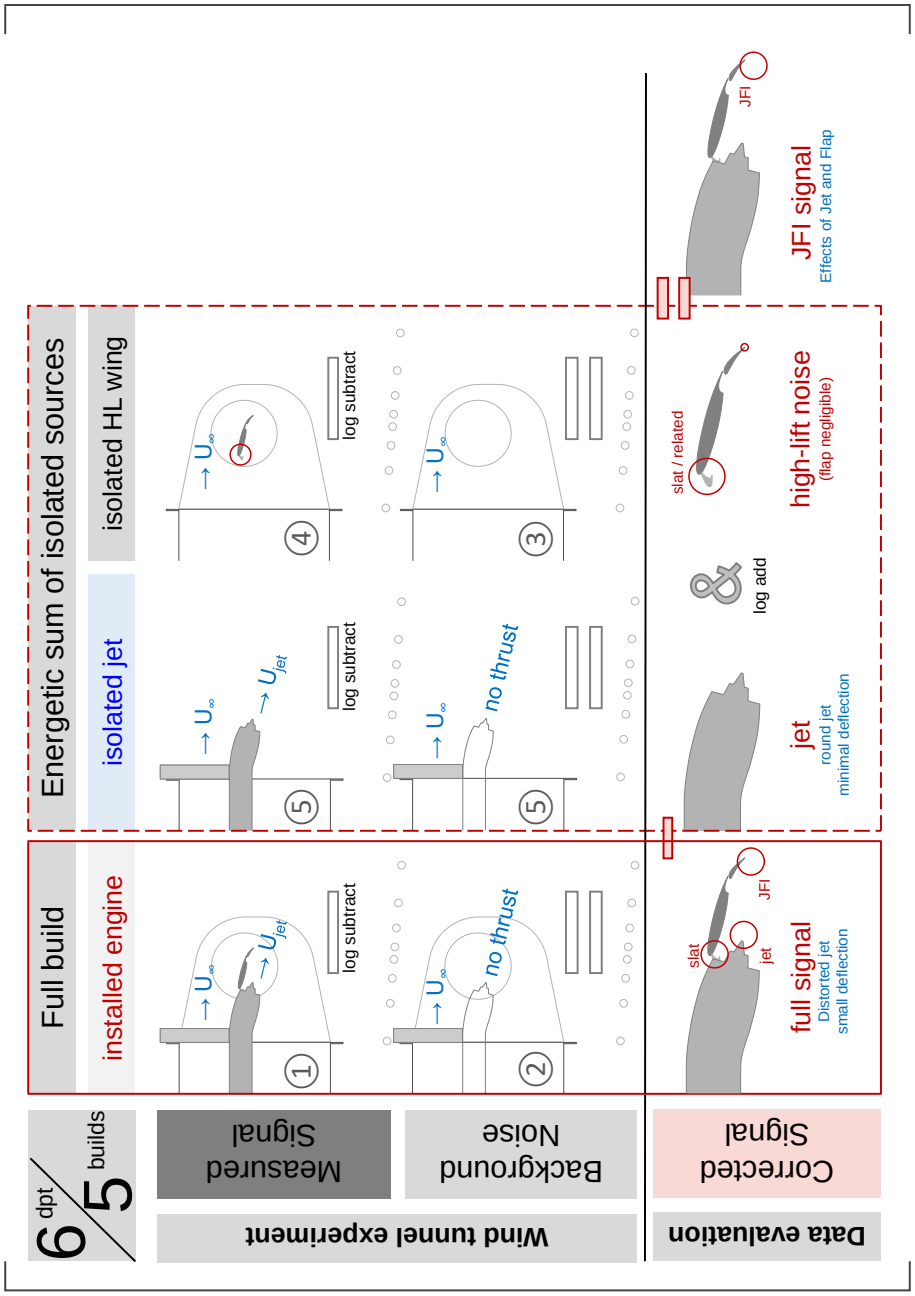

Figure G.2.: **6/5 measurement technique for jet-flap interaction noise**

H. Operational limits for isolated jet noise measurements with an acoustically ideal jet test rig

Let us assume that the extra noise from the engine holder and wind tunnel pipe (BGN2) can be completely diminished down to the background noise of the empty wind tunnel (build 0). Then, the AWB nozzle's jet noise as well as rig noise from the AWB nozzle duct will still be present. Hence, there is a limit to properly measure shear layers with rather weak velocity ratios close to unity. Where is this limit?

A direct comparison without actually minimizing the engine holder noise is not possible. The upper limit for the flight jet noise can be estimated with the help of static jet noise. The wind tunnel is not operated, hence the wind tunnel related background noise can be neglected.

The results are plotted in figure H.1. The thick red lines show the static jet noise which are also the maximally expected signal for the corresponding flight jet noise. The actually measured levels at flight jet operations (thin red lines) are higher than the corresponding static jet noise, but nearly equal to the actual background noise (thin grey lines) with the installed (real) jet test rig. The jet test rig consists of jet air supply pipe (wind tunnel pipe) and the V-shaped engine holder. An ideal jet test rig does not cause any acoustic penalty in the background noise, it produces the same noise levels as the empty wind tunnel (thick black lines).

Hence, the question of the maximum velocity ratio limit for an ideal jet test rig can be answered by evaluating the signal to noise ratio between the static jet (thick red) and the background noise of the empty wind tunnel (black): At velocity ratios of $r_{U,OSL} = 0.75$ the signal (thick red) is lower or equal to the ideal background noise (thick black). As a consequence, the measured signal (red) is very similar to the background noise (grey).

At velocity ratios of $r_{U,OSL} = 0.6$, there is some (hardly useful) signal which could potentially be measured and corrected for the frequency range between $f = 1 \ldots 6\,\mathrm{kHz}$.

Therefore, $r_{U,OSL} = 0.6$ is an upper boundary for isolated jet noise measurement in the AWB.

A more accurate limit of $r_{U,OSL} \approx 0.4$ can be determined by finding the flight jet operation which produces the same jet noise level as the tested static jet:
Assuming that flight jet noise scales with $I \propto (U_j - U_\infty)^8$ in the rear arc, the static jet noise of $\Delta U = 100\,\mathrm{m/s}$ and $U_\infty = 0\,\mathrm{m/s}$ is equal to flight jet noise at $\Delta U = 100\,\mathrm{m/s}$ and $U_\infty = 60\,\mathrm{m/s}$. This corresponds to a velocity ratio of $r_{U,OSL} = 60/160 = 0.375$.
The flight jet noise scaling analogy for forward arc to overhead flight jet noise is slightly different: The velocity ratio limit is $r_{U,OSL} = 60/153.4 = 0.42$ when assuming $I \propto (U_j - U_\infty)^6 U_c^2$.

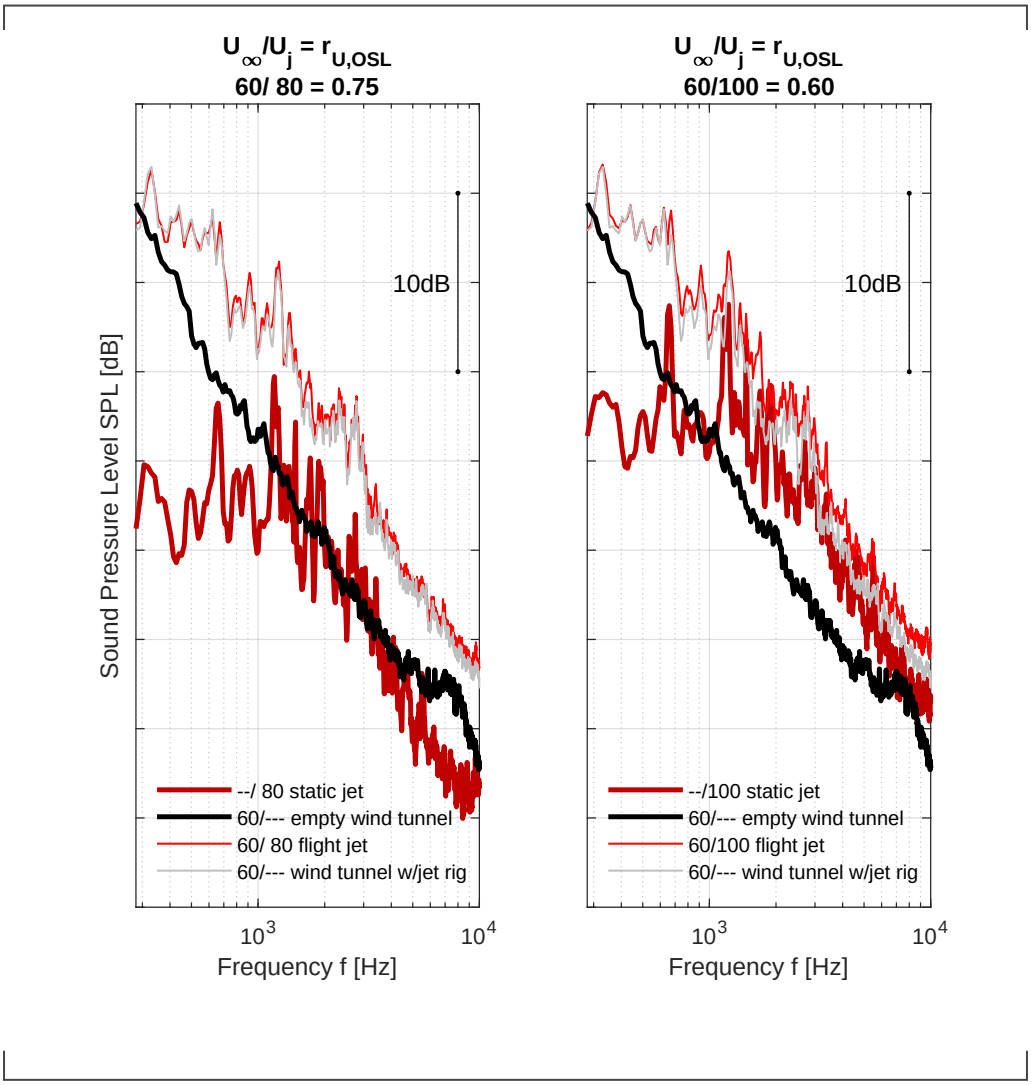

Figure H.1.: **Max. velocity ratio estimation using an ideal engine holder**

I. Low speed measurements with matched jets or engine-off condition

I.1. Integrated wing measurement

The integrated wing build (BGN3) can be used for a time and cost efficient high-lift-wing measurement. This test is very cost effective if no secondary air is needed. Hence, the spectra of a 'matched jets' setting (red) and an 'engine off' setting (grey) are compared in figure I.2.

In general, the engine off operational setting is very similar to the matched jets setting. Greater uncertainties are caused by the Rossiter-like tones which formulate within the slat cove: This is because here the slat has not been treated with noise reduction means. Therefore, the margins in the frequency range between $1 \ldots 2\,\mathrm{kHz}$ as well as the tone at $4\,\mathrm{kHz}$ are slightly off.

The 'engine off' setting produces negligibly higher sound pressure levels than the 'matched jets' setting. There is a positive offset of $\Delta SPL \approx 0.5\,\mathrm{dB}$ within the full frequency range $2.5 \ldots 40\,\mathrm{kHz}$.

Note that the first peak at $f = 340\,\mathrm{Hz}$ represents most likely a physical effect which should also occur in orginal scale. It can be also observed in the static jet measurement. This is a setting where the wind tunnel is switched off and where the jet can interact with the flap (and main wing).

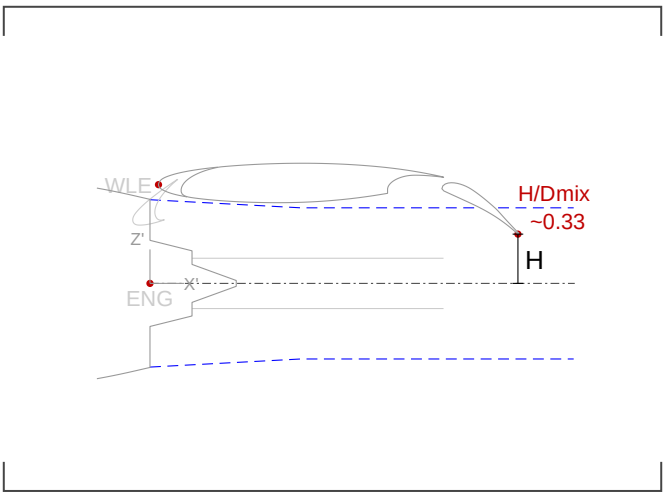

Figure I.1.: **Build: integrated wing**

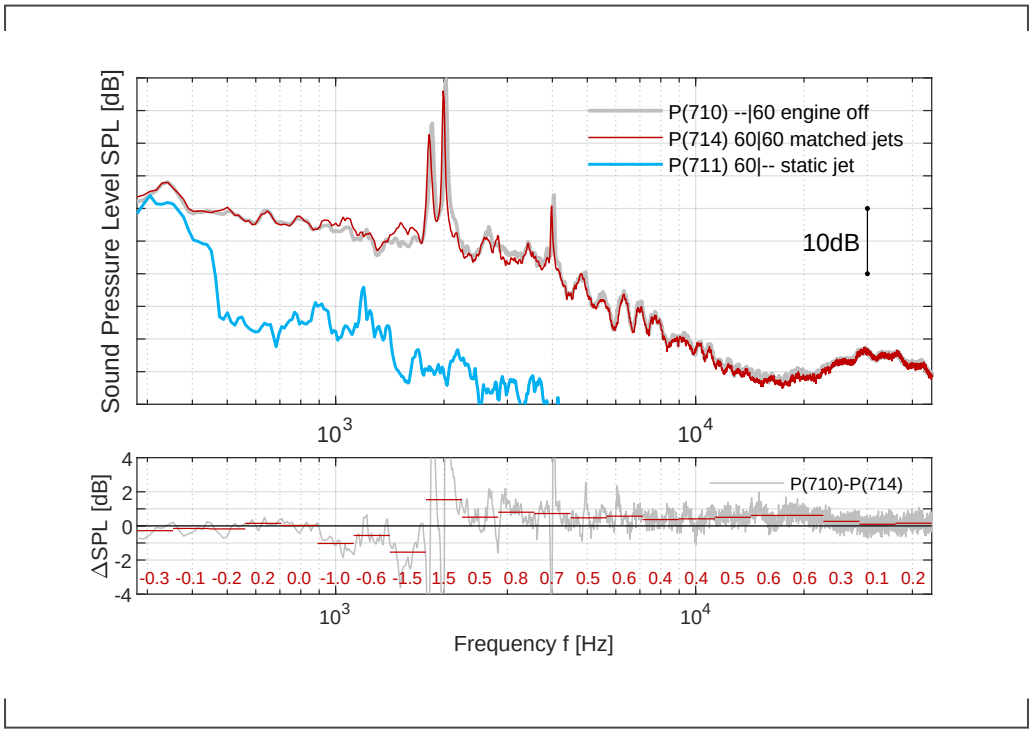

Figure I.2.: **Thrust setting for integrated wing (BGN3) measurement**

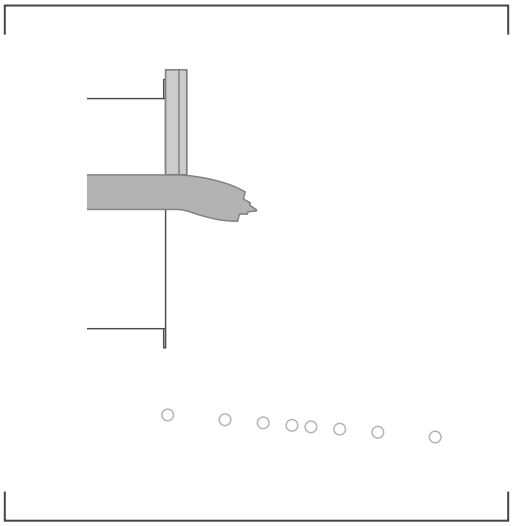

Figure I.3.: **BGN2 build: isolated engine**

I.2. Isolated jet background noise measurement

The same method is used for the decision which operation shall be used for the isolated jet background noise measurement (see build in figure I.3) and results in figure I.4.

The 'engine off' condition (grey) is very similar to the matched jets measurements (red). Therefore, the more cost-effective 'engine off' data points can be used for correction.

It must be considered that there is a chance of getting an unrepresentative amount of unwanted duct noise for 'matched jets' because the engine operates in an off-design condition. However, the conditions for the test data in figure I.4 are very good. This is because even the empty wind tunnel (build #0, black) background noise is large compared to the static jet (blue) which might be potentially contaminated with duct noise.

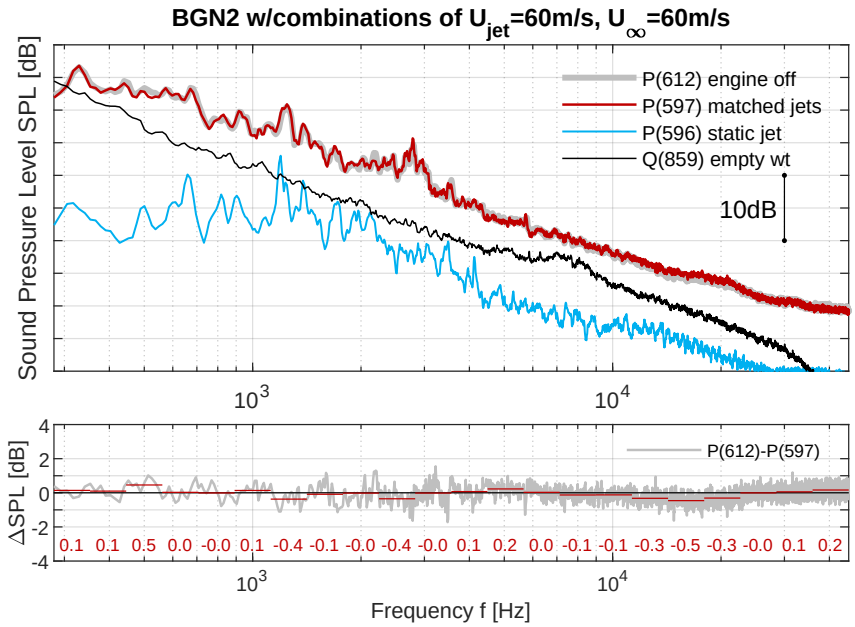

Figure I.4.: **Thrust setting for isolated jet background noise measurement (BGN2)**

J. Mean flow data in the jet-flap interaction experiment

A CFD simulation (credits to Dirk Boenke [5], then DLR) will be used in order to explain the flow situation underneath the high-lift wing. Due to the lack of an isolated high-lift wing simulation, an off-centered (i.e. more inboard/outboard) wind tunnel plane ($Y = -0.2\,\mathrm{m}$) is used to approximate the behavior of the isolated high-lift wing (see figures J.1a). The simulation results are presented in figures J.1 to J.5.

Note that the secret of the plots are the sharp focused resolution around characteristic flow properties, e.g. the wind tunnel velocity. This means that almost none of the plots is resolved for the full scale of the flow property: For example, the zero velocity of the wind tunnel chamber and the high jet velocity are not well resolved. In some of the graphics, a key property is displayed in orange.

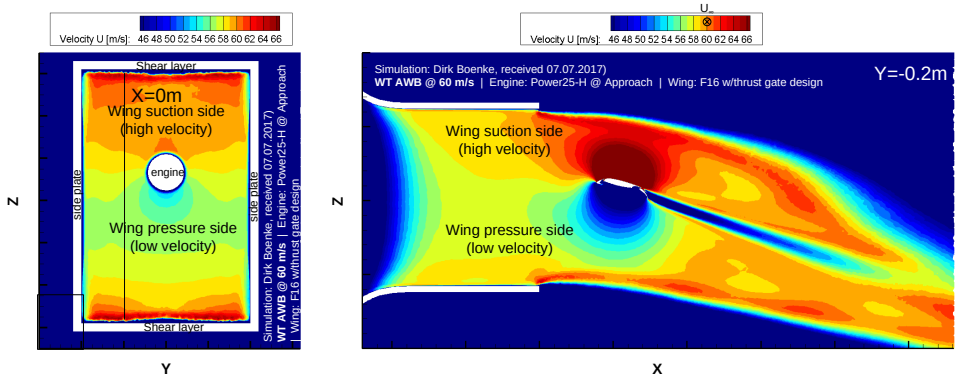

(a) **high-lift wing**

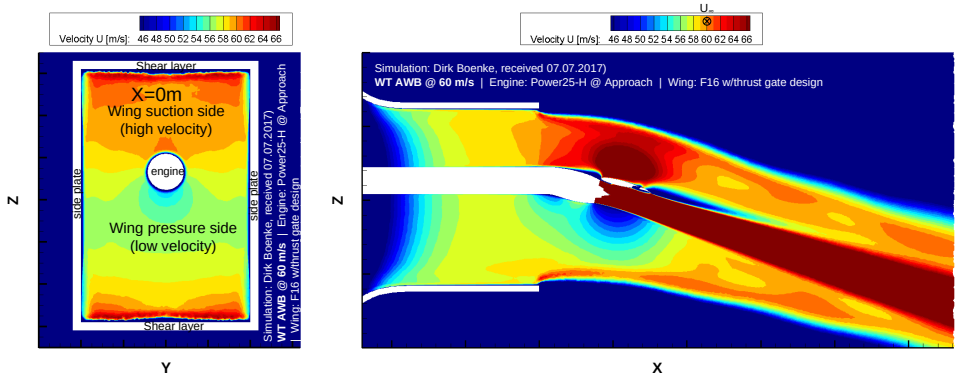

(b) **engine installed to high-lift wing**

Figure J.1.: **Extracted resolution focused around mean wind tunnel velocity (orange = target wind tunnel velocity)**

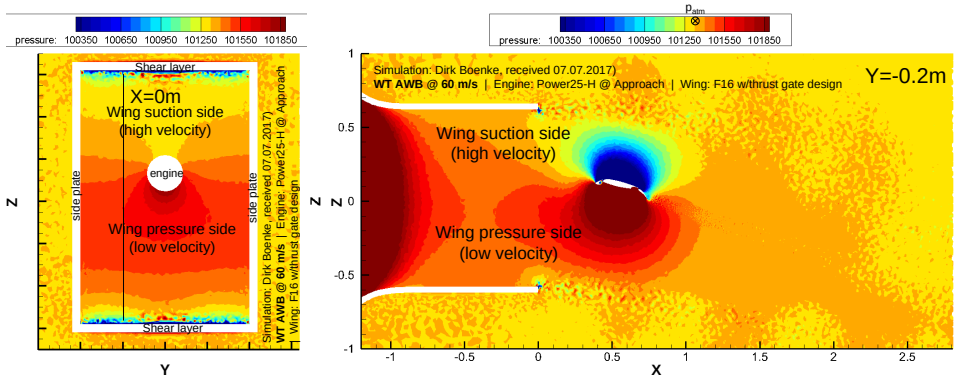

(a) **high-lift wing**

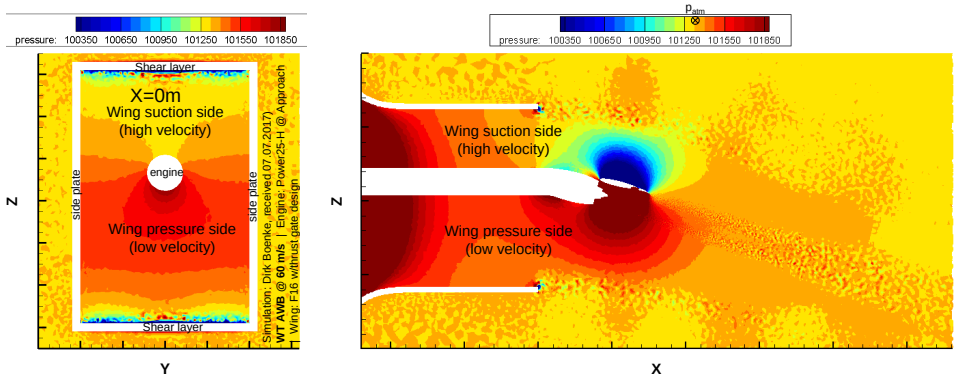

(b) **engine installed to high-lift wing**

Figure J.2.: **Extracted resolution focused around ambient wind tunnel pressure (orange = target ambient static pressure)**

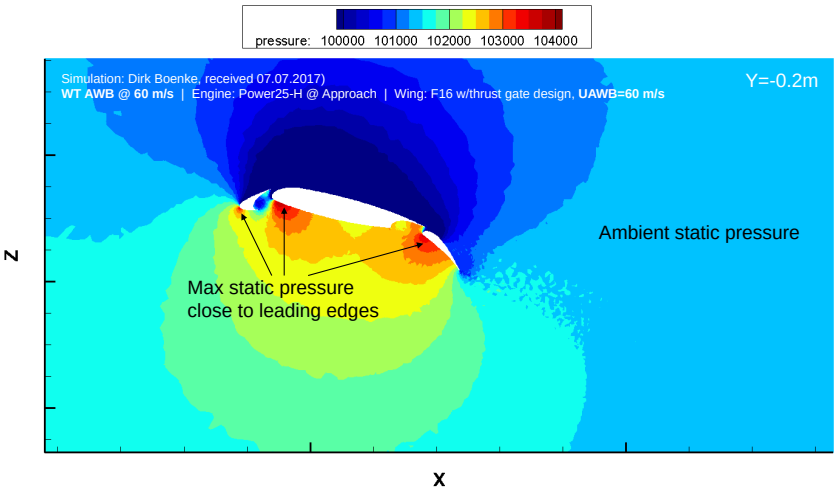

(a) **high-lift wing**

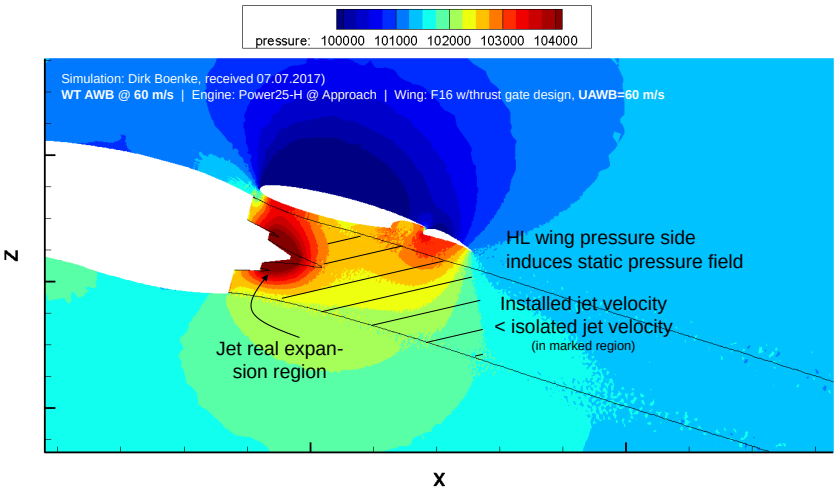

(b) **engine installed to high-lift wing**

Figure J.3.: **Extracted resolution focused around static pressure on wing pressure side**

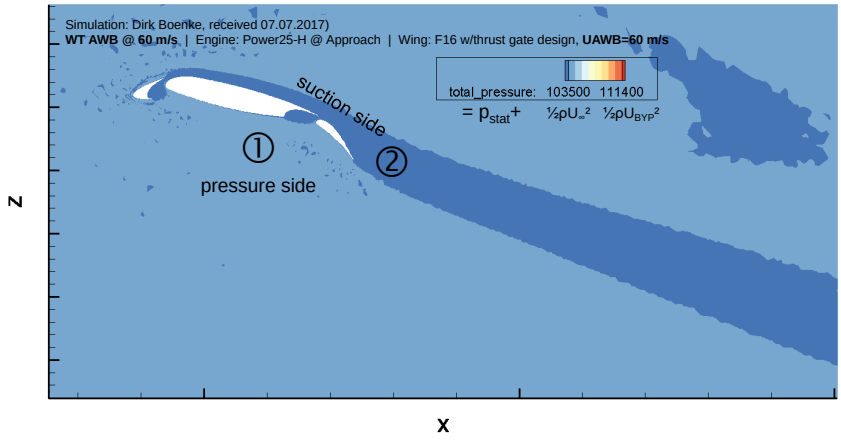

(a) **high-lift wing**

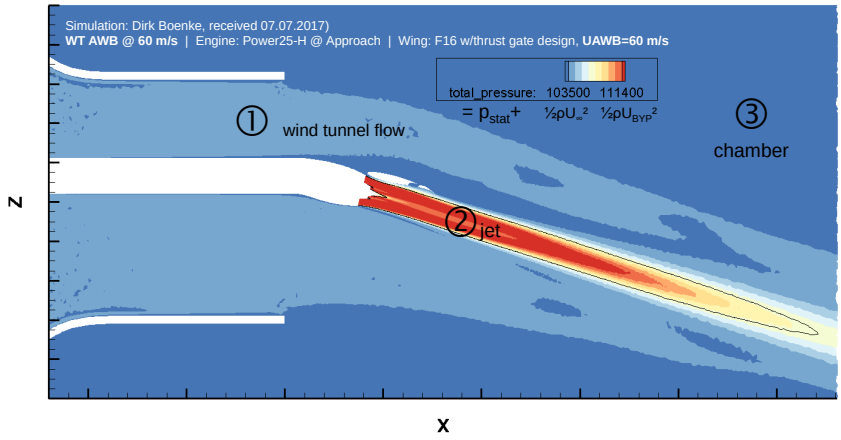

(b) **engine installed to high-lift wing**

Figure J.4.: **Extracted resolution focused around total pressure**

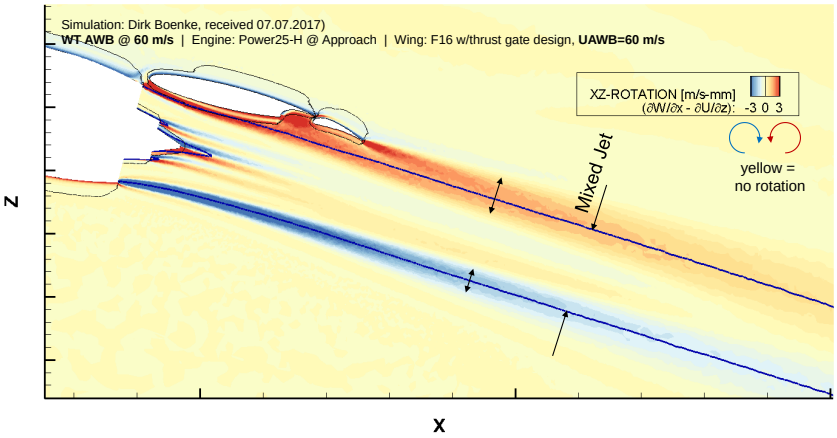

(a) **engine installed to high-lift wing**

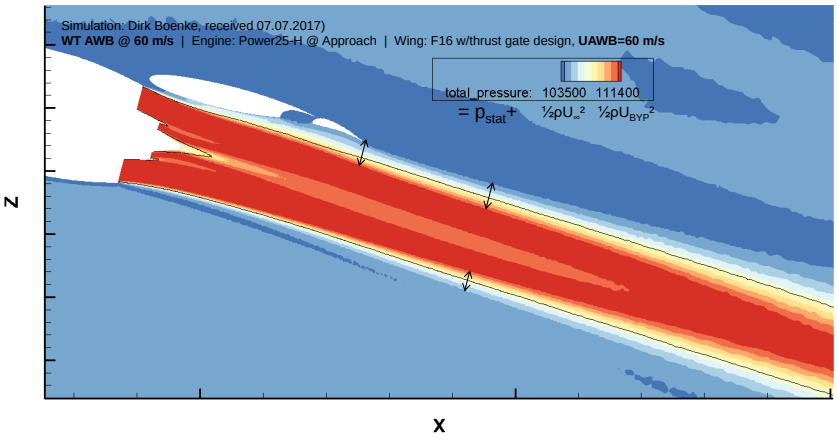

(b) **engine installed to high-lift wing**

Figure J.5.: **Shear layer displayed by rotation as well as total pressure**

K. Extended study on an improved jet-flap diagram

If the available flap trailing edge height H restricts the required space for an isolated jet shear layer, not only 1D geometrical parameters such as height differences or angles are important. The redistribution of the jet also suggests an analysis of the intersection and redistribution areas[1] Even though a thorough study exceeds the scope of this thesis, it can be shown that the areas cannot be calculated easily by one single geometric ratio.

The first question is how much of the cross-sectional area of the (isolated) jet is intersecting with the space requirements of the flap. The concept of using the cross-sectional area and possibly a shape coefficient is well-used in aerodynamic studies and therefore a good option. A more difficult task is to determine which parts of the jet can be compressed, and which must be redistributed. The second question is how much space is available to redistribute the jet.

The first question can be answered by calculating the difference between the combined area (1,2) and (2) (see figure K.1). For all $Z_{...} = [H_{OSL,i}, R_{mix}, H_{OSL,o}]$

$$\cos(\psi_{...}) = \frac{H}{Z_{...}} \tag{K.1}$$

$$\frac{A_{ci,...}}{\pi Z_{...}^2} = \begin{cases} 0 & \text{, if } \frac{H}{Z_{...}} \geq 1 \\ \left(\frac{\psi_{...}}{180\,^\circ} - \frac{H}{Z_{...}} \frac{\sin(\psi_{...})}{\pi} \right) & \text{, if } \frac{H}{Z_{...}} < 1 \end{cases} \tag{K.2}$$

Note that it is not necessarily clear at which position $H_{OSL,o}(x = ...)$ should be evaluated. Potential candidates are the flap trailing edge ($x = L$) as well as the intersection point with the wing or flap pressure side.

The above area ratios help to quantify areas of the jet which must adjust (i.e. potential core) as well as the ones which may be slightly compressed. A radical assumption would be the entire decimation of the shear layer:

$$A_{c,OSL,full} = A_{ci,fulljet} - A_{ci,pot.core} \tag{K.3}$$

[1] Some sources can be interpreted to rather suggest the actual impingement area [42] (2D geometries).

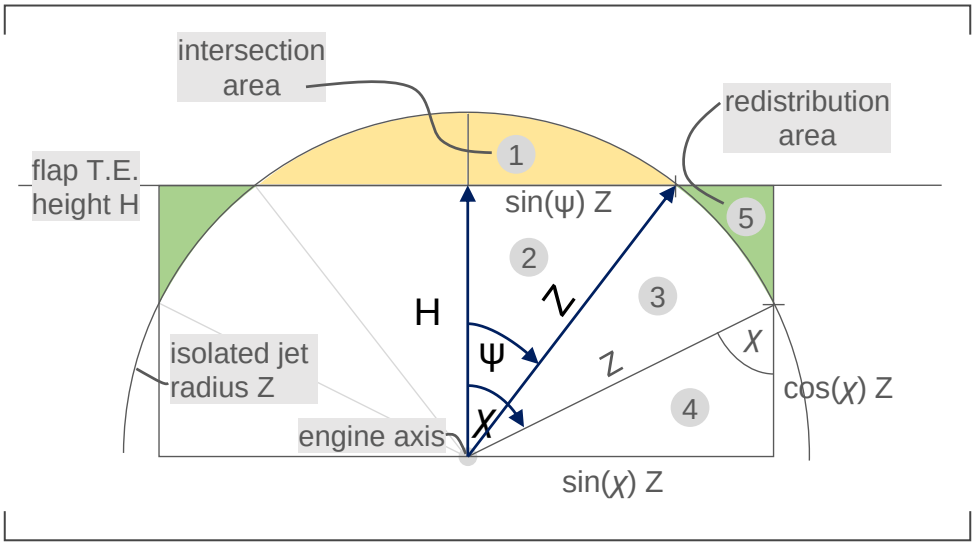

Figure K.1.: **Geometric model for the calculation of intersection and redistribution areas**

A more conservative approach is to assume that the properties in the mixing radius of the jet would rather not adjust:

$$A_{c,OSL,part} = A_{ci,fulljet} - A_{ci,mix} \tag{K.4}$$

The redistribution of the jet may be possible within a (fixed) angle in the range of $\chi = 0 \ldots 90\,^\circ$ of the mixed jet.

$$\cos(\chi) < \frac{H}{Z} < 1\text{:}\ \underbrace{A_{redist.}}_{5} = \underbrace{2\sin(\chi)HZ_{\ldots}}_{2,3,4,5} - \underbrace{\sin(\psi_{\ldots})HZ_{\ldots}}_{2} + \ldots \\ - \underbrace{\frac{(\chi - \psi_{\ldots})}{180\,^\circ}\pi Z^2_{\ldots}}_{3} - \underbrace{\frac{1}{2}\sin(2\chi)Z^2_{\ldots}}_{4} \tag{K.5}$$

$$\frac{H}{Z} < \cos(\chi)\text{:}\ A_{redist.} = 0 \tag{K.6}$$

Bibliography

[1] Roy K. Amiet. Correction of open jet wind tunnel measurements for shear layer refraction. In 2nd Aeroacoustics Conference, Aeroacoustics Conferences. American Institute of Aeronautics and Astronautics, 1975.

[2] John D. Anderson. Modern Compressible Flow: With Historical Perspective. Aeronautical and Aerospace Engineering Series. McGraw-Hill Education, 2003.

[3] Henry E. Bass, Louis C. Sutherland, and Allan J. Zuckerwar. Atmospheric absorption of sound: Update. The Journal of the Acoustical Society of America, 88(4):2019–2021, 1990.

[4] Ivan V. Belyaev, Georgy A. Faranosov, Nikolay N. Ostrikov, and Gennady Paranin. A parametric experimental study of jet-flap interaction noise for a realistic small-scale swept wing model. In 21st AIAA/CEAS Aeroacoustics Conference, AIAA Aviation Forum. American Institute of Aeronautics and Astronautics, 2015.

[5] Dirk Boenke. CFD RANS-Simulation on JFI noise, 07.07.2017.

[6] Willy J. G. Bräunling. Flugzeugtriebwerke: Grundlagen, Aero-Thermodynamik, ideale und reale Kreisprozesse, Thermische Turbomaschinen, Komponenten, Emissionen und Systeme. Flugzeugtriebwerke, 2009.

[7] James Bridges and Mark Wernet. Establishing consensus turbulence statistics for hot subsonic jets. In 16th AIAA/CEAS Aeroacoustics Conference, Aeroacoustics Conferences. American Institute of Aeronautics and Astronautics, 2010.

[8] Olaf Brodersen and Michael Pott-Pollenske. KonTeKst - Projektabschlussbericht: DLR IB 232-2020 C XX. 2020.

[9] Brüel & Kjær. Product data: Condenser microphone cartridges — types 4133 to 4181. page 7.

[10] André V.G. Cavalieri, Peter Jordan, William R. Wolf, and Yves Gervais. Scattering

of wavepackets by a flat plate in the vicinity of a turbulent jet. Journal of Sound and Vibration, 333(24):6516–6531, 2014.

[11] Stanislav Denisov, Georgy Faranosov, Nikolay Ostrikov, and Oleg Bychkov. Theoretical modeling of the excess noise due to jet-wing interaction. In 22nd AIAA/CEAS Aeroacoustics Conference, Aeroacoustics Conferences. American Institute of Aeronautics and Astronautics, 2016.

[12] William Devenport. Compressible Aerodynamics AOE 3114 - course lecture.

[13] Werner Dobrzynski. Scherschichtkorrektur nach Amiet unter Berücksichtigung einer zusätzlichen Temperaturgrenzschicht. Arbeitsdiagramme für die Korrektur akustischer Signale bei Fernfeldmessungen in Windkanälen mit offenen Messstrecken. DFVLR-Mitteilung 84-11, 1984.

[14] Bernhard Eisfeld. Turbulence modeling for free shear flows. In AIAA Aviation 2019 Forum, AIAA Aviation Forum. American Institute of Aeronautics and Astronautics, 2019.

[15] Vincent Fleury and Renaud Davy. Large-scale jet noise testing, reduction and methods validation "EXEJET": 5. Analysis of jet-airfoil interaction noise by microphone array techniques. In 20th AIAA/CEAS Aeroacoustics Conference, AIAA Aviation Forum. American Institute of Aeronautics and Astronautics, 2014.

[16] Helmut V. Fuchs and Ulf Michel. Experimental evidence of turbulent source coherence effecting jet noise. In 4th Aeroacoustics Conference, Aeroacoustics Conferences. American Institute of Aeronautics and Astronautics, 1977.

[17] Richard Gaeta and Krish Ahuja. Subtle differences in jet noise scaling with narrow band spectra compared to 1/3-octave band. In 9th AIAA/CEAS Aeroacoustics Conference and Exhibit, Aeroacoustics Conferences. American Institute of Aeronautics and Astronautics, 2003.

[18] W. K. George, R. Arndt, R.E.A. Arndt, and S. Corrsin. Advances in turbulence: The self-preservation of turbulent flows and its relation to initial conditions and coherent structures. Springer, 1989.

[19] Brenda Henderson, Kevin Kinzie, and Henry Haskin. The effect of nozzle trailing edge thickness on jet noise. In 10th AIAA/CEAS Aeroacoustics Conference, Aeroacoustics Conferences. American Institute of Aeronautics and Astronautics, 2004.

[20] Jerome Huber, Magdi Omais, Alexandre Vuillemin, and Renaud Davy. Character-

ization of installation effects for HBPR engine, part 4: Assessment of jet acoustics. In 15th AIAA/CEAS Aeroacoustics Conference (30th AIAA Aeroacoustics Conference), Aeroacoustics Conferences. American Institute of Aeronautics and Astronautics, 2009.

[21] Christian Jente. Aeroakustische Wechselwirkung von Triebwerk und Tragflügel bei hohem Nebenstromverhältnis: Aeroacoustic Jet-Flap-Interaction at Ultra-High Bypass Ratio. Master's Thesis, Technische Universität Darmstadt, Darmstadt, 2015.

[22] Christian Jente. Drivers of jet-flap interaction noise: The thrust vs. shear layer difference velocity experiment. In EU H2020 1st DJINN Conference: Industrially oriented jet noise reduction technologies, 2021.

[23] Christian Jente. Strahl-Klappen-Interferenz – wie bedeutsam ist die Interaktionsschallquelle am Flugzeug. In Berlin Deutsche Gesellschaft für Akustik e.V. (DEGA), editor, DAGA 2022 - 48. Jahrestagung für Akustik, pages 1278–1281, 2022.

[24] Christian Jente and Jan Delfs. Velocity scaling of shear layer noise induced by cold jet flow with co-flowing flight stream. In 25th AIAA/CEAS Aeroacoustics Conference, Aeroacoustics Conferences. American Institute of Aeronautics and Astronautics, 2019.

[25] Christian Jente, Michael Pott-Pollenske, Dirk Boenke, Alexander Buescher, and Iris Goldhahn. Experimental investigation of jet-flap-interaction noise sensitivity due to varying flap parameters at a UHBR engine/high-lift-wing installation. In 24th AIAA/CEAS Aeroacoustics Conference, AIAA Aviation Forum. American Institute of Aeronautics and Astronautics, 2018.

[26] Christian Jente, Michael Pott-Pollenske, Dirk Boenke, and Alexander Büscher. Acoustic similarity modelling of a UHBR jet engine for the investigation of jet-flap-interaction noise. In 23rd AIAA/CEAS Aeroacoustics Conference, AIAA Aviation Forum. American Institute of Aeronautics and Astronautics, 2017.

[27] Christian Jente, Johannes Schmidt, Jan Delfs, Karl-Stéphane Rossignol, Michael Pott-Pollenske, and Henri A. Siller. Noise reduction potential of flow permeable materials for jet-flap interaction noise. In 28th AIAA/CEAS Aeroacoustics 2022 Conference.

[28] Peter Jordan, Vincent Jaunet, Aaron Towne, André V. G. Cavalieri, Tim Colonius, Oliver Schmidt, and Anurag Agarwal. Jet–flap interaction tones. Journal of Fluid Mechanics, 853:333–358, 2018.

[29] Abbas Khavaran and James Bridges. Jet noise scaling in dual stream nozzles. In 16th AIAA/CEAS Aeroacoustics Conference, Aeroacoustics Conferences. American Institute of Aeronautics and Astronautics, 2010.

[30] Vinod Mengle. The effect of nozzle-to-wing gulley height on jet flow attachment to the wing and jet-flap interaction noise. In 17th AIAA/CEAS Aeroacoustics Conference (32nd AIAA Aeroacoustics Conference), Aeroacoustics Conferences. American Institute of Aeronautics and Astronautics, 2011.

[31] Alfons Michalke. A note on the spatial jet-instability of the compressible cylindrical vortex sheet.

[32] Alfons Michalke and Ulf Michel. Prediction of jet noise in flight from static tests. Journal of Sound and Vibration, 67(3):341–367, 1979.

[33] Ulf Michel. On the systematic error in measurements of jet noise flight effects using open jet wind tunnels. In 21st AIAA/CEAS Aeroacoustics Conference, AIAA Aviation Forum. American Institute of Aeronautics and Astronautics, 2015.

[34] Ulf Michel, Felix Kramer, and Charles Mockett. The dominating influence of large-scale jet motion on jet-wing interaction noise. In 25th AIAA/CEAS Aeroacoustics Conference, Aeroacoustics Conferences. American Institute of Aeronautics and Astronautics, 2019.

[35] W. R. Miller. Flight effects for jet-airframe interaction noise. In 8th Aeroacoustics Conference, Aeroacoustics Conferences. American Institute of Aeronautics and Astronautics, 1983.

[36] Bruce R. Munson, Donald F. Young, and Theodore H. Okiishi. Fundamentals of Fluid Mechanics. Wiley, 5 edition, 2006.

[37] Leandro Rego, Damiano Casalino, Francesco Avallone, and Daniele Ragni. Noise amplification effects due to jet-surface interaction. In AIAA Scitech 2019 Forum, AIAA SciTech Forum. American Institute of Aeronautics and Astronautics, 2019.

[38] Lennart Rossian. Minderung der Schallabstrahlung von aktiven Hochauftriebssystemen mit porösen Materialien. Doktorarbeit, Technische Universität Braunschweig, Braunschweig, 2020.

[39] R. D. Sandberg and B. J. Tester. Mach-number scaling of individual azimuthal modes of subsonic co-flowing jets. Journal of Fluid Mechanics, 793:209–228, 2016.

[40] Oliver T. Schmidt, Aaron Towne, Tim Colonius, André V. G. Cavalieri, Peter Jordan, and Guillaume A. Brès. Wavepackets and trapped acoustic modes in a turbulent jet: Coherent structure eduction and global stability. Journal of Fluid Mechanics, 825:1153–1181, 2017.

[41] Antonio Segalini. Experimental analysis of coaxial jets: instability, flow and mixing characterization. PhD thesis, Università di Bologna, Bologna and Italy, 01.01.2010.

[42] G. SenGupta. Analysis of jet-airframe interaction noise. In 8th Aeroacoustics Conference, Aeroacoustics Conferences. American Institute of Aeronautics and Astronautics, 1983.

[43] Christopher K. Tam and Sathyanarayanan Chandramouli. Jet-plate interaction tones relevant to over-the-wing engine mount concept. In 25th AIAA/CEAS Aeroacoustics Conference, Aeroacoustics Conferences. American Institute of Aeronautics and Astronautics, 2019.

[44] Christopher K. Tam and Sathyanarayanan Chandramouli. Jet-plate interaction tones relevant to over-the-wing engine mount concept. In 25th AIAA/CEAS Aeroacoustics Conference, Aeroacoustics Conferences. American Institute of Aeronautics and Astronautics, 2019.

[45] Christopher K. W. Tam and Laurent Auriault. Jet mixing noise from fine-scale turbulence. AIAA Journal, 37(2):145–153, 1999.

[46] Christopher K. W. Tam and Fang Q. Hu. On the three families of instability waves of high-speed jets. Journal of Fluid Mechanics, 201:447–483, 1989.

[47] Christopher K. W. Tam and Nikolai N. Pastouchenko. Fine-scale turbulence noise from dual-stream jets. AIAA Journal, 44(1):90–101, 2006.

[48] Christopher K. W. Tam and K. B. M. Q. Zaman. Subsonic jet noise from nonaxisymmetric and tabbed nozzles. AIAA Journal, 38(4):592–599, 2000.

[49] Christopher K.W. Tam and Sathyanarayan Chandramouli. Jet-plate interaction tones relevant to over-the-wing engine mount concept. Journal of Sound and Vibration, 486:115378, 2020.

[50] Marc Terracol, Eric Manoha, and Benoit Lemoine. Investigation of the unsteady flow and noise generation in a slat cove. AIAA Journal, 54(2):469–489, 2015.

[51] Aaron Towne, André V. G. Cavalieri, Peter Jordan, Tim Colonius, Oliver Schmidt,

Vincent Jaunet, and Guillaume A. Brès. Acoustic resonance in the potential core of subsonic jets. Journal of Fluid Mechanics, 825:1113–1152, 2017.

[52] D. J. Way and B. A. Turner. Model tests demonstrating under-wing installation effects on engine exhaust noise. In 6th Aeroacoustics Conference, Aeroacoustics Conferences. American Institute of Aeronautics and Astronautics, 1980.

[53] K. B. M. Q. Zaman and M. D. Dahl. Noise and spreading of subsonic coannular jets-comparison with single equivalent jet. AIAA Journal, 45(11):2661–2670, 2007.